Extracting Molecular Information from Spectroscopic Data

by

Cian John Menzel-Jones

B.Sc., Queen's University, 2004
M.Sc., The University of British Columbia, 2007

A THESIS SUBMITTED IN PARTIAL FULFILLMENT OF
THE REQUIREMENTS FOR THE DEGREE OF

DOCTOR OF PHILOSOPHY

in

The Faculty of Graduate and Postdoctoral Studies

(Physics)

THE UNIVERSITY OF BRITISH COLUMBIA

(Vancouver)

December 2014

Abstract

This thesis explores new ways with which to utilize molecular spectroscopic data in both the time and frequency domain. Operating within the Born-Oppenheimer approximation (BOA), we show how to obtain the signs of transition-dipole amplitudes from fluorescence line intensities. Using the amplitudes thus obtained we give a method to extract highly accurate excited state potential(s) and the transition-dipole(s) as a function of the nuclear displacements. The procedure, illustrated here for the diatomic and triatomic molecules, is in principle applicable to any polyatomic system. We, also, extend this approach beyond the BOA and demonstrate applications involving bound-continuum transition, and double-minimum potentials.

Furthermore, by using as input these measured energy level positions and the transition dipole moments (TDMs), we derive a scheme that completely determines the non-adiabatic coupling matrix between potential energy surfaces and the coordinate dependence of the coupling functions. We demonstrate results in a diatomic system with two spin-orbit coupled potentials, whereby experimentally measured information along with TDMs computed for two corresponding diabatic potentials to the fully spin-orbit coupled set of eigenstates, are used to extract the diagonal and off-diagonal spin-orbit coupling functions.

Using time-resolved spectra, we show that bi-chromatic coherent control (BCC) enables the determination of the amplitudes (=magnitudes+phases) of individual transition-dipole matrix elements (TDMs) in these non-adiabatic coupling situation. The present use of BCC induces quantum interferences using two external laser fields to coherently deplete the population of different pairs of excited energy eigenstates. The BCC induced depletion is supplemented by the computation of the Fourier integral of the time-resolved fluorescence at the beat frequencies of the two states involved. The combination of BCC and Fourier transform enables the determination of the complex expansion coefficients of the wave packet in a basis of vibrational energy eigenstates, from simple spontaneous fluorescence data.

Preface

Chapter 3 is based on the work first developed by the author and colleagues at the Institute of Molecular Science (IMS), Okazaki, Japan, between October and December 2009 by invitation of Dr. Kenji Ohmori. Dr. Moshe Shapiro suggested the direction of the project, which was jointly researched by the author and visiting science Dr. Xuan Li. This research spawned several publications:

(I) X. Li, C. Menzel-Jones, D. Avisar and M. Shapiro, *Solving the spectroscopic phase: imaging excited wave packets and extracting excited state potentials from fluorescence data*, PCCP **12**, 15760-15765 (2010)

(II) X. Li, C. Menzel-Jones and M. Shapiro, *Spectroscopic Phase and the Extraction of Excited-State Potentials from Fluorescence Data*, J. Phys. Chem. Lett. **1**, 3172-3176 (2010)

(III) C. Menzel-Jones, X. Li and M. Shapiro, *Extracting double minima excited state potentials from bound-continuum spectroscopic data*, J. Mol. Spectrosc. **268**, 221-225 (2011)

For manuscripts (I) and (II), the calculations, first draft, revisions, and editing, were jointly performed with Dr. Li, while Dr. Li acted as the principal in the review process. D. Avisar had originally tackled the problem and provided some initial insight into its direction. The calculations for (III) were simultaneously developed with Dr. Li, while the first draft, revision, editing and review process were carried out by the author. Dr. Shapiro was seminal to the revisions and edits of the manuscripts (I,II,III) as well as being involved in monitoring and providing advice on the results.

The central idea of Chapter 4 was provided by Dr. Shapiro. The theoretical solution and numerical calculations were developed by the author. This work lead to a publication (IV) which was written and submitted by the author with supervision from Dr. Shapiro:

(IV) C. Menzel-Jones and M. Shapiro, *Complex Wave Function Reconstruction and Direct Electromagnetic Field Determination from Time-Resolved Intensity Data*, J. Phys. Chem. Lett. **3**, 3353-3359 (2012)

The material in Chapter 5 was jointly devised by the author and Dr. Shapiro. The author performed the theoretical analysis and numerical calculations, then composed and submitted the resulting two manuscripts (V,VI). Dr. Shapiro provided important draft revisions and references.

(V) C. Menzel-Jones and M. Shapiro, *Using Time-Resolved Experiments and Coherent Control to Determine the Phase of Transition Dipole Moments between Individual Energy Eigenstates* J. Phys. Chem. Lett. **4**, 3083-3088 (2013)

(VI) C. Menzel-Jones and M. Shapiro, *Using coherent control to extract the phases of electronic transition-dipole matrices : The LiRb case* Can. J. Chem. **92**, 94-99 (2014)

Chapter 6 is based on an idea initially proposed by Dr. Shapiro, the author developed the work and performed numerical calculations. The first draft, revisions, and editing, of the manuscript (VII) were done in collaboration with Dr. Shapiro. The work lead to a manuscript that is currently in the review process.

Table of Contents

List of Tables

List of Figures

in memory,

Moshe Shapiro

Chapter 1

Introduction

1.1 Motivation

Molecules are an exciting platform for fundamental and applied research due to their complex quantum mechanical structure. In addition to the degrees of freedom of an atom, a molecule also possesses vibrational and rotational motions that can be harnessed [20–22]. This added complexity gives molecules interesting characteristics and behaviors, and opens the door for widespread applications, particularly in the new field of ultracold chemistry [23]. In this regime, molecular systems would become good candidates for performing large scale quantum information processing, and acting as quantum simulations machines. Ultracold molecules would allow for the realization of spin-lattice models and the study of exotic few- and many-body quantum mechanics. In addition, they could become a test bed for fundamental physics, including parity violation, time variation of constants, and the search for a permanent electric dipole moment of the electron [24]. Speculatively, molecules may even allow for the development of quantum sensors, cloaking devices, and novel lasers [25].

All of the above hoopla assumes that we have very accurate knowledge of the structure and coherence properties of the molecules in our system. Acquiring this information, which requires observing the interactions between photons and molecules, concerns the field of molecular spectroscopy. The laser, as a monochromatic, intense and coherent light source, has made possible high-resolution spectroscopic (HRS) measurements from which molecular constants and discrete energies levels can be determined. The absorption/emission spectra tools such as observing the fluorescence of electromagnetic radiation from molecules, typically in their gas phase, leads to information about the internal molecular structure (electronic distributions, nuclear vibrations and rotations). Combining the ability of light to be used as probe with the richness of molecular spectroscopy data in both the frequency and time domains, we constantly seek to improve on and develop new methods for extract-

ing information from the spectroscopic data in order to better deduce the physical or chemical properties of a molecular species. A recent quote from a 2013 review article in Molecular Physics titled *Manipulation of Molecules with Electromagnetic Fields* states: "Theoretical simulations of experiments at ultracold temperatures are impeded by the lack of numerical methods to produce intermolecular potentials with sufficient accuracy. It is necessary to develop approaches for inverting the scattering problem in order to fit intermolecular potentials,..." [24].

Alkali-metal diatomics are the simplest molecules consisting of two atoms having only one valence electron and thus serve as excellent test objects to probe different theoretical approaches that extract spectroscopic information. Experimentally, alkali-metal diatomics are also relatively easy to produce and can be addressed using conventional laser sources (Ar^+,He-Ne,dye laser, *etc.*). The research of diatomic molecule spectroscopy is very old but still active and innovative [26], since understanding the structure of these diatomic molecules is an essential step in the move from atoms to larger molecules. Central to the study of diatomic molecules is the concept of electronic potential energy surface (PES) which represents an effective potential energy function for the nuclear degrees of freedom due to the electronic motion. The electronic PES's are key to our current understanding of the structure and dynamics of molecules, especially that of collisional phenomena and chemical reactivity. Currently, there is an additional motivation for obtaining highly accurate diatomic potentials due to our emerging ability to synthesize ultracold diatomic molecules from ultracold atoms [27–29]. This can be done by, e.g., photoassociation [30], which provides a highly accurate ground potential close to the dissociation limit [31–33].

So far, knowledge of PES with many degree of freedoms has relied mainly on *ab initio* [34] or semiempirical [35–38] quantum chemistry computations. Despite the simple structure of alkali-metal dimers, *ab initio* (fully-theoretical) calculations are not sufficient, their results don't match spectroscopically derived information of the PES, electronic transition dipole moments or lifetimes, *etc.* This is because the Schrödinger equation cannot be solved analytically, and approximations must be used, leading to discrepancies between the empirical and theoretical PES for heteronuclear dimers that can reach several hundred cm^{-1} while experimental errors in the energy eigenvalues are only $0.1cm^{-1}$. The accuracy of computational techniques is still limited relative to the accuracy of measurements of spectroscopic line positions. Thus, a direct procedure for the extraction ("inversion") of PES

from spectroscopic data is highly desirable. Though the semiclassical method (the Rydberg-Klein-Rees (RKR) method) exists for (one-dimensional) diatomic systems, no direct inversion method has so far been developed for higher dimensional systems. Although many approximate schemes do exist, they only extract potentials when the BO approximation is valid (Sec. (4.1)). Fortunately, a lot of effort has been put towards determining the lowest (ground) singlet and triplet PES, since all molecules typically reside in these states, and thus these states will serve as known structure on which any new method can be based. We have developed a fully quantum mechanical inversion procedure, based on both frequencies and intensities, that is really remarkable, valuable, unique and builds a solid foundation. The PES are extracted from experimental observations by elevating relative intensity information to the status of primary input to the spectrum-to-potential inversion alongside energy level information need for assignment of observed spectra. Implementations are performed on some of the best studied homonuclear (*e.g.* Na_2) and heteronuclear (*e.g.* NaK) alkali dimers. This molecular spectroscopic technique looks to fill the void where accuracy is limited in regards to knowledge about structure and properties of many other diatomic species. The exact quantum procedure is valid for polyatomics and may also be generalized to liquid systems in terms of mean force potentials.

Spectroscopy in the frequency domain produces energy spectral lines which, however, yield no dynamical information. A complementary picture to HRS, is obtained with time-resolved spectra which records total absorption/emission intensity as a function of time. Time-resolved spectroscopy (TRS) has been used to determine lifetimes of excited states (related to transition probabilities and line intensities) used for the study of chemical reactions [39], radiative lifetimes and orbital mixing coefficients [40]. Moreover, these measurements allow one to observe quantum state dynamics operating on short time scales, in which vibrations (100s of fs) and rotations (1-1000 picoseconds (ps)) occur [41]. In particular, modern experimental studies have been made possible with the recent developments in ultrafast laser technology (*e.g.* 10 fs pulse in the visible) capable of exciting molecular rovibrational wavepackets (WP) consisting of a superposition of a set of stationary eigenstates each with a given phase. Unlike stationary wavefunctions, the molecular WP has a well defined position and group velocity within the uncertainty principle and requires a coherent excitation to instantiate phase relation between states (using a broadband femtosecond pulse). The vibrational WP in diatomics represents the probability of

the system having a given internuclear distance and typical oscillates with a period of a few hundred fs. Thus the time-dependent spectrum is governed by the motion of the WP and reveals information about the internal molecular dynamics.

A lot of effort has been put toward the active control of molecular quantum dynamics, especially in regards to state-selective control schemes and for realizing molecular quantum computations. In addition to developing realistic logic gates and controlling long-range dipole interactions, it will be imperative to extract state information without loss of amplitude or phase information. In the quantum information community the issue of phase reconstruction of an unknown quantum state is recognized as a crucial problem, and the ability to do so in spite of the non-cloning theorem lies in the multi-replicas generation of a given quantum state as found in a gaseous ensemble. In this work we present a scheme capable of reading out a molecular ensembles state properties, however the approach is reliant on accurate knowledge of the phases of the electronic transition dipole moments.

For homonuclear diatomics with no permanent dipole moment, electronic dipole transitions between rovibrational states are induced by electric fields and their strength are thus governed by this induced electric dipole moment. This is also true for polar (or heteronuclear) dimers in field-free environment, because the permanent dipole moment from the non-uniform distribution of charge does not play a role in transitions between different electronic states. Well-known to scattering theory is the "phase problem", where the objective is the inversion of experimental atomic collision cross sections to yield the interaction potential or repulsive behavior (see review in Ref. [42]) by determining the phases of the complex-valued scattering amplitudes [43, 44]. In bound-bound spectroscopy this phase problem is less severe as compared to the scattering case because here we deal with *real* electronic transition dipole matrix elements so we only need to determine their signs. Nevertheless, these signs affect experimental observations, for example, in the short pulse excitation of a wave packet, the fluorescence signal is composed of the beatings between many transitions, any change in whose signs fundamentally affecting the observations. Researchers, such as J. Tellinghuisen [45, 46], have detailed what determines the magnitudes of the Franck-Condon factors (not overall signs), and shows where and why vibrational overlap integrals accumulate. However, lacking a potential, Tellingheusen's work does not solve for the signs of the FC factors, since accumulation of overlap integrals does not affect the sign of the integral itself because the wavefunction itself can possess an undetermined global phase in coordinate space. For instance, when the

wavefunction of some state $|v'>$ is unknown, it is not trivial to draw lines between basis wavefunctions $|v''>$ and the Frank-Condon factors, $<v''|v'>$. We argue that this consistency is important in any theoretical/experimental study when both the wavefunction and the Frank-Condon factors are used: in short pulse excitation of a wavepacket, both the wavefunction and the Frank-Condon factors influence the propagation of the system and thus the quantum echo phenomena.

Nowhere do these relative phases (or signs) play a greater role than in coherent control, whereby one can tailor the amplitude and phase of an electric field at specific spectral components of the optical field to manipulate the desired complex coefficients of the eigenstates. This interference between quantum routes involving different vibrational states are very important to understand/control the quantum dynamics, and we harness this technique to extract relative transition dipole phase information between select states.

A fundamental property of molecular electronic states is that they have an associated spin angular momentum quantum number, S. Similar to most operators in quantum mechanics, the transition probabilities are diagonal in S, when working in the diabatic representation of the Born-Oppenheimer approximation. Thus, to first order, electronic transition between different spin states is forbidden. For example, a diatomic molecule residing in a singlet ($S = 0$) electronic state would not be able to access a triplet ($S = 1$) electronic state to first order. However, we find that extensive mixing between different spin states does occur and its effects on both HRS and TRS can be described by a spin-orbit coupling (SOC) Hamiltonian. This SOC mixing of singlet-triplet bare states is one of the most important mechanisms for extending radiative lifetime of a molecule in a collision free environment. Moreover, it allows for direct access from the scattering continuum to the ground PES; this has been utilized in approaches geared towards the generation of ultracold molecules [23]. Understanding and describing this coupling mechanism is possible by analyzing differences in the HRS (or perhaps TRS) data and gives vital information into a molecule's behavior.

1.2   Thesis Outline

The following (and last) section of this chapter will mention the units and numerical methods used in the simulations throughout this work. The next chapter will then provide a basic review of the background theory necessary for understanding the

subsequent research. For completeness, we cover fundamental molecular structure including the Born-Oppenheimer approximation, and an introduction to diatomic and polyatomic molecules. Light-matter interaction from a semi-classical perspective follows with application to molecular transitions. Next, we present laser excitation and control schemes directed at diatomic molecules in an ensemble, before covering molecule spectroscopy in the frequency and time domains.

In Chapter 3, we first discuss currently existing methods for determining potential energy surface from spectroscopic data. Then, we develop an inversion scheme for obtaining the signs of transition-dipole amplitudes from fluorescence line intensities. Using the amplitudes thus obtained we show how to extract highly accurate excited state potential(s) and the transition-dipole(s) as a function of inter-nuclear displacements. The same dipole amplitudes can also be used to extract the phase and amplitude of unknown time-evolving wave packets, in essentially a quantum non-demolition manner. The procedure, which is demonstrated for the $A(^1\Sigma_u^+)$ and $B(^1\Pi_u)$ states of the Na_2 molecule, is shown to yield reliable results even when we are given incomplete or uncertain data.

Next, we present an extension to the bound-continuum cases of our bound-bound inversion scheme for extracting excited state potentials and transition-dipoles from fluorescence data. The procedure involves the discretization of the continuous spectrum using box-normalization. The addition of the continuous spectrum guarantees completeness of the basis set used in the implicit expansion of the unknown excited state vibrational wave functions. The method, which is found to be robust with respect to missing data or uncertainties in the line strengths, is also capable of inverting polyatomic fluorescence data. We demonstrate the viability of the method by successfully generating the potential energy curve (PEC) for the $C(^1\Pi_u)$ state of the Na_2 molecule using a fraction of the total transitions to/from the $X(^1\Sigma_g^+)$ ground state, and by extracting the double-well $2^1\Sigma_u^+(3s+4s)$ curve of Na_2, assuming no prior knowledge of its structure.

Lastly, we present two extensions of this work. First, we demonstrate a successful extraction of a model two-dimenionsal (2D) PES using our inversion procedure. This follows along the same route as in the one-dimensional (1D) case, by using the magnitudes and positions of a set of frequency-resolved fluorescence (or absorption) lines we extract the relative *phases* of the transition-dipole matrix elements. With this information together with the (ground) PES to (from) which emission (absorption) occurs, we reconstruction a *point by point* two dimensional excited state PES.

The method is applied to 2D PES with multiple minima and many missing lines, and achieves typical (root-mean-square) RMS errors of < 0.002 cm^{-1} in the classically allowed region, and < 0.02 cm^{-1} in the classically forbidden region.

Next we present a new ("dipole correction") inversion scheme for the accurate extraction of excited state potentials from fluorescence line positions and line strengths which *does not* require the Franck Condon Approximation (FCA). The accuracy of the potential energy surfaces (PES) thus extracted is much higher than that of the FCA derived PES because we make use of the coordinate dependence of the electronic transition-dipoles. Using Na$_2$ we find the A $\rightarrow$ X electronic transition dipole function to accuracies better than 1×10^{-3} Debye. Then we use the A($^1\Sigma_u^+$)$\rightarrow$X($^1\Sigma_g^+$) P-branch emission to extract the excited state potential to global errors of less than 0.1 cm^{-1}, Moreover, we demonstrate that using emissions data from only the $s = 0 - 5$ low-lying levels or the $s = 20 - 23$ states of the Na$_2$ B($^1\Pi_u$) PES, we can obtain inversion results with global errors as small as 0.08 cm^{-1}.

In Chapter 4, we describe methods that one can use to image molecular wave-functions and discuss their associated drawbacks. Then, we present a reference-free robust method for the non-destructive imaging of complex time-evolving molecular wave functions using as input the time-resolved fluorescence signal. The method is based on expanding the evolving wave function in a set of bound stationary states, and determining the set of complex expansion coefficients by calculating a series of Fourier integrals of the signal. As illustrated for the A$^1\Sigma_u^+$ electronic state of Na$_2$, the method faithfully reconstructs the time-dependent complex wave function of the nuclear motion. Moreover, using perturbation theory to connect the excitation pulse and the material expansion coefficients, our method is used to determine the electromagnetic field of the excitation pulse. Thus providing a simple technique for pulse characterization which obviates the additional measurements and/or iterative solutions that beset other techniques. The approach, which is found to be quite robust against errors in the experimental data, can be readily generalized to the reconstruction of *polyatomic* vibrational wave functions.

To address the "phase problem", to which no direct approach exist, in Chapter 5 we develop an imaging method which uses Bi-chromatic Coherent Control (BCC) in conjunction with time-resolved fluorescence to extract the complex amplitudes (magnitudes and phases) of individual Transition Dipole matrix elements (TDM's) as well as the amplitude of time-evolving wave packets. The method relies on determining the phase relation between the BCC fields, which look to deplete the population of

different pairs of excited energy eigenstates, through the computation of a Fourier integral of the time-resolved fluorescence at the beat frequencies of these pairs of states. We illustrate our procedure by determining the amplitudes of the TDM's linking the vibrational states of the $A^1\Sigma_u^+$ and those of the $X^1\Sigma_u^+$ electronic states of Na_2. Furthermore, we demonstrate its broad applicability to systems in which there exist interacting potential energy surfaces by extracting the expansion coefficients of a wave packet in the basis of vibrational energy eigenstates in the strong spin-orbit coupling potentials in RbCs.

In addition, we illustrate our method by determining the amplitudes of the TDMs linking the vibrational states of the $A^1\Sigma_u^+ \sim b^3\Pi$ spin-orbit coupled potentials to *both* the singlet $X^1\Sigma_u^+$ and triplet $a^3\Sigma_u^+$ electronic ground states in LiRb. The approach, which is found to be quite robust against errors in the BCC procedure and experimental data, can be readily generalized to the imaging of wave packets of *polyatomic* molecules.

Lastly, Chapter 6 develops the first direct extraction of non-adiabatic couplings from HRS data. We show that it is possible to extract spin-orbit and non-adiabatic (non Born Oppenheimer) coupling terms, as well as potential curves and transition dipole moments from fluorescence line positions and line strengths. We demonstrate the viability of our method by extracting the spin orbit couplings of the weakly coupled $D(3)^1\Pi$ and $d(3)^3\Pi$ electronic states of NaK, and the strongly coupled $A^1\Sigma^+$ and $b^3\Pi$ electronic states of RbCs. The method can be applied to the extraction of non-adiabatic couplings in multi-dimensional systems and for more than two interacting electronic states.

To end we provide a final conclusion summarizing the key results of this thesis, and their applicability. The bibliography can be found thereafter.

1.3 Units and Numerical Simulations

Throughout the theoretical work of this thesis we will be using atomic units, namely,

$$a_0 = m_e = e = \hbar = \frac{1}{4\pi\epsilon_0} = 1 \tag{1.1}$$

where a_0 is the Bohr radius, m_e and e is the mass and elementary charge of the electron respectively. $\hbar$ represents Dirac's constant and Coulomb's constant includes the permittivity of free space ϵ_0. The energy in these units is given by Hartrees

(labelled as H or a.u.) and the speed of light $c \approx 137$.

Atomic units were used in all numerical calculations, however, for presentation purposes the final units were occasionally converted to a more recognized form. Spectroscopist typically use units of wavenumber (cm^{-1}) and Angstroms (Å) for energies and distances, with conversions as follows:

$$1 \text{ H} \approx 21947 \text{ cm}^{-1} \qquad 1 \text{ Bohr} \approx 0.5292 \text{ Å} . \tag{1.2}$$

Time is always converted back to the SI units of seconds.

The simulations themselves were generally done using very well known diatomic molecules. One of the most explored molecules and theoretically simplest after H_2, due to small number of valence electrons, may be Na_2 (after Li_2). References will show that Na_2 has thoroughly explored low-lying single and double well electronic states, including spectroscopically measured adiabatic curves and *ab initio* diabatic potentials and non-adiabatic (spin-orbit) couplings functions. For each method, the "experimental" data has been simulated from the given electronic structure. It will be shown how this information can be easily attained from laser fluorescence via high-resolution Fourier transform spectroscopy or time-resolved upconversion techniques. It will be assumed that the frequency-resolved spectra can be correctly assigned to eigenenergies of electronic PES (*e.g.* via combination differences or LoomisWood diagrams).

Numerical solution to the time independent Schrödinger were found using a basic finite difference approach. Typical higher order methods for solving ordinary differential equations, such as 4th-order Runge-Kunta or Numerov's method, were found to be unnecessary. Using a finite difference grid by discretizing space into N distinct points, R_i, for $i = \{1, N\}$, allows for simply evaluation of functions and their derivatives. For example using a one-dimensional (1D) Taylor expansion of the second derivative operator about a point R_i, we get

$$\frac{d^2}{dR^2}\psi(R) \approx \frac{\psi(R_i + h) - 2\psi(R_i) + \psi(R_i - h)}{h^2} \tag{1.3}$$

where $h = R_{i+1} - R_i$ represents the distance between adjacent points. A 1D treatment of Schrödinger equation can now solved as

$$\psi(R_i + h) - 2[1 + h^2 V(R_i)]\psi(R_i) + \psi(R_i - h) = E\psi(R_i) \tag{1.4}$$

9

for eigenvalues E with eigenstates $\psi(R)$ at each point R_i. The N above equations can be succinctly expressed as a tridiagonal matrix containing the kinetic and potential energy terms, with column vectors $\psi(R)$ solving the equality for some given energy E. Using common matrix diagonalization routines, either from LAPACK in FORTRAN or eigen3 in C++, a set of N eigensolutions can be found matching the grid dimensions.

An alternative approach used to solve Eq. (1.4) for large grid sizes, when the diagonalization becomes cumbersome, is known as the shooting method. We treat the Schrödinger equation as a two-points boundary value problem where $\psi(R) \to 0$ at the ends of the range (for bound states) and re-express Eq. (1.4) as

$$\psi(R_i + h) = 2[1 + h^2(V(R_i) + E)]\psi(R_i) + \psi(R_i - h) \ . \tag{1.5}$$

Using two initial values $\psi(R_0) = 0$ and $\psi(R_1) = 1$ and starting at the minimum possible energy, $E = 0$ or $E = -D_e$, where D_e is the dissociation limit of a PES, we can propagate the solution to $\psi(R_i)$ along the range until reaching the end. Our objective is to increment E until we find $\psi(R_N) \approx 0$, which yields a solution satisfying the two boundary conditions. This convergent solution gives the eigenvalue E and corresponding eigenvectors one at a time without large computational expense.

Chapter 2

Background Theory

Here we provide an introduction to molecular structure based on the time-independent Schrödinger equation (TISE). We wish to understand the basic principles governing molecules, especially diatomics, and the origin of their spectroscopic properties. This theoretical background of their energy structure will be necessary for the understanding of molecular excitations, wavepackets, and light-matter interactions. For a more detailed review of the physics of diatomic molecules please see Refs. [47, 48].

A directly computational approach to the TISE for molecular system will be found to be unfeasible, and several approximations will be discussed. Most importantly, is the assumptions that the electrons adiabatically follow motion of nuclei and the nuclei rotate and vibrate within effective field of electrons. This allows for a definition of the potential energy surface, however, breakdowns of this approximation will become important, particularly when considering non-adiabatic couplings.

2.1   Molecular Structure

In order to describe a molecular system we look towards solving the TISE

$$\mathbf{H}(\mathbf{q}, \mathbf{R})\Psi(\mathbf{q}, \mathbf{R}) = \boldsymbol{E}\Psi(\mathbf{q}, \mathbf{R}) \tag{2.1}$$

where $\mathbf{H}(\mathbf{q}, \mathbf{R})$ is the quantum mechanical Hamiltonian for the molecule, $\boldsymbol{E}$ and $\Psi(\mathbf{q}, \mathbf{R})$ are the eigenvalues and corresponding eigenstates with $\mathbf{q}$ and $\mathbf{R}$ representing the collective electronic and nuclear coordinates, respectively. The molecular Hamiltonian $\mathbf{H}(\mathbf{q}, \mathbf{R})$ can be written as a sum of its electronic and nuclear parts

$$\mathbf{H}(\mathbf{q}, \mathbf{R}) = \mathbf{H}_e(\mathbf{q}, \mathbf{R}) + \mathbf{H}_N(\mathbf{R}) \ , \tag{2.2}$$

with

$$\mathbf{H}_e(\mathbf{q}, \mathbf{R}) = \mathbf{T}_e(\mathbf{q}) + V_{ee}(\mathbf{q}) + V_{eN}(\mathbf{q}, \mathbf{R}) \tag{2.3}$$

and

$$\mathbf{H}_N(\mathbf{R}) = \mathbf{T}_N(\mathbf{R}) + V_{NN}(\mathbf{R}) \; , \tag{2.4}$$

where $\mathbf{T}_e(\mathbf{R})$ and $\mathbf{T}_N(\mathbf{R})$ are the kinetic energy operators for the electronic and nuclei respectively. The V terms are the electrostatic potential energies representing: the sum of all electron-electron repulsions

$$V_{ee}(\mathbf{q}) = \frac{1}{2} \sum_{i \neq j} \frac{1}{|q_i - q_j|} \; ,$$

the sum of all nuclear-nuclear interactions

$$V_{NN}(\mathbf{R}) = \frac{1}{2} \sum_{\alpha \neq \beta} \frac{Z_\alpha Z_\beta}{|R_\alpha - R_\beta|} \; ,$$

and the sum of all electron-nuclei attractions

$$V_{eN}(\mathbf{R}) = - \sum_{\alpha \neq i} \frac{Z_\alpha}{|R_\alpha - q_i|} \; .$$

The coordinate vectors R_α designates the position of a nucleus α and q_i are the electronic coordinate of the ith electron. The strength of these Coulombic interactions are quantified by the nuclear charges Z_α of the α nucleus and the elementary charge of the electrons ($e = 1$).

2.1.1 Born-Oppenheimer Approximation

Even for small molecules, treated non-relativistically, it is not possible to obtain an exact solution to the Schrödinger equation in Eq. (2.1). The complexity of the Hamiltonian even prevents one from performing direct numerical (*ab initio*) molecular structure calculation. As a result, progress must be made through approximations, the most fundamental of which, known as the *Born-Oppenheimer approximation* (BOA), enables one to separate the nuclear from the electronic coordinates. Based on the large mass difference between the electrons ($m = 1$) and nuclei ($\mu \gtrsim 1836$), it is assumed that the electronic motion occurs on a much faster timescale than the nuclear motion, therefore the electronic configuration quickly adjusts itself to any nuclear motion. By assuming that this adjustment occurs instantaneously we may

write the total wavefunction as

$$\Psi(\mathbf{q}, \mathbf{R}) = \Psi_e(\mathbf{q}; \mathbf{R}) \cdot \psi_N(\mathbf{R}) \tag{2.5}$$

where $\Psi_e(\mathbf{q}; \mathbf{R})$ are the electronic eigenstates of the electronic Hamiltonian in Eq. (2.3)

$$H_e(\mathbf{q}; \mathbf{R})\Psi_e(\mathbf{q}; \mathbf{R}) = \boldsymbol{E}_e(\mathbf{R})\Psi_e(\mathbf{q}; \mathbf{R}) \ , \tag{2.6}$$

and $\psi_N(\mathbf{R})$ are the nuclear wavefunctions for the corresponding Hamiltonian in Eq. (2.4)

$$H_N(\mathbf{R})\psi_N(\mathbf{R}) = E_N\psi_N(\mathbf{R}) \ . \tag{2.7}$$

Notice in Eq. (2.6) that under the BOA it was assumed that $T_e \gg T_N$ (by a factor of m/μ), thus the effect of the nuclear kinetic energy operator $T_N(\mathbf{R})$ on the electronic wavefunctions $\Psi_e(\mathbf{q}; \mathbf{R})$ has been ignored. Corrections to this approximation will be addressed in Sec. (2.1.2).

By omitting the couplings between the nuclear and electronic parts, the full Schrödinger equation can be written in terms of the nuclear wavefunctions

$$\left(\mathbf{T}_N(\mathbf{R}) + V_{NN}(\mathbf{R}) + \boldsymbol{E}_e(\mathbf{R})\right)\psi_N(\mathbf{R}) = E\psi_N(\mathbf{R}) \ , \tag{2.8}$$

where the electronic wavefunctions, $\Psi_e(\mathbf{q}; \mathbf{R})$, normalized to unity ($\langle\, \Psi_e \,|\, \Psi_e \,\rangle = 1$), have dropped out upon integration over $\mathbf{q}$. The sum of the electronic energy and Coulomb potential terms of the nuclei in Eq. (2.8),

$$V(\mathbf{R}) = V_{NN}(\mathbf{R}) + \boldsymbol{E}_e(\mathbf{R}) \ , \tag{2.9}$$

represent the effective (or averaged) potential on which the the nuclei move, and are referred to as (electronic) potential curves (or surfaces). In other words, it represents the potential energy governing the dynamical equations of nuclear motion. These potential energy surfaces (PESs) of a molecule, $V(\mathbf{R})$, do not represent any physical observable, but are merely convenient mathematical constructions derived from a specific set of assumptions, namely the separation of variables (Eq. (2.5)) and that $\langle\, \Psi_e \,|T_N|\, \Psi_e \,\rangle \sim T_N\langle\, \Psi_e \,|\, \Psi_e \,\rangle$. When the eigenvalues of the full Hamiltonian, Eq. (2.1), which are now a sum of the nuclear-coordinate dependent electronic eigenvalue,

$\boldsymbol{E}_e(\mathbf{R})$, and the nuclear energy E_N

$$\boldsymbol{E} = \boldsymbol{E}_e + E_N \tag{2.10}$$

do not exactly match observed energy levels, it points to a failure in one of these approximations (see discussion in Sec. (2.1.2)). By treating molecules in this way, the electronic Schrödinger equation, Eq. (2.6), can be solved for various electronic configuration at different values of the inter-nuclear separation $\mathbf{R}$. Then each electronic eigenenergy defines a different *Born-Oppenheimer potential energy surface* (PES) which defines the allowable vibrational and rotational motions and energy states of the nuclei.

2.1.2 Diatomic Molecules

We now continue the discussion with an emphasis on diatomic molecules, though many of the following concepts extend to polyatomic systems (see Sec. (2.1.3)). A diatomic can easily be cast into a central-potential problem, where the frame of reference of the nuclear Schrödinger equation of Eq. (2.8) is moved into the center-of-mass (CM) coordinates and the variables are separated into radial and angular spherical components. Namely, the nuclear wavefunction is expressed as $\psi_N(\mathbf{R}) = R^{-1}\psi_{\nu,l}(R)Y_{l,m}(\theta, \phi)$ where $\psi_{\nu,l}$ represents the radial wavefunction and $Y_{l,m}$ are the spherical harmonic functions. By omitting the CM motion, the problem reduces to the familiar radial Schrödinger equation (with $\hbar = 1$), whose eigenstates represent the possible vibrational and rotation (*i.e. rovibrational*) states available to the molecule under the influence of the central potential,

$$\left(-\frac{1}{2\mu}\frac{d^2}{dR^2} + V(R) + \frac{l(l+1)}{2\mu R^2}\right)\psi_{\nu,l}(R) = E_{\nu,l}\psi_{\nu,l}(R) , \tag{2.11}$$

where μ is the reduced mass, ν and l label the vibrational and rotation quantum numbers respectively, and R is a scalar parameter representing the separation between the atoms. One should see that the form of the above equation is identical to that for a single particle in a one dimensional (1D) effective potential given by

$$V_l^{eff}(R) = V(R) + \frac{l(l+1)}{2\mu R^2} \tag{2.12}$$

where the second (centrifugal) term gives the energy associated with the rotational motion, and $V(R)$ represents the radial dependent potential curve (or PES). As expected, when values of l, the quantized amount of spatial angular momentum, get larger, the atoms experience a stronger repulsive force that stretches the bond, thus also affecting the vibrational modes of the molecule. This behavior is a manifestation of rotational-vibrational coupling. For an extensive description of diatomic molecules please refer to Ref. [47].

Electronic States

The electronic eigenstates or PESs in the Born-Oppenheimer approximation can either be obtained from direct *ab initio* calculations of the electronic Schrödinger equation (Eq. (2.6)), or from inversion techniques based on the analysis of experimental data (Sec. (3.1)). The classification of these molecular electronic states is done according to the quantum numbers of the angular momenta operators that commute with the electronic Hamiltonian ($\mathbf{H}_e(\mathbf{q}, \mathbf{R})$). In diatomic molecules there exist angular momenta associated with the electron orbital motion ($\mathbf{L}$), the electron spin ($\mathbf{S}$), the nuclear rotation ($\mathbf{R}$), and the nuclear spin ($\mathbf{I}$). Ignoring the small nuclear spin component, the total angular momentum is written as $\mathbf{J} = \mathbf{L} + \mathbf{S} + \mathbf{R}$, and the total exclusive of spin as $\mathbf{N} = \mathbf{J} - \mathbf{S}$. However, not all these angular momenta are conserved and they may interact together in various combinations. In particular, there are five idealized coupling cases which may occur between these angular momenta [1, 49], and the choice of which coupling pair (*i.e.* $\{\mathbf{L}, \mathbf{S}\}$) dominates defines a given basis set of $\mathbf{H}(\mathbf{q}, \mathbf{R})$ (Eq. (2.2)).

The preferred basis throughout this thesis will be that of Hund's case (a) (see Fig.2.1) in which the strongest coupling occurs between the two angular momenta $\mathbf{L}$ and $\mathbf{S}$ and the inter-nuclear axis ($\mathbf{A}$), namely the energies associated with the $\{\mathbf{L}, \mathbf{A}\}$ and $\{\mathbf{S}, \mathbf{A}\}$ interactions are much larger than the other pairs. This is the most common choice in most diatomic molecules and allows for the definition of two new "good" quantum numbers (*i.e.* operators that commute with $\mathbf{H}_e(\mathbf{q}, \mathbf{R})$). We define the $\mathbf{L}$ and $\mathbf{S}$ projections onto the inter-nuclear axis, $\mathbf{A}$, by $\mathbf{\Lambda}$ and $\mathbf{\Sigma}$ respectively. In addition, this defines another conserved quantity known as the total molecular angular momentum given by $\mathbf{\Omega} = \mathbf{\Lambda} + \mathbf{\Sigma}$. The set of good quantum numbers $\{J, S, \Lambda, \Sigma, \Omega\}$ now define a molecular basis set, and can be used to label

electronic eigenstates as follows:

$$(n)^{2S+1}\Lambda^{\pm}_{\Omega,g/u},\tag{2.13}$$

where $S = \{0, \frac{1}{2}, 1, ...\}$ is the electronic spin quantum number and we describe the corresponding molecular state as either a singlet, doublet, triplet,... respectively. The electronic label n denotes the eigenstate of $\mathbf{H}_e(\mathbf{q}, \mathbf{R})$ similar to the atomic principle quantum number. These are typically labelled, in terms of increasing energy, $n = X, A, B, C, ...$ (for experimentalist) or $n = 0, 1, 2, 3, ...$ (for theorist), while excited states of different spin multiplicity to that of the ground electronic state use lower cases letters $n = a, b, c, ...$. The states corresponding to the value of the projection of
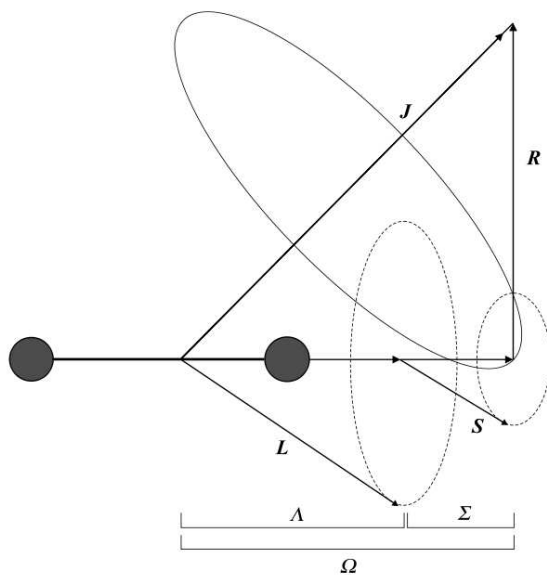
Figure 2.1: Hund's case (a) angular momentum and good quantum numbers.[1].

the orbital angular momentum on the molecular axis $\Lambda = 0, \pm 1, \pm 2, ...$ are designated as Σ, Π, Δ,... respectively. The double degeneracy of these states (whenever $\Lambda \neq 0$) may be lifted through the interaction of $\mathbf{R}$ and $\mathbf{L}$ (Λ-doubling), however this only becomes important for high rotational speeds (large J values), and will not be encountered in this thesis. The $\pm$ and g/u in Eq. (2.13) specifies symmetries

of the electronic wavefunction. For $\Lambda = 0$ (*i.e.* Σ states), the $+$ (even) or $-$ (odd) represent the symmetry with respect to a reflection in the plane containing the inter-nuclear axis. Then for homonuclear diatomics, there exist a symmetry of the wavefunction about the inversion center which can either be *gerade* (g,even) or *ungerade* (u,odd). These symmetries will become important when considering transitions between different electronic states (in Sec. (2.2.2)).

Another important basis set which will be encountered arises from Hund's case (c). In this situation the spin-orbit interaction, $\{\mathbf{L}, \mathbf{S}\}$, is stronger than their individual interactions with the internuclear axis ($\mathbf{A}$). The projections, $\mathbf{\Lambda}$ and $\mathbf{\Sigma}$, can not longer be defined, and it is the projection of the $J_\alpha = \mathbf{L} + \mathbf{S}$ vector onto $\mathbf{A}$ that defines $\mathbf{\Omega}$. Just as in case (a), the doubly degenerate $\Omega \neq 0$ states are split with the inclusion of rotation (Ω-*doubling*), though these effects won't be considered here. Most notable, is that these electronic states now exhibit avoided-crossings, a fact which will be returned to in Sec. (2.1.2).

Lastly, it should be mentioned that because the couplings associated with the nuclear spin angular momentum ($\mathbf{I}$), which give rise to hyperfine structure in molecules, are much smaller than all other couplings, they will be ignored throughout this work. See Ref. [1] for more details and a descriptions of the Hund's cases.

Vibrational and Rotational Energies

Each distinct electronic eigenenergy, $(n)^{2S+1}\Lambda^\pm_{\Omega,g/u}$, defines a PES in the nuclear coordinates for a molecule's vibrations and rotations. In order to study these vibrational and rotational states we begin with two further approximations. Assuming that there exist a minimum to the electronic PES ($V(R_e)$), instead of an unstable electronic state in which the two atoms repel each other for all values of R, then one can Taylor expand about this equilibrium distance (R_e) to second order giving

$$V(R) \approx V(R_e) + \frac{k_e}{2}(R - R_e)^2 \ . \tag{2.14}$$

This is known as the *harmonic approximation* where k_e is the force constant of the molecular bond which relates to the oscillation frequency through $\omega_e = (k_e/\mu)^{1/2}$.

Then using the centrifugal potential term (Eq. (2.12)) the rotational frequency of the molecule can also be estimated as $\omega_r \approx 1/(\mu R^2)$. Therefore, we find that for a typical molecule the ratio between these frequencies is $\omega_e/\omega_r \sim \mathcal{O}(10^2 - 10^3)$, so it can be assumed that a molecule generally rotates at the midpoint of its vibrational

oscillation, namely at the internuclear distance R_e. This allows us to apply the *rigid rotor approximation*, replacing R with R_e in the centrifugal potential. Now by solving the radial Schrödinger equation (Eq. (2.11)) with these simplified potentials we find the rovibrational energies

$$E_{\nu,l} = V(R_e) + B_e l(l+1) + \omega_e(\nu + 1/2) \ , \qquad (2.15)$$

where $B_e \equiv 1/(2\mu R_e^2)$ is known as the rotational constant, $l = \{0, 1, 2, ...\}$ is the rotation quantum number, and $\nu = \{0, 1, 2, ...\}$ is the vibrational quantum number. Higher order corrections in both the vibrational and rotational potentials can be used to improve the above result, namely,

$$E_{\nu,l} \quad = \quad V(R_e) + G(\nu) + B_\nu l(l+1) - D_\nu[l(l+1)]^2 + H_\nu[l(l+1)]^3 - (2.16)$$

$$\text{where} \quad G(\nu) = \omega_e(\nu + 1/2) - \omega_e x_e(\nu + 1/2)^2 + \omega_e y_e(\nu + 1/2)^3 + ... (2.17)$$

The unfamiliar coefficients in $E_{\nu,l}$ are the so-called *band constants* which account for centrifugal distortions in the rotational motion. The additional coefficients in $G(\nu)$, called the vibrational constants, provide anharmonic corrections to the quadratic approximation. Together these series of constants which can be obtained from experimental measurements are known as the *spectroscopic constants*. In Sec. (3.1) this model will be further discussed in the context of determining electronic potential energy surfaces.

Another common approach to account for the anharmonicity of a molecular PESs is through modeling the electronic potential using a Morse function

$$V(R) \quad = \quad D_e \left(e^{-2\beta(R-R_e)} - 2e^{-\beta(R-R_2)} \right) + D_e \qquad (2.18)$$

where the (Morse) parameters $\beta = \sqrt{2\mu\omega_e\chi_e}$ and $D_e = \omega_e/(4\omega_e\chi_e)$ control the width and depth of the well, respectively. In Fig. (2.2) ([2]), a typical Morse potential (dashed-curve) is shown together with a realistic PES of Be_2. As expected, the curves agree very well about the equilibrium position (minimum of the potential) and along the repulsive wall but diverge at longer range. Alternatives to the Morse functions for describing PESs will be discussed in Secs. (2.4,3.1). However, this form captures the effect of the anharmonicity of the PES, whereby rovibrational levels get increasingly closer together as the vibrational quantum number ν increases. Eventually, when the potential energy function reaches zero (at the dissociation energy), the molecule
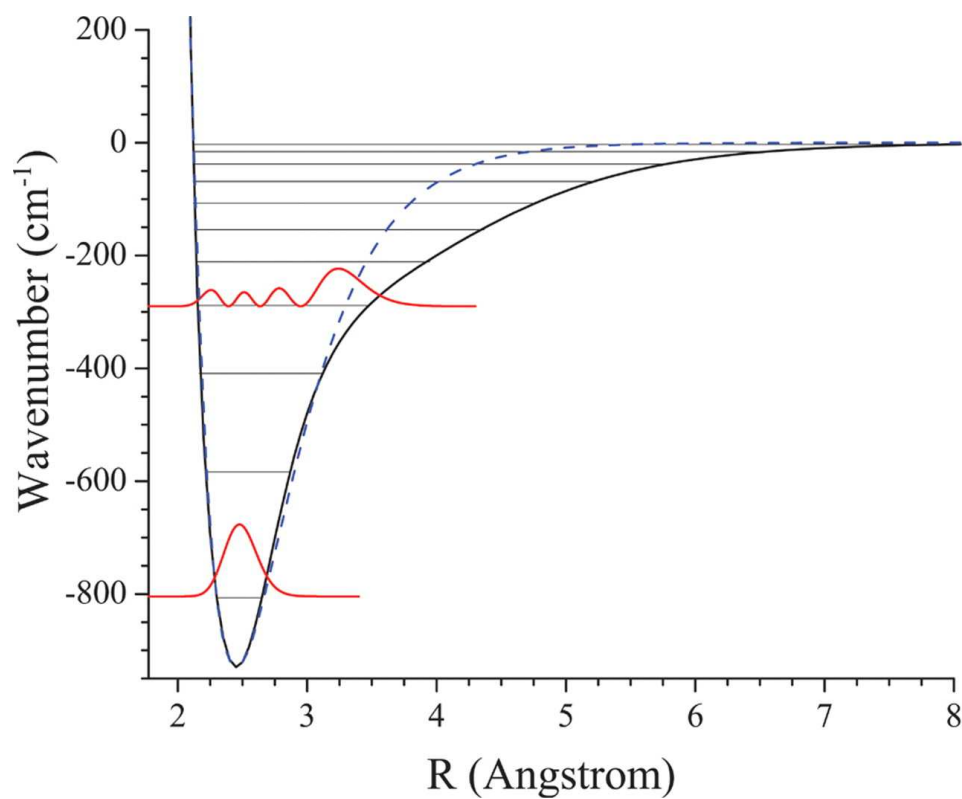
Figure 2.2: Ground electronic state potential energy curve of the beryllium dimer. The vibrational wave functions for $\nu = 0, 3$ are also shown for reference. The dashed curve is a Morse potential constructed to reproduce the experimental dissociation energy and harmonic vibrational constant [2].

is no longer bound and the difference in energy between successive quantum states vanishes forming an energy continuum. Note that the dissociation energy may be measured either from the bottom of the potential (D_e, as in Eq. (2.18)), or from the zero point vibrational energy, in which case it is called D_0.

Continuum States

Above the dissociation limit the vibrational energy of the continuum state(s) are no longer quantized; consequently, these vibrational wave functions ($\psi_{E,l}(R)$) are labeled by the quantum number, E (for energy). Unlike the bound state eigenstates which can be "space-normalized" since $\psi_{\nu,l}(R) \xrightarrow{R \to \{0, \infty\}} 0$, the continuum function must be "energy-normalized" because $\psi_{E,l}(R) \neq 0$ for $R \to \infty$. A general treatment of continuum (scattering) states is beyond the scope of this work (see Ref. [50] on Scattering Theory), instead these states will be approximated in terms of *quasi-continuum* states using the method of *Box-Normalization*. By adding a vertical and infinite barrier at large internuclear distance above the dissociation energy the continuous spectrum can be artificially discretized into a set of quasi-continuous levels. These quasi-continuous states, now "bound" within a region of space, can now be space-normalized to unity. However, notice that the location of this outer wall would affect the amplitude and density of these discrete levels, thereby influencing their behaviors and couplings within the system. So care must be taken in characterizing these states if they are to be treated as ordinary vibrational bound states. In particular, note that the product of the amplitude times the density of states remains a constant, finite value as the barrier goes to infinite internuclear distance; even when the amplitude of each wavefunction goes to zero, and the density of states becomes infinite, thereby returning to a continuous spectrum. See Sec. (2.4.3) for a comparison of the transition dipole couplings between bound–continuum states derived using the artificial channel method [51–53], and the bound–quasi-continuum states.

Diabatic and Adiabatic Curves

In this section we will go beyond the Born-Oppenheimer(BO) approximation and discuss the perturbations that arise from the *off-diagonal* elements of the molecular Hamiltonian $\mathbf{H}(\mathbf{q}, \mathbf{R})$ in the BO basis. The exact eigenvalues and eigenfunction of $\mathbf{H}(\mathbf{q}, \mathbf{R})$ can always be expressed as an infinite linear combination of *any* set of basis

states, however, as Lefebvre-Brion and Field state: the BO wavefunctions of Eq. (2.5) are the "only available type of complete, rigorously definable basis set" [48].

There are two different representations of the BO basis that will be most useful. We have already encountered one, known as the *diabatic* basis, in which the electronic wavefunctions, $|\Psi_{e,i}^d\rangle$, are defined such that

$$\langle \Psi_{e,j}^d |\mathbf{T}_N| \Psi_{e,i}^d \rangle = 0 \tag{2.19}$$

In this case, the *off-diagonal* elements of $\mathbf{H}_e$ give rise to either *electrostatic* perturbations from V_{ee} for states with identical electronic symmetry (equal Λ, Σ, S), or *spin-orbit* couplings, upon inclusion of a *relativistic* perturbative operator, $\mathbf{H}_{SO}(\mathbf{q}, \mathbf{R})$, to the non-relativistic Hamiltonian $\mathbf{H}_e$, between states of different Λ, S, but the same $\Omega = \Lambda + \Sigma$. Because the diabatic functions are not exact solutions of the electronic Hamiltonian (*i.e.* $\langle \Psi_{e,j}^d |H_e| \Psi_{e,i}^d \rangle \neq 0$), these PESs are able to exhibit crossings.
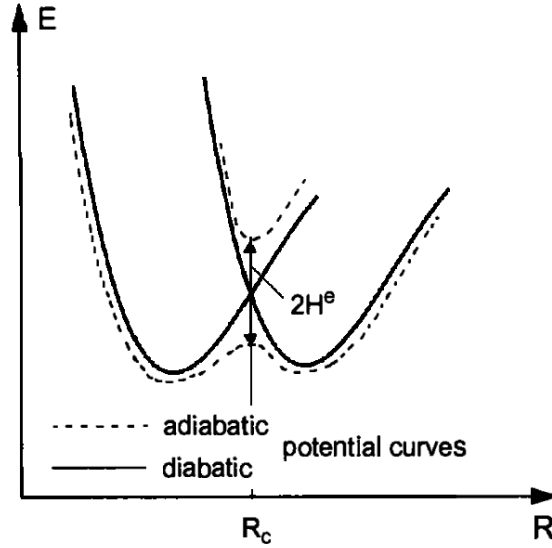
Figure 2.3: Diabatic (crossing) potential energy curves cross at R_c as a result of neglecting the part of $\mathbf{H}_e$ that causes the adiabatic (non-crossing) curves' *avoided-crossing* by $2H_e$ [3].

Alternatively, the *adiabatic* functions, $|\Psi_{e,i}^{ad}\rangle$, which are defined as the exact

solutions to $\mathbf{H}_e$,

$$\langle\,\Psi^{ad}_{e,j}\,|\mathbf{H}_e|\,\Psi^{ad}_{e,i}\,\rangle = 0, \tag{2.20}$$

take into account the electronic couplings between the diabatic functions and lead to PESs with an *avoided-crossing* proportional to the strength of the interaction (see Fig.2.3). This occurs due to the non-crossing rule of von Neumann and Wigner [54] (initially proposed by Hund [55]), which states that for diatomic molecules there cannot exist a degeneracy in the electronic states (which would occur at a crossing point). The perturbations in the adiabatic basis, known as *non-adiabatic inter-actions*, now arise due to the off-diagonal elements of the nuclear kinetic energy operator, $\mathbf{T}_N(\mathbf{R})$.

We leave this discussion here (see Ref. [3] for more details), noting, as in Fig.2.3, how PES with double minima may arise. Unless stated otherwise, this thesis will work in the diabatic picture in which interactions between curves (when they occur) are introduced as off-diagonal elements in the electronic Hamiltonian in the unperturbed basis. However, the diabatic states are not unique, unlike in the adiabatic case, their form can change along with the interaction terms yielding the same electronic Hamiltonian. Lastly, because this presentation will focus on rotationless states ($J = 0$), the *rotational* and *spin-rotation* perturbations will not be addressed. In addition, the matrix elements associated with *spin-spin* couplings will be ignored due to their relative weakness to those of the *spin-orbit* terms.

2.1.3 Polyatomic Molecules

Determining the molecular structure of polyatomic molecules becomes increasingly more difficult as one increases the number of constituent atoms. This is a consequence of the many more nuclear degrees of freedom (DOF) that become available such as additional stretching, bending, and torsional motions. In general, the potential energy of a polyatomic molecule is given as a function in $3N - 3$ dimensions, where $3N$ defines the number of independent coordinates available to $N \geq 3$ number of atoms in free space, and, three coordinates are required to specify the center of mass of the body. By solving separately for the rotational motion through introducing constants for the angular momentum, the DOF of the effective potential (potential plus centrifugal terms) reduces to $3N - 6$ since three more DOF are used to define the object's orientation in space. The remaining coordinates for specifying the molecular structure will now consist of internuclear distances and/or bond

angles, and it should be evident that for molecules with more than three atoms (or those triatomics in which the bond lengths and angles are independent), it will not be possible to plot and fully visualize the potential energy surface (PES).

Another complication in the description of polyatomics is that the internal coordinates (distances, angles) do not generally form an orthogonal set. This implies that there exist non-zero off-diagonal terms in the Hamiltonian for the kinetic energy, *i.e.* couplings between the normal modes. However, it is possible to abandon the normal modes picture and define a new set of coordinates which are linear combinations of the internal coordinates where the kinetic energy operator becomes diagonal [56] (although there exist an infinite number of these sets). The only polyatomic molecules with a reasonable simple form of the kinetic energy operator are the linear triatomics, which can be described by a set of three coordinates.

As we saw for diatomic molecules, with a single vibrational DOF, when two electronic states possess the same symmetry, we encounter an avoided crossing. However, for polyatomic molecules, which have multiple vibrational DOF, the crossing of such electronic states is possible, and leads to a structure known as a conical intersection (CI). The CI is a $3N - 8$ dimensional subspace in which the two electronic states of the same spatial/spin symmetry are allowed to cross, because their energies remain degenerate. The two-dimensional space that lifts this degeneracy is spanned by two vectors relating the two intersecting electronic states: namely, the difference of their energy gradient vectors, and their non-adiabatic coupling vectors. When the PES is plotted as a function of these two vectors, we observe a pair of cones meeting at the degeneracy point, and separated by the branching plane that lifts the degeneracy, leading to the name "conical intersection". The occurrence of conical intersections is often a result of the Jahn-Teller theorem [57] which states that a nonlinear molecular with a spatially degenerate electronic state will spontaneously distort its configuration to that of a reduced symmetry in order to lower its overall energy.

When two adiabatic PES come close to each other, as they do in the vicinity of conical intersections, the vibronic coupling becomes large leading to a breakdown of the BOA (and giving rise to such non-adiabatic phenomena as radiationless decay). The coupling of different electronic states through nuclear vibration occurs often in polyatomics due to the many nuclear DOF and large number of energetically close electronic states.

Now we begin to appreciate the complexity of performing spectroscopic studies

on polyatomic systems. Even for the simplest case of linear triatomics, there exist three internal DOF, and many of the electronic states are two fold degenerate, leading to the Renner-Teller effect [58] in which strong mixing occurs between Born-Oppenheimer terms. In lieu of the difficulties associated with polyatomic molecules, this thesis will proceed with diatomics in mind. However, the work to come, will, in principle, be application to both diatomic and polyatomic systems.

2.2 Light-Matter Interaction

In this section we provide a basic overview of the theory of light-matter interactions, in particular, as it pertains to diatomic molecules. The most general approach uses the quantum electrodynamics Hamiltonian

$$H = H_0 + H_f + H_{int} \tag{2.21}$$

where the system, H_0, the electromagnetic (EM) field, H_f, and their interaction, H_{int} Hamiltonians are all treated quantum mechanically. However, the majority of molecular experiments involve high photon densities and thus it can be assumed that the EM Hamiltonian can be described classically (*i.e.* by Maxwell's equations). This opens the door for a semi-classical treatment of the light-matter interactions, in which the matter is treated as an unperturbed quantum mechanical (QM) system (*e.g.* the Born-Oppenheimer rovibrational Hamiltonian $H_N(\mathbf{R})$) and the influence of the classical EM field becomes a QM perturbation.

2.2.1 Semi-Classical Theory

The semi-classical approach provides use with the ability to develop an intuitive picture of the light-matter interaction, and allows use to develop a theory necessary for manipulating and studying the internal structure of molecules. For our purposes we will use only the first (and in our cases dominate) term of the dipole expansion of H_{int} (*e.g.* ignoring higher multipole terms such as the electric-quadrupole or magnetic-dipole); this is known as the *electric-dipole approximation*. Moreover, we will make use of the *large-wavelength approximation*, assuming that our EM field is homogeneous field over the molecular dimensions, and thus the spatial variation of field can be ignored. With these simplifications, the interaction Hamiltonian can be written as a scalar product of the electric transition dipole moment operator,

$\boldsymbol{\mu}_e = -\sum_j e\mathbf{q}_j$, and the time-dependent electric field, $\boldsymbol{\varepsilon}(t)$,

$$H_{int}(\mathbf{q}, t) = \boldsymbol{\mu}_e(\mathbf{q}) \cdot \boldsymbol{\varepsilon}(t) , \qquad (2.22)$$

where q_i specifies the position of the jth electron and t represents time. Here we have ignored the nuclear contribution to the dipole moment because it drops out of the molecular transition matrix

$$H^{i,f}(t) = \langle\, \Psi^f(\mathbf{q}, \mathbf{R})\, |\boldsymbol{\mu}_e(\mathbf{q}) \cdot \boldsymbol{\varepsilon}(t)|\, \Psi^i(\mathbf{q}, \mathbf{R})\, \rangle , \qquad (2.23)$$

which quantifies the transition amplitude between some initial, $\Psi^i(\mathbf{q}, \mathbf{R})$, and some final, $\Psi^f(\mathbf{q}, \mathbf{R})$, eigenstate of the full molecular Hamiltonian H_0. Upon applying the BOA, we can simplify Eq. (2.23) to

$$H^{i,f}(t) = \langle\, \psi_N^f(\mathbf{R})\, |\boldsymbol{\mu}_e^{i,f}(\mathbf{R}) \cdot \boldsymbol{\varepsilon}(t)|\, \psi_N^i(\mathbf{R})\, \rangle \qquad (2.24)$$

where the *electronic transition dipole surface*, $\boldsymbol{\mu}_e^{i,f}(\mathbf{R})$, is defined as

$$\boldsymbol{\mu}_e^{i,f}(\mathbf{R}) = \langle\, \Psi_e^f(\mathbf{q}; \mathbf{R})\, |\boldsymbol{\mu}_e(\mathbf{q})|\, \Psi_e^i(\mathbf{q}; \mathbf{R})\, \rangle \qquad (2.25)$$

The series of approximations leading to this expression of the probability amplitude for a transition from an initial state $|\,i\,\rangle$ to a final state $|\,f\,\rangle$ is known as the *Franck-Condon (FC) principle.* In regards to the interaction, this assumes that the transition time is short relative to changes in the nuclear configuration, thus the amplitude of the transition is related to the degree with which both the initial and final electronic ($\Psi_e^i(\mathbf{q}; \mathbf{R})$) and nuclear ($\psi_N^i(\mathbf{R})$) wavefunctions overlap respectively. As a result, electronic transition are more likely to occur at the classical turning points where the momentum is zero, and where the nuclei spend most of their time. In addition, it is often assumed (in the *Condon approximation*) that the nuclear coordinate dependence of transition dipole surface (TDS) is rather smooth, thus it can be written as an average value over the nuclear coordinates $\mathbf{R}$, $\boldsymbol{\mu}_e^{i,f}(\mathbf{R}) \approx \overline{\boldsymbol{\mu}}_e^{i,f}$). Then, the strength of a transition within molecules becomes modulated by only the FC factor $\langle\, \psi_N^f(\mathbf{R})\,|\,\psi_N^i(\mathbf{R})\,\rangle$ (up to O(1)). However, the largest determinant of the transition probability is found through molecular selection rules (see Sec. (2.2.2)), though we will find that these selection rules are not always valid, either due to the breakdown of the BOA or due to contributions from weaker multipole moments.

2.2.2   Molecular Transitions

Before presenting the selection rules that largely govern molecular transitions, we will first review the internal transitions available within molecules. These can be divided into two main groups: *radiationless transitions* resulting from collisions or couplings to the physical environment, and *radiative transitions* which evolve an interaction of electromagnetic (EM) fields with the eigenstates of a molecule.

Radiationless Transitions

A radiationless transition can occur as a result of an inelastic collision of a molecule with its surroundings. Often this is a de-excitation process in which internal molecular energy (electronic, vibrational or rotational) is transferred into kinetic energy. An excited electronic state of a molecule in a given vibrational level (rotational states are not considered for simplicity) may undergo three sorts of transitions. These are conveniently represented in the Jablonski diagram Fig. (2.4) as internal conversion (IC), intersystem crossing (ISC), and vibrational relaxation (VR), where the S_i and T_i represents the ith singlet and triplet electronic states respectively. Within a given electronic state, S_i or T_i, a molecule's vibrational energy will gradually decrease over time as a result of thermal collisions causing VR. Once either in the ground vibrational state or before of a given S_i (T_i) state, collisional energy transfer may result in a change of the electronic state to one of the same spin multiplicity S_{i-1} (T_{i-1}) for IC, or one of a different spin multiplicity T_j (S_k) as in ISC. As a result, a dense ensemble of excited molecules, uninfluenced, will usually decay by a series of radiationless transitions from excited electronic and vibrational states to a ground state Boltzmann distribution (see Sec. (2.3.1)). Note that nearly any energetically allowed transition is possible between electronic, vibrational and rotational states as a result of an inelastic collision. The well-known molecular selection rules which limit allowed transitions, occur due to electric-dipole couplings in the BOA, this discussed in Sec. (2.2.2).

Because these nonradiative processes cannot be quantified or measured, they are detrimental to molecular spectroscopist or those designing quantum control schemes (See Sec. (2.3.1) on *dephasing*). Fortunately, the mean time between collisions of particles in a gas can be controlled via the pressure, density, and temperature, and in this work we will assume that the collisions occur on a nanosecond (ns) timescale for the small molecular species of interest [59, 60].
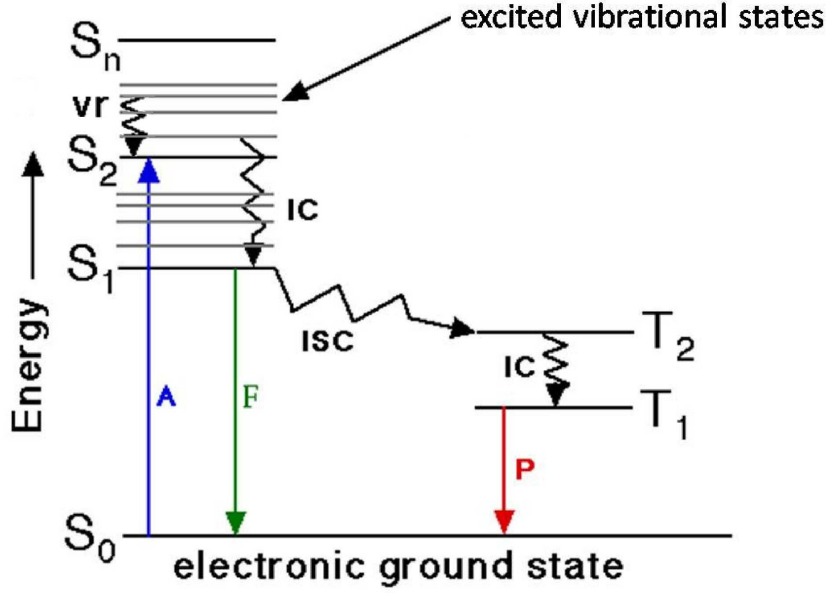
Figure 2.4: Jablonski diagram where: S = single state, T = triplet state, A = absorbance, F = fluorescence, P = phosphorescence, IC = internal conversion, ISC = intersystem crossing, and VR = vibrational relaxation.

Radiative Transitions and Selection Rules

Radiative transitions result from the absorption or emission of one (or more) photons, these are shown in Fig. (2.4) as: absorption(A), fluorescence(F) and phosphorescence(P). The mathematical details of these transitions will be discussed in Sec. (2.4).

At the moment our interest will be in estimating which transitions are permitted within a diatomic molecule interacting with an EM field in the dipole approximation. From Eq. (2.23), we write the probability amplitude for a transition in the BOA as

$$A \quad \propto \quad \langle \, \Psi_e^f \psi_N^f \, | \boldsymbol{\mu}_e \cdot \hat{\epsilon} | \, \Psi_e^i \psi_N^i \, \rangle \tag{2.26}$$

$$A \quad \approx \quad \langle \, \psi_e^f \chi_s^f \psi_{rot}^f \psi_{vib}^f \, | \boldsymbol{\mu}_e \cdot \hat{\epsilon} | \, \psi_e^i \chi_s^i \psi_{rot}^i \psi_{vib}^i \, \rangle \tag{2.27}$$

where we have expanded the electronic wave function, Ψ_e, to include both the spatial, ψ_e, and the electron spin, χ_s, components. And, the nuclear wave function, ψ_N, has been separated into rotational, ψ_{rot}^i, and vibrational, ψ_{vib}^i, parts. The canonical selection rules are expressed from the point of view of the Hund's case (a) basis which

exclude spin-orbit coupling, thus we can separate the electronic wavefunction into the orbital and spin terms $(|n\Lambda\rangle|\Sigma, S\rangle)$. By omitting the rotational-vibrational coupling we can specify the vibrational and rotation eigenstates in terms of their quantum numbers ν and J respectively (*i.e.* $\psi_{vib} = |\nu\rangle$ and $\psi_{rot} = |J\rangle$), where J should not be confused with the total electronic angular, but equals the l rotational quantum number from earlier (following convention).

Thus we rewrite Eq. (2.26) in terms of these quantum numbers corresponding to their appropriate wavefunctions

$$
\begin{aligned}
A &\approx \langle\psi_e^f|\mu_e|\psi_e^i\rangle\langle\chi_s^f|\chi_s^i\rangle\langle\psi_{rot}^f|\hat{\mu}_e\cdot\hat{\epsilon}|\psi_{rot}^i\rangle\langle\psi_{vib}^f|\psi_{vib}^i\rangle \\
&= \langle n^f\Lambda^f|\mu_e|n^i\Lambda^i\rangle\langle\Sigma^f, S^f|\Sigma^i, S^i\rangle\langle J^f, m_J^f|\hat{\mu}_e\cdot\hat{\epsilon}|J^i, m_J^i\rangle\langle\nu^f|\nu^i\rangle \quad (2.28)
\end{aligned}
$$

where we have included the quantum number $m_J = \{-J, ..., J\}$ labelling the rotational sublevels.

The first term in Eq. (2.28) yields the electronic orbital selection rules associated with transitions between $n\Lambda_{g/u}^{\pm}$ states:

$$
\Delta n \neq 0 \qquad \Delta\Lambda = 0, \pm 1 \qquad \pm \leftrightarrow \pm \qquad g \leftrightarrow u . \qquad (2.29)
$$

Recall that the $\pm$ refer to the reflection symmetry of $\Lambda = \Sigma$ state, and g/u represents a symmetry with respect to inversion for homonuclear diatomics. For the spin component of the electronic wavefunction we have the simple requirement that $\Delta S = 0$, since operators governing transitions are diagonal in S in the absence of spin-orbit coupling. The third term, known as the *Hönl-London factor*, involving the rotational wavefunctions gives rise to the rules:

$$
\Delta J = \pm 1 (\Delta\Lambda = 0) \qquad \Delta J = 0, \pm 1 (\Delta\Lambda = \pm 1) . \qquad (2.30)
$$

Moreover, there is a dependence of the m_J sublevel couplings on the polarization of the electric field $\hat{\epsilon}$. Linear polarized light (*e.g.* $\hat{\epsilon} = \hat{z}$), which we will used throughout this thesis, requires that $\Delta m_J = 0$, whereas a circularly polarized field (*e.g.* $\hat{\epsilon} = \hat{x} \pm \hat{y}$) permits only $\Delta m_J = \pm 1$ transitions. Lastly, the inner product of the vibrational wavefunction do not define a selection rule and simply provides the previously discussed Franck-Condon (FC) factor.

Thus, we find that a single photon electric dipole transition will occur between two different electronic states for all $\Delta\nu$, however if $\Delta\Lambda = 0$ then there must be a

change in the rotational state, $\Delta J \neq 0$, as shown in Eq. (2.30). This restriction results from parity conservation, whereby the absorption or emission of a photon (with parity -1) must change the parity of the overall wavefunction. We will refer to these bound-bound transitions between rovibrational states where $\Delta J =$ -1, 0, or +1 as P, Q, or R branches respectively. We must keep in mind that these selection rules, and the concept of the Franck-Condon factor, come about from a series of assumptions, most notably through application of the BOA which permits a factorization of the total wavefunction into nuclear, electronic spatial and spin wavefunctions, and the omission of vibrational and rotational coupling between states. As a result, these rules may not always be strictly observed, however they will serve suitable well for our investigation.

Before continuing, we make a quick comment on the phenomenon of phosphorescence. In particular, for phosphorescence to occur there must exist spin-orbit coupling between some excited diabatic singlet (S_i) and triplet (T_j) states (which is not necessary for nonradiative ISC). This "singlet-triplet transition" in fact is "allowed" only because the triplet state obtains some singlet character as we shall see in Sec. (5.3.2). Together with nonradiative effects, phosphorescence can result in the very long lifetimes ($\gtrsim$ 1s), compared to the relatively short lifetimes (100ps-10ns) of fluorescent states. Studying this form of radiation is beyond the scope of this work, however, it plays an important role in acting as metastable states, capable of storing energy, for instance, where it can act as reaction intermediate in photosystem II in electron-transfers reactions [61].

2.3 Laser Excitations in Molecules

Unless stated otherwise, for the remainder of this thesis we will assume that we are working with a gaseous ensemble of molecules. In this section we discuss the nature of such systems and discuss their behavior in the presence of electric fields. In particular, we focus on the internal dynamics of molecules by looking at the origin of coherence and the behavior of molecular wavepackets. This will set the stage for understanding the time- and frequency-dependent molecular spectroscopy in the section to come.

2.3.1 Molecular Ensemble

In the BOA there exist a set of nuclear wavefunctions, $\psi_N(\mathbf{R})$, for each electronic PES, $\boldsymbol{E}_e(\mathbf{R})$. The amplitude of these quantized stationary eigenstates reflect the probability distribution, in the coordinates $\mathbf{R}$, of observing a nuclei at that position. Under typical conditions a molecule doesn't exist in a single eigenstate but in a thermal ensemble of multiple internal quantum states following the Boltzmann distribution

$$g_i e^{-E_i/(k_b T)}, \tag{2.31}$$

where g_i and E_i is the degeneracy and energy of a state i relative to the overall ground state of the molecule respectively. k_b is the Boltzmann factor and T is the temperature.

Given that for the typical diatomic molecule the spacings between vibrational levels is $\mathcal{O}(10^3)$ Kelvin (K), and the separation between rotational levels is only a few K, then at ordinary temperatures (100's K), a molecule will reside in its ground vibrational state $\nu = 0$, and in a distribution of several rotation levels J following Eq. (2.31). For instance, we can calculate and find the rotational state with the maximum population as $J_{max} = (\sqrt{2k_b T/B} - 1)/2$, where B is the rotational constant.

Due to the nature of thermal excitations, such superpositions of eigenstates would be incoherent, that is, there wouldn't be a fixed phase relation between the individual, $\psi_{vib}\psi_{rot} = |\,\nu = 0, J\,\rangle$, levels. An example is an ensemble of molecules at room temperature in which all of the diatomic molecules will be rotating out of phase with each other. To addresses this fundamental problem of controlling a system having an initial state that is an incoherent thermal mixture of different states, we can prepare a molecule in a single quantum state $\langle\,\mathbf{R}\,|\,\nu, J\,\rangle \equiv \psi_N^{(\nu,J)}(\mathbf{R})$, by insuring that the translational (kinetic) energy be reduced to below 1 K (for a relatively light molecule) such that the thermal energy $k_b T$ is smaller than the rotational energy spacing. In this way our ensemble of molecules will begin in a single $|\,\nu = 0, J = 0\,\rangle$ state. Note that throughout this thesis we will average over all hyperfine levels which have spacing of $\mathcal{O}(10^{-2})$ K. From this initial state, a coherent process can be used, such as from a *laser* field, to transfers coherence to the ensemble of molecules.

2.3.2 Excitation Laser Fields

We define our laser (light amplified by stimulated emission of radiation) field as

$$
\begin{aligned}
\varepsilon(t) &= \varepsilon(t)\hat{\epsilon} \\
&= \mathcal{E}(t)\cos(\omega_0 t)\hat{\epsilon} ,
\end{aligned}
\tag{2.32}
$$

where $\mathcal{E}(t)$ represents the (complex) pulse envelope of the field, and ω_0 is the carrier frequency. Unless stated otherwise the polarization of the field, $\hat{\epsilon}$, will be linear and along the $\hat{z}$ direction in the laboratory frame. It will be useful to represent the complex-valued electric field also in frequency-space by its inverse Fourier integral

$$
\begin{aligned}
\varepsilon(t) &= \int_{-\infty}^{\infty} d\omega \varepsilon(\omega)e^{-i\omega t} \\
&= \int_{-\infty}^{\infty} d\omega |\varepsilon(\omega)|e^{i\phi(\omega)}e^{-i\omega t}
\end{aligned}
\tag{2.33}
$$

where $|\varepsilon(\omega)|$ and $\phi(\omega)$ are the magnitude and phase of the field at the frequency ω, respectively. In addition, we define the time averaged intensity and the period averaged spectral intensity of a slowly varying pulse as follows:

$$
\langle I(t) \rangle = \frac{c}{8\pi}|\varepsilon(t)|^2 , \qquad \langle I(\omega) \rangle = \frac{c}{16\pi^2}|\varepsilon(\omega)|^2 .
\tag{2.34}
$$

Ultrashort Pulses and Pulse Shaping

A property of the Fourier transform is that the time-bandwidth product of a Gaussian laser pulse is approximately fixed at

$$
\Delta\tau\Delta\omega \approx 0.441 ,
\tag{2.35}
$$

where $\Delta\tau$ and $\Delta\omega$ are the full-width-half-maximum (FWHM) of the two intensity profiles of Eq. (2.34) respectively. So we observe a broadening occurring to a pulse's frequency bandwidth upon a reduction of its temporal width, with the precise value of Eq. (2.35) depending on the shape of the pulse envelop (*e.g* hyperbolic-secant-squared $= 0.315$) [62].

It has become common to generate pulses of only a few femtoseconds (fs), known as *ultrashort* pulses, consisting of only a few optical cycles. The standard approach involves pumping a mode-locked oscillator with a continuous-wave (cw) laser field.

In this case there exist a fixed phase between the modes of the optical cavity, and the modes will periodically all constructively interfere with one another leading to an intense pulse of light with a duration determined by the number of modes which are oscillating in phase [63]. For more information on ultrashort laser fields refer to Ref. [62].

Another tool which has become vital to study and observe molecular quantum dynamics on short time scales is pulse shaping. Given a femtoseconds pulse in the visible spectrum, the electric field can be modulated in the frequency domain like

$$\varepsilon(\omega)_{mod} = M(\omega)\varepsilon(\omega) \ , \tag{2.36}$$

where $M(\omega)$ is the modulation function of a spatial light modulator capable of manipulating the spectral amplitude, phase or polarization, with common resolutions of approximately 0.5 nm (or 10 cm^{-1}) [64]. Note that this energy is at least an order of magnitude smaller than spacing between vibrational levels. Finally, returning this shaped pulse back into the time domain requires an inverse Fourier transform (IFT)

$$\varepsilon(t)_{mod} = \frac{1}{2\pi} \int_{-\infty}^{\infty} M(\omega)\varepsilon(\omega)e^{i\omega t}d\omega \ . \tag{2.37}$$

These ultrashort pulses with large bandwidth allow for the simultaneous excitation of several molecular eigenstates, and by tuning pulses' temporal and spectral profiles we are able to prepare a molecule in very particular electronic, vibrational, rotational states.

Perturbation Theory

Using the assumptions and results of Sec. (2.2), we are ready to solve the time-dependent Schrödinger equation for a molecule in the presence of an EM field

$$i\frac{\partial \Psi(t)}{\partial t} = \left(\boldsymbol{H}_N + \boldsymbol{H}_{int}(t)\right) \Psi(t) \ , \tag{2.38}$$

where H_N represents the nuclear Hamiltonian in the Born-Oppenheimer approximation with (rovibrational) eigenstates $\psi_N = |\,\nu, J\,\rangle$, and H_{int} is given by Eq. (2.22). The wavefunction of the interacting system can be expanded in the unperturbed

basis (omitting electronic spin states) as

$$| \Psi(t) \rangle = \sum_q \sum_j \sum_k c_{q,j,k}(t) e^{-i E_{q,j,k} t} | n_q \Lambda_q \nu_j J_k \rangle \tag{2.39}$$

where $E_{q,j,k}$ is the energy of the $(j,k)^{th}$ rovibrational level, and the square of the coefficients $c_{q,j,k}(t)$ give the population in a given state $| \nu_j J_k \rangle$, within the qth electronic state. The elements of the interaction Hamiltonian between some initial state i and a final state f can be written as (from Eq. (2.22))

$$H_{g,e}^{i,f}(t) \approx \epsilon(t) d_{g,e}^{i,f} \tag{2.40}$$

where we define the electronic transition dipole moment (TDM) as

$$d_{g,e}^{i,f} = \langle \nu^f, J^f | \boldsymbol{\mu}_{g,e} \cdot \hat{\epsilon} | \nu^i, J^i \rangle . \tag{2.41}$$

Here we have simplified the notation by defining $\mu_{g,e}$ as the radial dependent electronic transition dipole function between a ground, g, and an excited, e, electronic state (different n's and Λs). In the case of electronically forbidden transitions this dipole function will thus tend to zero. For simplicity, the initial, i, and final, f, eigenstates of these different electronic potentials will now only be specified by their rovibrational quantum numbers ν and J. The M_J indices are not included since we will assume that the rotational sublevels will remain approximately degenerate, and the Σ, S labels become superfluous in the absence of spin-orbit coupling.

Now, if we take θ to be the angle between $\boldsymbol{\mu}_e(\mathbf{q})$ and $\boldsymbol{\varepsilon}(t)$, where we assume that the EM field is linearly polarized, then

$$H_{g,e}^{i,f}(t) = \varepsilon(t) \cos \theta \langle \nu^f, J^f | \mu_{g,e} | \nu^i, J^i \rangle . \tag{2.42}$$

In which case, if the field interacts with an ensemble of randomly oriented molecules in the gas phase, then the angle θ between $\boldsymbol{\mu}_e(\mathbf{q})$ for each molecule and the fixed field $\boldsymbol{\varepsilon}(t)$ can be averaged ($\langle \cos^2 \theta \rangle = 1/3$), and we find that the probability of an electronic transition to be given by

$$P_{i,f}(t) = |H_{g,e}^{i,f}(t)|^2 \propto |\varepsilon(t)|^2 |\overline{\mu}_{g,e}^{i,f}|^2 |\langle \nu^f, J^f | \nu^i, J^i \rangle|^2 , \tag{2.43}$$

where first term is proportional to the intensity of the laser field, the second term

provides us with the orbital selection rule, and the last term is known as the *Franck-Condon (FC) factor*. As stated above, the coupling of an individual molecule with the radiative field (Eq. (2.41)) is a function of the angle, $\cos\theta$, between the internuclear axis and $\hat{z}$. Thus every molecule in the ensemble with a different spatial orientation will experience a different overall strength of the electric field, $|\mathcal{E}(t)|$. Fortunately, our procedures are fairly robust to variations in the pulse intensity. Although, it is possible to prepare the sample as a volume of (non-isotropically) aligned molecules using an initial pump pulse [65]. In this way the molecular axes of all the molecules in the ensemble can become oriented parallel to the electric field of the laser before starting an experiment.

Molecular Wavepackets

Under perturbation theory (PT), a monochromatic or narrowband laser field will excite a single eigenstate ν_j from an initial eigenstate ν_i according to Eq. (2.43). However, a broadband Gaussian laser pulse, which in PT can be thought of as a coherent sum of monochromatic light fields with varying wavelengths, can access many different energy levels from a given initial state. It is this coherent property of the laser field that allows for the accurately manipulation of molecular states and the control of quantum processes (see also Sec. (2.3.3) on Coherent Control). By using such a laser excitation we can create a coherent superposition of a set of eigenfunctions (stationary states) known as a molecular wavepacket. Assume that we are only dealing with vibrational states ($\psi_k^{vib}(R)$) in a given electronic surface, we may write the wavepacket as

$$\Psi(R,t) = \sum_k c_k \psi_k^{vib}(R) e^{-iE_k t} \tag{2.44}$$

where c_k are the coefficients or amplitudes of the kth vibrational state with eigenenergy E_k. In first-order PT, these coefficients become [66]

$$c_k = 2\pi i \epsilon(\omega_{k,i}) d_{k,i} \tag{2.45}$$

where $\epsilon(\omega_{k,i})$ is the field strength at the frequency $\omega_{k,i}$, and $d_{k,i}$ is the electronic TDM between the initial and final states. We see from Eq. (2.45) that the initial form of the wavepacket $\Psi(R,t)$ will be determined by the spectral width of the laser field and the strength of the electric dipole couplings. However, because each of

the individual stationary eigenstates evolve in time with a complex phase the initial wavepacket will quickly delocalize. This delocalization or de-phasing of vibrational eigenstates, is due to the interferences between the constituent eigenstates which evolve with different periods. The wavepacket probability density,

$$|\Psi(R,t)|^2 = \sum_{k,k'} c_k c_{k'}^* \psi_k^{vib}(R) \psi_{k'}^{vib}(R)^* \cos(\omega_{k,k'}t) \qquad (2.46)$$

shows that the predominant frequencies in wavepacket motion are the *beat frequencies* ($\omega_{k,k'} = E_k - E_{k'}$) between individual eigenstates. To first order, $\Delta k = \pm 1$, the semi-classical vibrational period of the wavepacket is given as $T_{cp} = 2\pi/\omega_{k,k'}$. Of course all the higher order terms along with the weighting $a_\nu a_{\nu'}$ describing the magnitude of the oscillations are required to fully describe a wavepacket's behavior. Though we can roughly state that a wave packet revivals occur with period $T_r \approx 2T_{cp}/\omega_{k,k'}$, so for example in Na$_2$, we find $\mathrm{T}_{cp} \approx 300$ fs and $\mathrm{T}_r = 29$ ps. In Sec. (2.4.2) we will discuss the future of wavepackets when left untouched, particularly in the context of molecular fluorescence (see Sec. (2.4)).

2.3.3 Quantum Control Schemes

Only upon the invention of coherent fields (lasers) have quantum control schemes been able to accurately specify the interaction and control the final states of molecular systems. In the current subsection we will briefly outline one quantum control scheme which harnesses the complex phases inherent in electric fields and quantum states; this has become known as *coherent control* (CC).

Coherent control [66, 67] of quantum systems is very active area of research in physics and chemistry. The mechanism for control is the interference between multiple pathways from some initial state(s) to some final state(s). The nature of the interference is manipulated by changing the relative complex phase of the laser fields which are exciting the different paths.

For simplicity and for our purposes, we will use weak-fields and can thus understand the process in the context of perturbation theory (PT). In general, CC becomes more difficult in the strong field case once AC Stark shifts arise and the perturbations of the quantum system becomes dynamical.
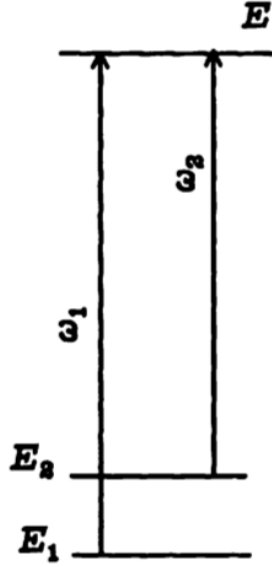
Figure 2.5: Implementation of bichromatic control (BCC) in a three state system where the initial population resides in states E_1 and E_2. Two continuous wave (CW) lasers with frequencies ω_1 and ω_2 respectively, couple these states to a final state E. The amplitude and phase relation between the two laser fields will determine the population of the final state.

Bi-Chromatic Control

One of the simplest implementations of coherent control is a scheme known as Bi-Chromatic Control (BCC) [66], depicted in Fig. (2.5). In this case, there are two ground states which are initially populated, say E_1 and E_2, and we wish to excite a third state, E. Take two CW fields with frequencies ω_1 and ω_2 which independently couple the two initials states to the one final state, then using perturbation theory (or Eq. (2.45)) the amplitude of state E can be written as

$$c_E \propto \epsilon(\omega_1)d_1 + \epsilon(\omega_2)d_2 \qquad (2.47)$$

where the *complex* quantities, $\epsilon(\omega_k)$ and d_k (see Sec. (2.3.2)), can be written in terms of a real-valued amplitude and phase as: $\epsilon(\omega_k) = |\epsilon(\omega_k)|e^{i\delta_k}$ and $d_k = |d_k|e^{i\phi_k}$ where $\phi_k = \{0, \pi\}$ for bound states $\{E_1, E_2, E\}$. With this representation we can write the probability amplitude of the final state as

$$|c_E|^2 \propto |\epsilon(\omega_1)d_1|^2 + |\epsilon(\omega_2)d_2|^2 + 2|\epsilon(\omega_1)||\epsilon(\omega_2)||d_1||d_2|\cos(\Delta\delta_{1,2} + \Delta\phi_{1,2}), \quad (2.48)$$

where $\Delta\delta_{1,2} = \delta_1 - \delta_2$ and $\Delta\phi_{1,2} = \phi_1 - \phi_2$. By varying the relative laser intensities $(\epsilon(\omega_k))$ and phases (δ_k) between the two pathways 1 and 2, such that $|\epsilon(\omega_1)||d_1| = |\epsilon(\omega_2)||d_2|$ and $\Delta\delta_{1,2} + \Delta\phi_{1,2} = \{0, \pi\}$, the final population residing in state E

after the BCC process can be tuned to be anywhere between 0 and $4|\epsilon(\omega_1)||d_1|$. This process is analogous to controlling the appearance of fringes in the well-known double slit experiment, in which two coherent beams interfere either constructively or destructively on a particular target depending on their relative amplitude and phase relations.

Although we have presented the BCC technique using two independent CW laser fields, it is possible to stimulate the two excitation pathways using a single broadband laser pulse [68–70]. By using pulse shaping techniques (Sec. (2.3.2)) to manipulate the magnitude and phase at the two frequencies components of the field (ω_1 and ω_2) corresponding to the transition energies we can apply BCC in the femtosecond regime. In Chapter 5 we will harness this technnique for determining the relative phases of the transition dipole matrix elements between rovibrational eigenstates.

2.4 Molecular Spectroscopy

Here we extend the discussion of the light-matter interactions to include the radiative emissions of diatomic molecules in the gas phase. This emitted fluorescence provides us with information about a molecules internal structure and dynamics, and the ability to verify theoretical ideas and models.

For a single excited rovibrational state, $|i\rangle$, with population $|c_i|^2$, we define the *radiative lifetime* as $\tau_i = 1/\gamma_i$ where γ_i is the *decay rate* and the population after time t is

$$|c_i(t)|^2 = |c_i(t=0)|^2 e^{-\gamma_i t}. \tag{2.49}$$

In the absence of collisions, nonradiative decay processes or stimulated emission, the decay rate is given as

$$\gamma_i = \sum_f A_{f,i} \tag{2.50}$$

where the summation occurs over all (allowed) final states of transition, and $A_{f,i}$ is the Einstein spontaneous emission coefficient. The Einstein A-coefficient is a first-order decay constant defined (in atomic units) as

$$A_{f,i} = \frac{4\omega_{f,i}^3}{3c^3} |\mu_{f,i}|^2, \tag{2.51}$$

where $\omega_{f,i}$ are the transition frequencies and $\mu_{f,i}$ are the transition dipole matrix elements. Therefore, the decay of a state can be quantified by a single exponential

despite the summation over all Einstein coefficients. Note that for rotating molecules a sum over the m_J quantum number is implicit in $|\mu_{f,i}|$, namely,

$$|\mu_{f,i}|^2 = \sum_{m_f=m_i-1}^{m_i+1} |\langle f, m_f \, |\mu| \, i, m_i \rangle| \tag{2.52}$$

Experimentally, the fluorescence or phosphorescence (*e.g.* the decay to a triplet state in the presence of spin-orbit coupling) emitted by molecules can be viewed in either the frequency- or the time-domain. We will briefly discuss these two pictures below, though for a detailed review see Ref. [71].

2.4.1 High-Resolution Rovibrational Spectroscopy

High-resolution molecular spectroscopy is principally used for determinating the internal structure of a molecule, this includes its rotational, vibrational, and electronic energies. In this thesis we will be interested only in the visible or ultraviolet (UV) rovibrational spectrum of, predominantly, diatomic molecules. In Fig. (2.6)(a) we show a pair of Born-Oppenheimer potential energies curves and a few of the eigenenergies associated with each. Population in the excited potential will spontaneously decay through the emission of radiation to the levels of the ground state. A *spectrum*, $I(\omega)$, shown in Fig. (2.6)(b), is a plot of of the signal strength versus frequency, where the signal strength is often based on detection of photons recorded as an electrical current or voltage. The difference magnitudes of the spectral lines across frequencies correspond to the difference strengths of the transition dipole matrix elements (TDMe) coupling excited and ground rovibrational eigenstates. Spectroscopist will almost always write the frequency in units of cm^{-1} (or wavenumbers), however, as a theorist, atomic units (Hartree) will be used interchangeably (1 Ha $= 2.1947 \times 10^5$ cm^{-1}).

There are many approaches that can be used for collecting such frequency-resolved spectra, this thesis will not deal with these practical techniques but will focus on the application of this data. Common methods such as Raman-spectroscopy, Fourier-transform interferometry and CARS spectroscopy, and others can be reviewed in Refs. ([71],[48]).
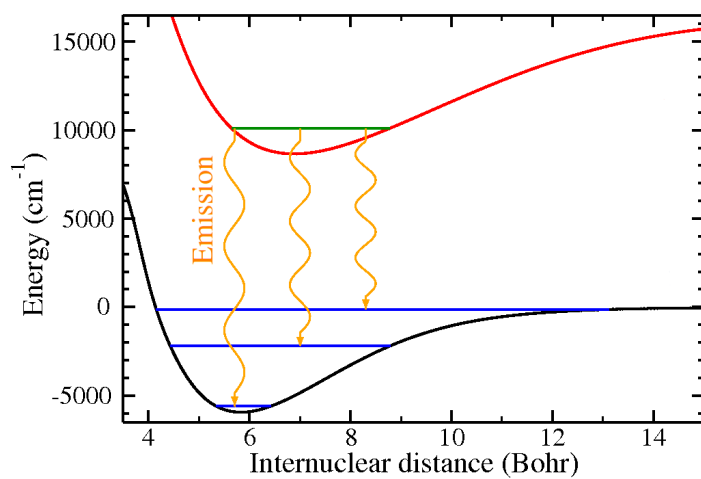
(a)
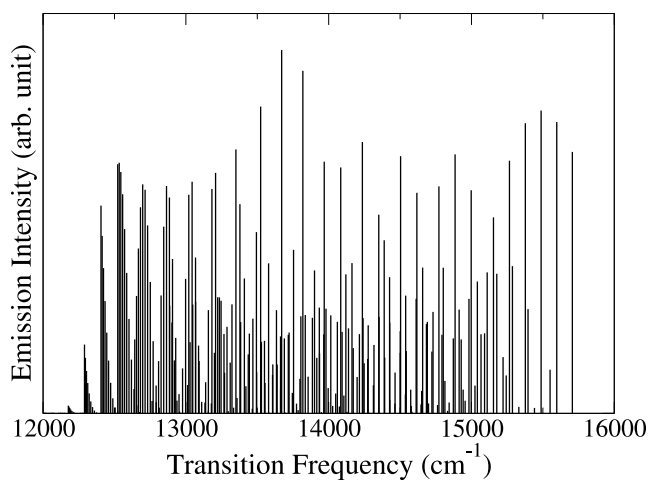
(b)

Figure 2.6: (a) A schematic illustration of the emission process between two diatomic potentials. (b) A typical spectrum of fluorescence lines calculated between the rovibrational states of the two electronic potentials shown in (a).

Laser-Induced Fluorescence and Fourier Transform Spectrometry

In brief, laser-induced fluorescence (LIF) involves exciting a state or states of a quantum system with an electromagnetic field, such that it will undergo spontaneous de-excitation (or fluorescence), emitting radiation which can be then captured. LIF is widely used in the spectroscopy of diatomic molecules since the lasing wavelength can be tuned to a particular excitation, which allows for the determination of intensities associated with a particular vibrational or rotation level. This method is applicable to very weak transitions with Franck-Condon factors below 10^{-4}, and capable of resolving high values of vibrational and rotational quantum numbers. Advantages over absorption spectroscopy are the very high signal-to-noise ratios and the ability to capture radiation in all directions since the fluorescence signal is often isotropic. Note that, as a result of the low excitation energies, stimulated emission processes are typically ignored in the data analysis due to their negligible contribution to the fluorescence.

To characterize the spectrum of the fluorescence radiation, the simplest approach would be to use a monochromator and measure the intensity of the light at all the relevant wavelengths. However, the full spectrum can be generated much more efficiently, and with less sensitivity to noise, using a technique known as Fourier transform spectroscopy (FTS) [72]. FTS is based on the principles of interferometry, in which coherent waves from at least two sources or paths are combined and their superposition measured. In particular, a Fourier transform spectrometer is designed similar to a Michelson interferometer, except that one of the mirrors can move rapidly back and forth, and the recombined beam is detected synchronously with the motion of this mirror. This allows for the temporal correlation function of the light to be measured at each different time delay, thus converting the time domain into a spatial coordinate. The measured outcome, known as an interferogram, is an intensity measurement as a function of the retardation path length. The interferogram recorded by the detector can be thought of as a sum over weighted monochromatic interferograms, in which we think of each spectral component of the radiation as producing its own interferogram with an amplitude weighted by the relative spectral intensity. From this perspective, we can see that by making measurements of the signal at many discrete mirror positions, we can use a Fourier transform to pick out the intensities of each frequency and produce a spectrum. Or, in other words, the interferogram (intensity of recombined beam as a function of path length) is

simply the Fourier transform of the intensity of the light source. In practice, this technique has become very reliable and can provide very high resolution (~ 0.005 cm^{-1}) [16, 73].

Phase of TDMe

Before continuing on we will comment on the phases of the TDMe; particularly, since the spectral data only provides information about their magnitudes. These matrix elements are linked to the potentials and the nuclear wave functions that are derived from them. In bound-bound transitions, both initial and final eigenstates in $\langle \nu'' | \mu | \nu' \rangle$ are real, thus this becomes a simple sign ($\pm$), unlike the usual complex phase encountered in scattering theory. When dealing with transition between n excited states and m ground states there will exist $n \times m$ TDMe and thus seemingly 2^{nm} sign possibilities. However, because each individual wavefunction $| \nu \rangle$ can have an arbitrary phase, we are free to choose the signs of $n + m - 1$ TDMe at will. For example, all m TDMe of sgn($\langle \nu'' | \mu | \nu' = 0 \rangle$) for $\nu'' = \{0, m-1\}$ can be chosen to be positive, where *sgn* is the sign function. This fixes the arbitrary phases of the final $| \nu'' \rangle$ states and the one initial $| \nu' = 0 \rangle$ state. With these states fixed, we can now choose sgn($\langle \nu'' | \boldsymbol{\mu} | \nu' \rangle$) for all other $\nu' = \{1, n - 1\}$ by selecting any overall phase for each $| \nu' \rangle$. This gives us the $n + m - 1$ arbitrary chosen phases of the TDMe, and the rest of the $(n - 1) \times (m - 1) + 1$ are then fixed and need to be determined by performing the integration over the relevant wave function or extracted from the experimental data (Chapter 3).

A basic argument towards obtaining the relative phase (sign) information involves using a semi-classical stationary phase point approximation. Namely, it states that whenever the observed transition intensities along a fluorescence progression (same ν', series of ν'') depart from monotonic behavior, the phase of the transition amplitude has reversed. It is true that the fluorescence progression shows a trend and the nodal structures reveals the wavefunction of the ν' state. However, the fixing of phases of the transition dipole amplitudes is strictly tied to the fixing the relative phases of wavefunctions of ν'' states. Let us take the simplest case: $\nu' = 0$ vibrational state. If one expands $| \nu' = 0 >$ in terms of the $| \nu'' >$ states, the formula will be: $\phi(\nu' = 0) = \sum_{\nu''} | \nu'' >< \nu'' | \nu' = 0 >$. The second term is the Frank-Condon overlap while the first $| \nu'' >$ is the basis wavefunction for the expansion. We know the fluorescence spectrum, $| < \nu'' | \nu' = 0 > |^2$, shows no nodal structures. Therefore, one can *choose* to assign $< \nu'' | \nu' = 0 >$ to be all positive. However, this choosing

signs fixes the relative phases of $|\nu''>$ simultaneously. Therefore, one then needs to be able to *use/find* these relative phases of $|\nu''>$ as well, instead of blindly assigning them inconsistently. Equivalently speaking, after choosing $<\nu''|\nu'=0>$ to be all positive (or all negative), there is no freedom to choose the signs for each $|\nu''>$ except for an overall sign, while the relative signs are fixed! It is, in general, very difficult to search for the correct combination of relative signs for the basis wavefunction: it is a 2^{N_g-1} problem where N_g is the number of basis functions for even just one ν' state (not 2^{N_g} because of the arbitrary overall sign). Furthermore, the choice of using the simple semi-classical wavefunction as the basis wavefunction does not give all positive/all negative signs for $<\nu''|\nu'=0>$, which confirms the fact that the solution for these relative signs are non-trivial.

Also, we need to point out that for diatomics these semi-classical methods are at best approximate. In fact, as is well known in semi-classical theories, the single stationary phase approximation often fails, especially in the long wavelength regime or when the main contributions to the dipole matrix elements come from the vicinity of the classical turning points. For any procedure to be useful it has to be completely general and highly reliable. The fact there are some cases in which a simple argument based on a single stationary phase approximation might work is not sufficient for a general procedure. So although fluorescence progression 'might' indicate sign reversal, this is certainly not the case when double minima exist, or in polyatomic case. In particular, two or more phase reversals (nodes) can occur in the region between the ν',ν'' and $\nu',\nu''+1$ transition, for example when the nodes are closely spaced (due to high kinetic energy) or when the transition amplitudes are small.

As will be seen in Chapter 3, determination of these relative phases can be done accurately and efficiently because, instead of searching for various combinations of relative signs of basis wavefunctions, knowledge of the energy levels of the excited states can be used to "guess" smartly what the signs of $<\nu''|\nu'=0>$ are when the relative signs of the basis wavefunctions, $|\nu''>$, are pre-chosen. This is possible because interference effects are experimentally observable; hence the correct sign of an interference effect can be obtained from a computation that embodies internal consistency.

In Chapter 5, we present another approach which directly extracts the complex amplitudes (magnitudes and phases) of transition dipole matrix elements. The method uses Bi-chromatic Coherent Control (BCC) in conjunction with time-resolved fluorescence to uniquely determine the transition properties between individual rovi-

brational eigenstates without any a priori assumptions. See Sec. (3.1) for other alternative approaches that use spectral information for uncovering the structure and properties of a molecule.

2.4.2 Time-Resolved Fluorescence of Vibrational States

High-resolution measurements for gases using time-resolved picosecond Raman spectroscopy were first demonstrated by Graener et al. in 1984 [74]. Modern approaches (see Ref. [71]) now include using femtosecond Four-wave Mixing Spectroscopy together with optical gating [75] and up-conversion [4, 5] techniques to achieve temporal resolution of less than 60 fs. In Fig. (2.7)(a) we show an excited wavepacket

(a)	(b)
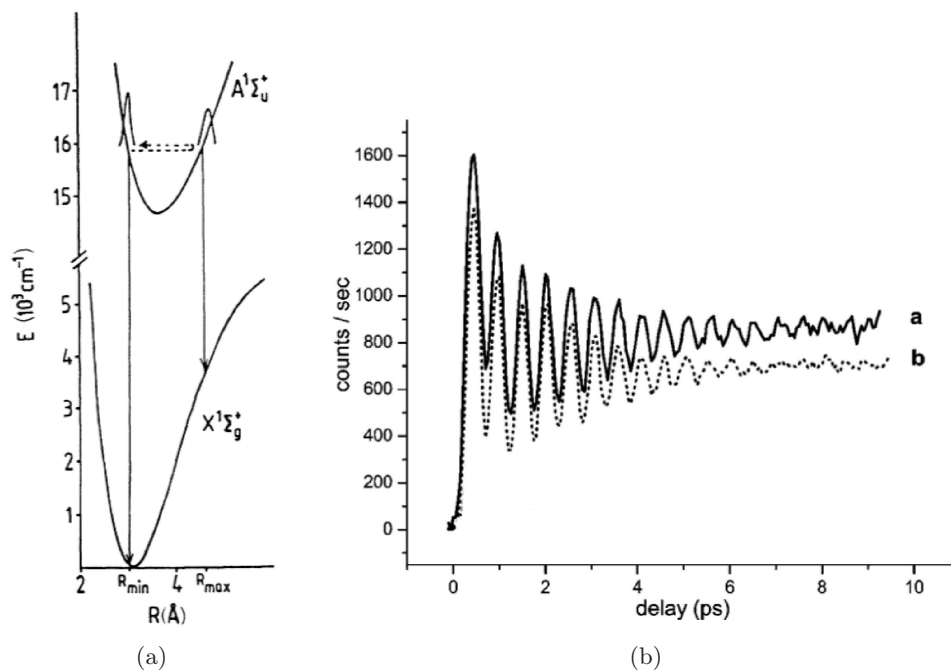
Figure 2.7: (a) Wavepacket decaying from an excited PES to the ground state. The most probable decay routes are shown for when the wavepacket is at its turning points. Image taken from Ref. [4]. (b) Temporal fluorescence captured over several picoseconds. This picture is taken from Ref. [5] where the number of counts are captured after the upconversion of the raw fluorescence. The two lines capture the results without (a) and with (b) a monochromator inserted after the crystal.

at the two end points of its oscillations in the excited PES. The two vertical lines depict the most probable decay path for when the wavepacket is in these positions,

namely, when the wavepacket has the greatest overlap (Franck-Condon factor) with a vibrational state in the ground potential. Although the typical lifetimes of vibrational states for diatomics, which can be calculated using Eq. (2.50), are in the nanoseconds (ns), the probabilistic behavior of the spontaneous fluorescence process means that a measurable fraction ($\sim 10^{-8}$) of the excited molecules in a gas (of say 10^{23} particles) will decay after a few femtoseconds (fs). Unfortunately, the fastest electronics operate on a picosecond timescale, and thus capturing time-dependent processes at any shorter times requires the application of alternative techniques; one such approach is *up-conversion*.

Up-Conversion

This method focuses the spontaneous fluorescence captured over a fixed solid angle (say, 0.03sr) onto a nonlinear crystal [4]. A gate-pulse (or pulse-train) is also sent into the crystal such that whenever the radiation temporally and spatially overlaps it leads to sum-frequency generation. The resulting radiation (often in the ultraviolet (UV)) is sent through a double-prism monochromator and measured using a photomultiplier [5]. For single gate-pulses, the time dependence of fluorescence occurs by varying the timing of the gate pulse relative to the pulse causing the initial excitation (in a similar manner to pump-probe absorption measurements).

In a mathematical sense we define time-dependent spectrum in terms of the energy spectrum ($S(T, \omega_F)$) over finite-time and frequency. Following Walmsley in Refs. ([5],[4]):

$$S(T, \omega_F) = \int_{-\infty}^{\infty} dt |E_{FB}(t)|^2 \tag{2.53}$$

where the electric field is given as

$$E_{FB}(t) = \int_{-\infty}^{t} dt' H(t - t', \omega_F) B(t', T) E(t') . \tag{2.54}$$

The gate-pulse acts as the time gate such that

$$B(t, T) = e^{(-|t-T|\Gamma)} \tag{2.55}$$

where Γ relates to the pulse duration, while the double monochromotor acts as a

frequency filter and can be modeled by

$$H(t - t', \omega_F) = \gamma^2 [\gamma^2 + (\omega - \omega_F)^2]^{-1} . \tag{2.56}$$

In this way, temporal resolutions of at least 60 fs with energy ranges of 4 nm can be attained.

2.4.3 Bound-Continuum Transition

The discussion of molecular state emissions has so far only included bound-bound transitions. However, as an excited bound state decays, there will also be a weak coupling to lower continuum states. The dipole matrix elements associated with these transitions are complex due to the nature of the continuum states. We demonstrate in Sec. (2.1.2) how to represent these continuum states as pseudo-bound states and calculate an effective real-valued TDMe. To be sure of the accuracy of this approximation, the effective eigenstates and TDMe representing the continuum space must be compared with the results of a proper calculation. One method to obtain these complex TDMe involving continuum levels is known as the *artificial channel method*.

Artificial Channel Method

The quality we are interested in determining is the matrix element

$$f_{\boldsymbol{m},i} = \langle E, \boldsymbol{m}^- | \mu_e | E_i \rangle \tag{2.57}$$

where $| E_i \rangle$ is the initial bound excited state, $| E, \boldsymbol{m}^- \rangle$ represents an incoming $(^-)$ scattering states with energy E and collective quantum number $\boldsymbol{m}$, and μ_e is the usual electric dipole function [51–53]. Note that we do not use the outgoing scattering states because they correspond at early times to a well-defined fragment state $| E, \boldsymbol{n}^0 \rangle$ and not a molecular bound state $| E_i \rangle$ as in our case. On the other-hand, the incoming solutions, $| E,^- \rangle e^{-iEt}$, approach in the infinite future a single well-defined asymptotic state $| E, \boldsymbol{n}^0 \rangle$. The $f_{\boldsymbol{m},i}$ integral, which is often described as a *photodissociation amplitude*, is difficult to calculate due to the highly oscillatory scattering function $\langle R | E, \boldsymbol{m}^- \rangle$.

Shapiro [51] developed an approach to calculate $f_{\boldsymbol{m},i}$ by treating the problem using time-independent scattering theory with a source term, namely, $| E_i \rangle$. However,

instead of solving a set of inhomogeneous differential equations (DEs) (with source term), he re-expressed these as a set of coupled homogeneous DEs. This allows for greater generality of the solution in regards to different ground state PESs, but leads to a great difficulty in integrating over the bound wavefunction for all energies, because its solutions diverge asymptotically at all energies other than at the particular eigenenergies. This problem can be stabilized by including one extra "artificial" continuum channel which serves as a source for the bound manifold. The final solutions to $f_{m,i}$ using the artificial channel method (ACM) can be found in Ref. [52], therein also contains several alternative approaches so such calculations. For our application in Sec. (2.1.2) we use a FORTRAN subroutine written by M. Shapiro in 1972, entitled: "Program for Quantum Mechanical Solutions of Photo(Pre)dissociation and Bound State Problems, using the Artificial Channel Method".

Chapter 3

Inverions of Potential Energy Surfaces

3.1 Potential Inversion Methods

The Born-Oppenheimer approximation gives rise to the concept of molecular potential energy surfaces/curves (PES) which then governs a molecule's behaviors and interactions. However, even for large-scale *ab initio* calculation on small molecular systems, these electronic eigenvalues are difficult to obtain within spectroscopic accuracy [76, 77]. Therefore, it is necessary to determine these potentials (or PES) empirically from experimental observations. In this section we outline several currently existing methods of extracting the PES from spectroscopic data, and mention the drawbacks associated with each.

3.1.1 Dunham Expansion

Nearly all approaches that determine an electronic PES from experimental data use knowledge of the rovibrational energies of the desired potential. These eigenenergies can be obtained directly by analyzing the transitions appearing in a given spectrum. By taking the differences of spectral lines relating a common state $(\omega_{i+1,j} - \omega_{i,j} = \omega_{i+1,i} = \Delta E_{i+1,i})$ and the combination of differences between two such results $\Delta(\Delta E_{k,i}) = \Delta E_{k+1,k} - \Delta E_{i+1,i}$, we can use a least-squares approach to find the spectroscopic constants $\{\omega_e, \omega_e x_e, B_\nu, D_\nu, ...\}$ used in the expansion of the rovibrational energies (Eq. (2.16) from Sec. (2.1.2)). Given these constants it is then possible to obtain an expression for an ordinary single minimum PES.

In the simplest case, we found in Sec. (2.1.2) that these constants can be related to those of a Morse function (Eq. (2.18)). In particular, the eigenvalues of the

vibrational states for a rotationless Morse potential are given by

$$
\begin{aligned}
E_\nu &= \omega_e(\nu + 1/2) - \omega_e x_e(\nu + 1/2)^2 & (3.1) \\
&= \beta\sqrt{\frac{2D_e}{\mu}}(\nu + 1/2) - 2\mu\beta^2(\nu + 1/2)^2 \ , & (3.2)
\end{aligned}
$$

where β and D_e are two of the Morse parameters. This form of the PES is usually not sufficient for realistic applications, however, it serves very-well in providing a rudimentary model of the PESs in a diatomic for testing purposes.

Often, a better expression can be obtained using the work of Dunham [78]. He provided an expression for the rovibrational energies in terms of spectroscopic constants

$$
E(\nu, J) = \sum_{i,j} Y_{i,j}(\nu + \frac{1}{2})^i[J(J+1)]^j \ , \tag{3.3}
$$

where the *Dunham coefficients*, $Y_{i,j}$, are given by *e.g.* $Y_{1,0} \approx \omega_e$, $Y_{2,0} \approx -\omega_e\chi_e$, $Y_{0,1} \approx B_e$, $Y_{0,2} \approx -D_e$, etc. In his treatment, Dunham modeled a diatomic as a vibrating rotor in which the electronic PES, $U(x)$, is given as a Taylor series expansion about the minimum, R_e, where $x = (R - R_e)/R_e$,

$$
U(x) = a_0 x^2 (1 + \sum_{i \geq 1} a_i x^i) \ , \tag{3.4}
$$

and the $\{a_i\}$ potential parameters can also be related to the Dunham coefficients (*e.g.* $a_0 = -Y_{1,0}^2/(4Y_{0,1})$, $a_1 = Y_{1,1}Y_{1,0}/(6Y_{0,1}^2)$,...). In the same way as earlier, these Dunham coefficients can be determined directly from a global fit of the experimentally assigned spectral lines to the analytical energy levels using a least-squares fitting routine. The solution Dunham provided is found using the first-order WKB (Wentzel-Kramers-Brillouin) approximation, thus the model suffers for light molecules and at long-ranges where the potential function diverges. Many groups have provided corrections using higher-order WKB and Born-Oppenheimer breakdown terms involving adiabatic and non-adiabatic effects [79, 80]. However, in the end this approach cannot make prediction beyond the range of the available data [81], and is complicated by the multitude of corrections necessary for reasonable results and the strong inter-parameter correlation in the Dunham expansion.

3.1.2 Rydberg-Klein-Rees (RKR) Method

Given knowledge of the vibrational, $G(\nu)$, and rotational, B_e, constants obtained from fitting to spectral lines there is an another approach known as the Rydberg-Klein-Rees (RKR) method [82–85] for determining PESs. Similar to Dunham's approach, but with the advantage that one is not fitting a given functional form (Eq. (3.4)), this method also applies the first-order WKB (Wentzel-Kramers-Brillouin) approximation in the form of the quantization condition

$$\int_{R_-}^{R_+} p\,dR = \pi(\nu + 1/2) \tag{3.5}$$

where $p = 2\mu\sqrt{E - V(r)}$ is the momentum and R_- and R_+ are the classical inner and outer turning points of the nuclear motion. However, instead of starting with a model and finding some expression for $V(r)$, the RKR method relies on a clever trick which avoids creating any definition for the potential. This requires the definition of a special function $A(E, J)$ with partial derivatives, $\partial/\partial E$ and $\partial/\partial J$ that can be expressed as both a function of the two turning points, R_+ and R_-, and as an integral over the vibrational quantum number, ν, where the integrand depends only on the spectroscopic functions $G(\nu)$ and B_ν [86].

$$R_\pm(\nu) = \left(f(\nu)^2 + \frac{f(\nu)}{g(\nu)}\right)^2 \pm f(\nu) \tag{3.6}$$

where

$$
\begin{aligned}
f(\nu) &= \sqrt{\frac{1}{2\mu}} \int_{-\frac{1}{2}}^{\nu} |G(\nu) - G(\nu')|^{-\frac{1}{2}} d\nu' \\
g(\nu) &= \sqrt{2\mu} \int_{-\frac{1}{2}}^{\nu} B_{\nu'} |G(\nu) - G(\nu')|^{-\frac{1}{2}} d\nu' \ .
\end{aligned} \tag{3.7}
$$

Note that corrections to the rotational parameter B_e to account for rotational-vibrational interactions are given by the rotational function,

$$B_\nu = B_e + \sum_{i=1}^{\infty} (-1)^i \alpha_e (\nu + 1/2)^i \tag{3.8}$$

where α_e are higher order constants.

Although the RKR method lacks self-consistency in the vibrational and rotational

constants, researcher, such as Tellinghuisen [45, 46], have developed iterative schemes to converge the results. And, standard programs such as LeRoy's `RKR1` [87] now exist to construct RKR curves from spectral data. The procedure uses the initial estimation of the $G(\nu)$ and B_ν harmonic constants to calculation $V(R)$ using the RKR method. The RKR potential, $V(r)$, is then used to calculate the centrifugal distortion (spectroscopic) constants D_e and H_e which are then used as corrections to the measured (raw frequencies) wavenumbers. With these adjusted wavenumbers, we iteratively return and obtain a least-squares estimation of the two harmonic terms to generate a new potential. This technique and many other methods [88–91] refine and expand the use of the RKR approach, however, several drawbacks appear to be inherent within its application. Namely, that its validity is generally restricted to only when the BOA is valid, and its foundation in the WKB approximation limits its accuracy for very light dimers. And similar to Dunham, the potentials can only be constructed up to highest observed vibrational state, so it becomes unreliable at energies near and above the dissociation limit (*e.g.* it cannot resolve the repulsive barrier). Lastly, RKR cannot address exotic potentials with multiple minima and struggles with multidimensional (polyatomic) systems.

3.1.3 Direct-Potential Fits

The most common approach for obtaining accurate PESs in diatomic molecules in recent years [92–97] is through using direct potential fits (DPFs).

Inverted Perturbation Approach

The modern DPF technique is based on the original inverted perturbation approach (IPA) of Kosman and Hinze [98], which is a fully quantum mechanical method (contrary to the semiclassical Dunham or RKR schemes) for defining diatomic PESs. The method seeks to find a linear correction $\delta U(R)$ to some initial approximation of the potential curve $U(R)$ such that the eigenvalues of the molecular Schrödinger equation with a potential term $U(R) + \delta U(R)$ best agree with the measured spectra. Using a parametrized function for $\delta U(R)$, the numerically solutions of the Schrödinger equations can be designed to converge, in the least-squares sense, to the experimental eigenvalues. Initially [98], a series of global Legendre polynomials were used to describe $\delta U(R)$, however, it was later found [99] that IPA gave more realistic results when the potential energy correction term was expanded in terms of local

distributed Gaussian functions. These local functions were evaluated directly on a set of discrete variable representation (DVR) points and the least-square fitting to the spectroscopic data of eigenenergies was done using singular value decomposition (SVD). However, because the success of IPA depends strongly on the choice of basis functions, it is difficult to guess which expansion will fit the correction better and with less coefficients; particularly when the the real shape $V(R)$ is quite exotic.

To avoid this functional dependence, Pashov [100] proposed a modified-IPA approach which expressed the correction to the potential curve as a set of n equidistant points and then afterwards connected these points with a spline function. Other authors [101–103] have extended this program, however more recently, the preferred approach has been to use direct fits to determine parameters characterizing the potential energy functions.

DPF Analysis

The more general DPF analysis allows one to create model Hamiltonians of molecular systems that also take into account atomic-mass-dependent radial and centrifugal potential corrections due to the breakdown of the BOA. The unknown functions for the PES, spin-orbit couplings or non-adiabatic corrections are parametrized using some initial estimates. Similar to IPA, the theoretical eigenenergies from a numerical solution of the radial Schrödinger equation are compared with the experimental spectral lines, and the error between these transition energies are minimized by iteratively optimizing the values of the parameters in the unknown functions. Researchers such as Coxon [104, 105], Bergeman [19, 93, 95, 96, 106] and LeRoy [80] have been very active in applying this approach. In particular, LeRoy [107] has developed and provided free publicly available computer programs (`DPotFit` [108]) for implementing such routines.

However, because IPA is based on the first-order perturbation approach to iteratively correct the potential energy and DPF involves minimizing a multi-dimensional nonlinear system, it becomes essential to have a good prior knowledge of the potential surface. Without starting with very good initial estimations neither method will converge to the experimental data; often because, the system of linear equations is usually overdetermined and it becomes difficult to find the global minimum. Unfortunately, such prior estimates are not always available, particularly for the cases of double minimum potentials, and thus a lot of variables must be included in the parametrization; greatly increasing the computational costs.

Model Potentials

Model potentials are often used when given a set of conventional spectroscopic constants or when fitting spectral lines from, say, FT-spectroscopy measurements [32, 73, 109]. As mentioned earlier, to represent ordinary single minimum PES, the simplest option is the Morse function whose vibrational eigenvalues can be related to the spectroscopic constants

$$E_\nu \; = \; \omega_e(\nu + 1/2) - \omega_e x_e(\nu + 1/2)^2 \qquad (3.9)$$

$$= \; \beta\sqrt{\frac{2D_e}{\mu}}(\nu + 1/2) - 2\mu\beta^2(\nu + 1/2)^2 \; . \qquad (3.10)$$

These analytical energies can be used to fit the molecular spectra to find the optimum coefficients, and thus give a Morse representation of the potential.

Other multi-parameter functions such as the Lennard-Jones, Generalized Morse, or Morse-Lennard-Jones [110] provide more flexibility in their application, particular for non-linear direct potential fitting [78, 80, 105, 111], however in the past several years the Morse/long-range (MLR) model, first introduced by LeRoy [81], has proved very successful in representing PESs of diatomic and polyatomic molecules (see Ref. [112] and references therein). The MLR potential is a single analytical function that accurately describes both the deep-well region and long distance behavior of molecular PESs. Fitting experimental data to a single function avoids the problems associated with interpolation and yields reasonable results even with vacancies in the spectra, see the work of Madison [112] for a recent application.

Tiemann [113] also provides another expression, known as the "Hannover" form, which has been used a lot in the DPF papers of Bergeman [19, 93, 95, 96, 106]. Their form will be used in subsequent Chapters as a theoretical model of our PESs.

3.1.4 Reflection Method

None of the above potential inversion techniques provide reliable information about the repulsive wall at and above the dissociation energy. In an attempt to characterize this centrifugal barrier comes the *reflection method*, which is an approximate procedure related to photodissociation dynamics, namely the "photofragmentation mapping" [114]. This approach, also known as collision-induced dissociation (CID) [115, 116], relies on collecting the kinetic energy distribution to determine repulsive wall of a potential. However, theoretically the approach relies on semi-classical

assumptions and fitting restrictions; and experimentally the research has been limited to the study of ions due to the need of large molecular currents for good CID measurements [116].

3.2 A New Approach

Given the ever increasing pool of high-quality spectroscopic and scattering data, our understanding of intra- and inter-molecular dynamics is slowly becoming more and more detailed. The main missing element appears to be the lack of systematic methods for obtaining accurate potential energy surfaces and dipole moment surfaces (DMS) from such data. Though *ab initio* computational methods and more approximate methods which are suitable for larger systems [35–38, 117–119] are quite successful, in most cases the line positions predicted by such computations are not yet of "spectroscopic accuracy". Present day analysis of spectroscopic data are invariably performed in the "forward direction", using analytic functional forms to represent the PES, and optimizing their parameters to replicate to the extent possible the experimental values. Such parameter fitting methods are, however, inherently deficient due to our rather arbitrary choice of the functional forms used and the limited number of parameters we can consider. As we saw the RKR method [82–85] is a direct inversion approach available for diatomic molecules, but it can only generate potentials below the dissociation energy and is limited by the range of validity of the WKB approximation. Moreover, potentials possessing two or more minima cannot be inverted by this method. A few modified RKR methods have been developed for polyatomic molecules [88–91], but these methods are approximate as they are based on the adiabatic separation of the molecular coordinates and the vibrational self-consistent-field (SCF) approximations. Overcoming some of the restrictuions of the RKR method are the fitting approaches such as inverse perturbation analysis [98, 99, 120], IPA for bound-continuum [101], DPF [19, 93, 95, 96, 106], and others [102, 103], but these methods usually rely on having a good prior knowledge of the potential surface, which may not always be available. Other authors [121–123] have developed procedures which determine the PES numerically using Tikhonov regularization. Though, this requires substantial number of iterations and computer resources to deal with slow convergence, the method is under-determined due to the small number of data points used relative to the large number of unknowns, resulting in multiple solutions and non-unique PES. As in other inversion schemes

(e.g. that of scattering cross sections data[50, 124]) the stumbling block appears to be the extraction of the relative *phases* of the relevant (e.g. fluorescence, photo-absorption) amplitudes. Given these phases, it was previously shown [125, 126] that a point-by-point extraction of the excited state PES is possible.

The inversion procedure presented herein, based upon the work of Shapiro [126], avoids using SCF or WKB approximations and is theoretically applicable to poly-atomic systems [6]. The non uniqueness of the associated inverse problem is solved by introducing *a priori* restrictions on the form of the PES using experimental information. The method as developed so far suffers however from the need to first solve the *phase problem*, namely to determine the relative phases of the transition-dipole amplitudes from the (absolute-value) squares of these amplitudes provided by experiments.

In the following we show how the extraction of the phases (for bound-bound transitions - the signs) of transition-dipole amplitudes from their experimentally-measured absolute-value-squares, can be done in an iterative manner. Concurrent with the iterative phase extraction we generate, in an ever increasing range, the excited state potential(s) from which emission occurs. We demonstrate this procedure for several excited states of the Na_2 molecule. We are able to extract the potential(s) below *and* above the dissociation threshold with accuracies that are percentage-wise substantially better than, though proportional to, the accuracy of the experimental data. Our results for the repulsive regions are obtained with greater accuracy and are beyond the assumptions and fitting restrictions inherent of procedures based upon the reflection method [115, 116].

As a by-product, we also generate the transition-dipole function and go beyond the Franck Condon (FC) approximation[47]. We see no inherent restrictions, given data of sufficient quality and completeness, in successfully applying this method to any polyatomic molecule.

3.2.1 Potential Inversion

Our aim is to compute a "target" potential $V_e(\mathbf{R})$, assuming that we already know the (reference) potential $V_g(\mathbf{R})$ to which emission occurs, where $\mathbf{R} \equiv (R_1, R_2, \cdots, R_N)$ designates a collection of the internuclear coordinates of the (polyatomic) molecule of interest.

The time-independent Schrödinger equations associated with the two Born Op-

penheimer potentials are,

$$\left[\hat{K}(\mathbf{R}) + V_g(\mathbf{R}) - E_i\right] \chi_i(\mathbf{R}) = 0 \tag{3.11}$$

and

$$\left[\hat{K}(\mathbf{R}) + V_e(\mathbf{R}) - E_s\right] \phi_s(\mathbf{R}) = 0, \tag{3.12}$$

where $\hat{K}(\mathbf{R})$ denotes the kinetic energy operator for the nuclear coordinates $\mathbf{R}$, χ_i and ϕ_s are, respectively, the bound (rovibrational) wave functions of the ground and excited electronic states. E_i and E_s are the energies of these rovibrational states.

We begin by assuming that we already know the transition-dipole amplitudes,

$$d_{i,s} \equiv \int d\mathbf{R}\chi_i^*(\mathbf{R})\mu_{e,g}(\mathbf{R})\phi_s(\mathbf{R}) \approx \overline{\mu} \int d\mathbf{R}\chi_i^*(\mathbf{R})\phi_s(\mathbf{R}), \tag{3.13}$$

where the last equation spells out the FC approximation [47]. We now rewrite Eq. (3.12) as

$$\phi_s(\mathbf{R})V_e(\mathbf{R}) = [E_s - \hat{K}(\mathbf{R})]\phi_s(\mathbf{R}), \tag{3.14}$$

and multiply both sides from the left by ϕ_s^*. Summing over all discrete states s, and dividing by $\sum_s |\phi_s|^2$, we obtain that

$$V_e(\mathbf{R}) = \frac{1}{\sum_s |\phi_s(\mathbf{R})|^2} \sum_s \phi_s^*(\mathbf{R}) \left[E_s - \hat{K}(\mathbf{R})\right] \phi_s(\mathbf{R}). \tag{3.15}$$

The unknown excited states $\phi_s(\mathbf{R})$ are now expanded in the basis set of ground rovibrational wave functions $\chi_i(\mathbf{R})$,

$$\phi_s(\mathbf{R}) = \sum_i \chi_i(\mathbf{R})\langle\chi_i \mid \phi_s\rangle, \tag{3.16}$$

By employing the FC approximation we can write the $\langle\chi_i|\phi_s\rangle$ overlaps in terms of the transition-dipole matrix elements,

$$\langle\chi_i|\phi_s\rangle = \frac{1}{\overline{\mu}}\langle\chi_i|\mu_{e,g}(\mathbf{R})|\phi_s\rangle = \frac{d_{i,s}}{\overline{\mu}}. \tag{3.17}$$

After replacing $\langle\chi_i|\phi_s\rangle$ of Eq. (3.15) with $d_{i,s}/\overline{\mu}$ and using Eq. (3.16), we obtain

that,

$$V_e(\mathbf{R}) = \frac{1}{\sum_s |\sum_i \chi_i(\mathbf{R})d_{i,s}|^2} \sum_s (\sum_i \chi_i d_{i,s})^* \left[E_s - \hat{K}(\mathbf{R})\right] (\sum_j \chi_j d_{j,s}). \quad (3.18)$$

Use of Eq. (3.11) allows to express the action of the $\hat{K}(\mathbf{R})$ operator on the ground state wave function $\chi_i(\mathbf{R})$ as,

$$\hat{K}(\mathbf{R})\chi_j(\mathbf{R}) = [E_j - V_g(\mathbf{R})]\chi_j(\mathbf{R}). \quad (3.19)$$

Insertion into Eq. 3.18 yields,

$$V_e(\mathbf{R}) = \frac{1}{\sum_s |\sum_i \chi_i(\mathbf{R})d_{i,s}|^2} \sum_s \sum_{i,j} (\chi_i d_{i,s})^* [\omega_{i,s} + V_g] (\chi_j d_{j,s}), \quad (3.20)$$

where $\omega_{i,s} \equiv E_s - E_j$ are the transition energies. Finally, by pulling $V_g(\mathbf{R})$ out of the double summation, we arrive at the expression

$$V_e(\mathbf{R}) = \frac{\sum_s \sum_{i,j} d_{i,s}^* d_{j,s} \omega_{i,s} \chi_i^*(\mathbf{R}) \chi_j(\mathbf{R})}{\sum_s |\sum_i \chi_i(\mathbf{R})d_{i,s}|^2} + V_g(\mathbf{R}). \quad (3.21)$$

Irrespective of any experimental source of error, discussed in section 3.3.3 below, this formula is expected to be accurate only for $\mathbf{R}$ values for which the expansion of $\phi_s(\mathbf{R})$ according to Eq. (3.16) converges well. An additional source of error occurs when the numerator and denominator of Eq. (3.21) approach zero in the far tail of the classically forbidden region. This point is discussed further below.

3.2.2 Transition-Dipole Function

The $V_e(R)$ potentials extracted as described above, enable us to obtain the electronic transition dipole function $\mu_{e,g}(R)$. Starting from the definition of the transition dipole matrix elements (Eq. (3.13)), we multiply both sides by $\chi_i^*(R)$ and perform a summation over the index i. Assuming that the set of ground states $\{\chi_i\}$ forms a complete basis in which we can expand ϕ_s, we apply the completeness condition

$$\sum_i \chi_i(R)\chi_i^*(R') = \delta(R - R'), \quad (3.22)$$

and obtain that

$$\sum_i \chi_i(R) d_{i,s} = \mu_{e,g}(R) \phi_s(R). \tag{3.23}$$

Using the redundancy of Eq. (3.23) with respect to the choice of ϕ_s, we multiply it by $\phi_s^*(R)$ on both sides and sum over the index s. Upon rearrangement, our formula for the dipole function becomes

$$\mu_{e,g}(R) = \frac{\sum_{i,s} \phi_s^*(R) \chi_i(R) d_{i,s}}{\sum_s |\phi_s(R)|^2}. \tag{3.24}$$

The s summation in Eq. (3.24) guarantees (as in Eq. (3.21)) that the denominator does not vanish at the zeroes of any of the wave functions.

As in the potential extraction, the accuracy in calculating the dipole function at a given position $\mathbf{R}$ depends on the completeness of the eigenstates of our reference potential in that region and having non-vanishing excited states $\phi_s(\mathbf{R})$ amplitudes.

3.2.3 Going Beyond the FC Approximation

In deriving Eq. (3.21) we have invoked the FC approximation[125, 126], having replaced the overlap matrix elements $f_{is} \equiv \langle \chi_i \mid \phi_s \rangle$ that should have been used in Eq. (3.21), by $d_{is}/\overline{\mu}_{e,g}$. (The unknown constant $\overline{\mu}_{e,g}$ is unimportant because it cancels out in both the denominator and numerator.) We had to make this replacement because prior to the extraction of V_{ex} all we had were the, experimentally derived, $|d_{is}|$ matrix elements. Having completed the above iteration procedure obtaining a good representation of $V_{ex}(R)$ (because the FC approximation is usually well justified), we can now go *beyond* the FC approximation by computing the overlap matrix elements, f_{is}, and using them in Eq. (3.21) instead of d_{is}. As will be shown, this results in a slightly improved potential, most noticeably near the R_e region.

Explicitly,

$$\phi_s(\mathbf{R}) = \frac{\sum_i \chi_i(\mathbf{R}) d_{i,s}}{\mu_{e,g}(\mathbf{R})}. \tag{3.25}$$

We can now recompute the overlap integrals as,

$$f_{i,s} \equiv \langle \chi_i \mid \phi_s \rangle = \int d\mathbf{R} \frac{\sum_j \chi_j(\mathbf{R}) d_{j,s} \chi_i(\mathbf{R})}{\mu_{e,g}(\mathbf{R})}, \tag{3.26}$$

and use these new values in Eq. 3.21. We will return to this approach later in Sec. 3.7.2.

3.3 Application

3.3.1 Bound-Bound Diatomic Model

To better explain how the phase extraction procedure works we simplify the treatment by concentrating on bound-bound transitions of *diatomic* molecules, reporting about the use of continuum states in a later section (Sec. 3.4). In order to "jump-start" the inversion scheme, given that neither the signs of $d_{i,s}$, nor $V_e(R)$, nor $\phi_s(R)$ are initially known, we rely on the fact that the excited potential can be parametrized *near* its minimum position R_e as an harmonic, or better still, a Morse potential,

$$V_M(R) = D_e \left[\exp(-\beta(R - R_e)) - 1\right]^2 - D_e + T_e. \tag{3.27}$$

We can make a rough guess as to the value of R_e based on some measured intensity ratios, such as $|d_{0,0}|^2/|d_{1,0}|^2$. Likewise, we can estimate D_e, T_e, and β, based on the three lowest transition frequencies $\omega_{s=0,1,2;i=0}$, to the $i = 0$ ground vibrational level. It turns out that a rough initial estimate is all we need, as the final result is rather insensitive to it. Once we make any reasonable initial guess for V_e, we can obtain the signs of the transition-dipole matrix elements according to Eq. (3.13) (note that the magnitudes are already known from experiment), and substitute the results in Eq. (3.21) using only low-lying vibrational states, to obtain an improved estimate of $V_e(R)$ near R_e. This procedure can then be iterated until convergence.

As shown in Fig. (3.1), at this stage the potential is only known over a small

$$\left[\left(R_e - \frac{\Delta}{2}\right) - \left(R_e + \frac{\Delta}{2}\right)\right]$$

region, since we have used data pertaining to only its lowest lying $\phi_s(R)$ vibrational states. We now augment this region by smoothly extrapolating the potential using two exponential functions, one pertaining to $R < R_e - \frac{\Delta}{2}$ and the other pertaining to $R > R_e + \frac{\Delta}{2}$. We then compute a few higher vibrational states of the augmented potential, and re-calculate the signs of the $d_{i,s}$ matrix elements for all states considered thus far. We substitute the matrix elements thus obtained in Eq. (3.21) and iterate for $V_e(R)$ until convergence. We repeat this procedure anew, each time slightly increasing the Δ range of the potential for which Eq. (3.21) is used.
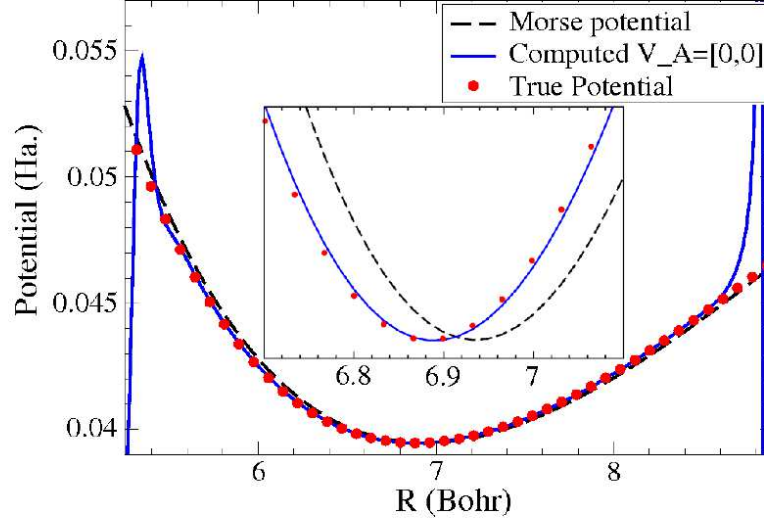
Figure 3.1: The beginning of the target potential extraction process near the minimum region, using a Morse potential as an initial guess.
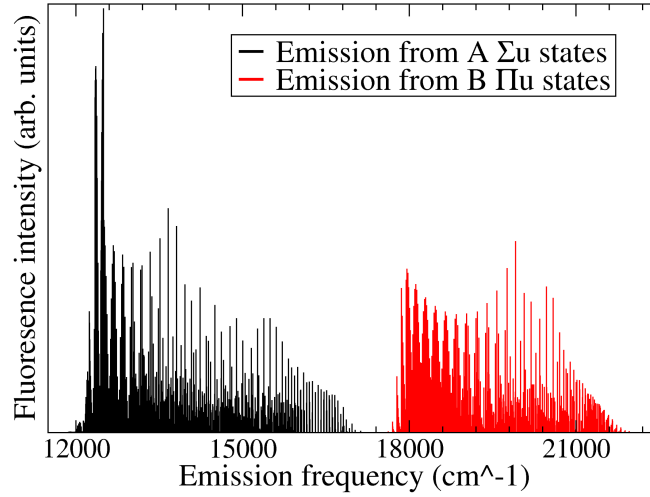
Figure 3.2: The simulated emission spectrum from the Na_2 $A(^1\Sigma_u^+)$ and $B(^1\Pi_u)$ potentials to the $X(^1\Sigma_g^+)$ potential, where we display the transitions between $\nu_A = [0-25]$ ($\nu_B = [0, 25]$) and $\nu_X = [0, 60]$ states.

3.3.2 Na$_2$ Single Well

As a realistic application of our procedure we now present the extraction of the A($^1\Sigma_u^+$) and B($^1\Pi_u^+$) excited state potentials of Na$_2$ from fluorescence data. We simulate the experimental fluorescence data by calculating $|d_{i,s}|^2$ for various transitions between the A($^1\Sigma_u^+$) and B($^1\Pi_u$) states and the ground X($^1\Sigma_g^+$) state, using the *ab initio* potentials and transition dipole functions as provided by Schmidt et al.[127]. In Fig. 3.2, we show the emission transition signals from the A($^1\Sigma_u^+$) and B($^1\Pi_u$) potentials to the X($^1\Sigma_g^+$) potential.
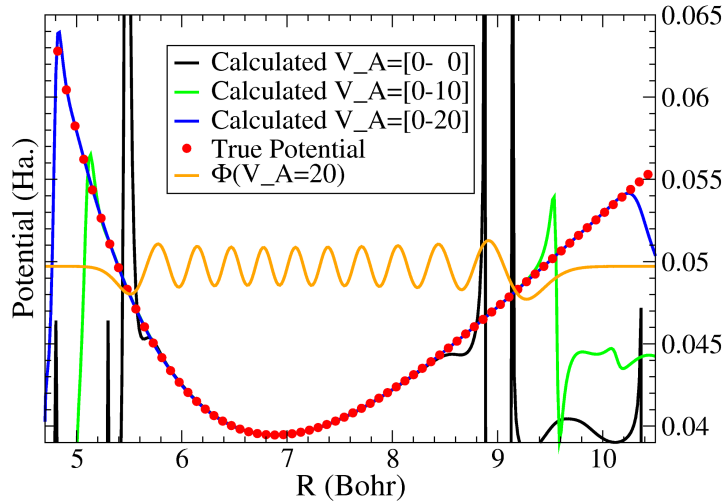
Figure 3.3: The A($^1\Sigma_u^+$) Na$_2$ potential extracted piece by piece by including an ever increasing number of excited vibrational states.

Given the above $|d_{i,s}|^2$ and $\omega_{i,s}$ line positions, we have computed the A($^1\Sigma_u^+$) potential from Eq. (3.21) using the $\nu_X = [0 - 60]$ and $\nu_A = [0 - 20]$ states. In Fig. 3.3, we see that the computed potential matches the *ab initio* potential very accurately, extending well beyond the turning points of the highest $\phi_s(\nu_A = 20)$ state. As we venture more and more into the classically forbidden regions, the magnitudes of the $\phi(\nu_A = 0 - 20)$ states start to diminish rapidly, eventually causing the error in the extracted potential to be unacceptable. As the number of included states is increased, a highly accurate excited potential appears to "spread out" to the right and left of R_e at an ever increasing Δ. At the end of the procedure,

Region	R_{left}	R_{right}	RMS with FCA	RMS Beyond FCA
Deep Well	LTP(0)	RTP(0)	0.19	0.01
Well	LTP(5)	RTP(5)	0.22	0.11
Left end	LTP(20)	LTP(18)	1.69	1.10
Right end	RTP(18)	RTP(20)	0.16	0.03
Global	LTP(20)	RTP(20)	0.33	0.55

Table 3.1: RMS errors (in cm^{-1}) of the A($^1\Sigma_u^+$) potential in different regions, extracted using the FC approximation and beyond, where LTP(ν) and RTP(ν) denote the left-turning-point and right-turning-point of a given ν^{th} vibrational state.

the range for which the potential is accurate is limited only by the range of the highest $\phi_s(R)$ vibrational state used. It is not possible to further increase the range of the extracted potential by including even higher ($\nu_A > 25$) states without also including the X($^1\Sigma_g^+$) continuum states [128]. The ground continuum states are needed to satisfy the completeness condition of Eq. (3.16) for the $\nu_A > 25$ high lying vibrational states.

We supplement the figures by providing in Table 3.1 the details about the root-mean-square (RMS) errors of the calculated A($^1\Sigma_u^+$) potential in the FC approximation and beyond. The various regions of interest are defined via the left (LTP(ν)), and right (RTP(ν)) turning points of a given vibrational level ν. The RMS errors are calculated between the inverted curve and the "true" *ab initio* potential within these different ranges of the potential. As expected, our accuracy decreases as we expand the well region where we calculate the RMS error from between the turning points of the $\nu = 0$, to the $\nu = 5$, to the $\nu = 20$ states. This is due to the increasing difficultly of expanding the higher excited states in the ground state basis of eigenstates. We also find larger errors appearing on the left (repulsive) wall arising from the inaccuracies in this expansion. Although we use this RMS error between the inverted and real curves throughout this chapter to quantify the accuracy of our inversion procedure, experimentalist may be more interested in how well we reproduce the spectral lines (*i.e.* how accurately do we find the energy eigenvalues). Unfortunately, there is no direct way to compare the RMS error of the extracted potential curve to the RMS error between the calculated and actual eigenenergies since it depends on how the discrepancies in the curves arise. Instead, the (global) RMS curve error can be thought of as an upper limit to the errors in line positions. In general, the latter are found to be at least half that due to oscillations in the calculated potential about

the "true" curve.
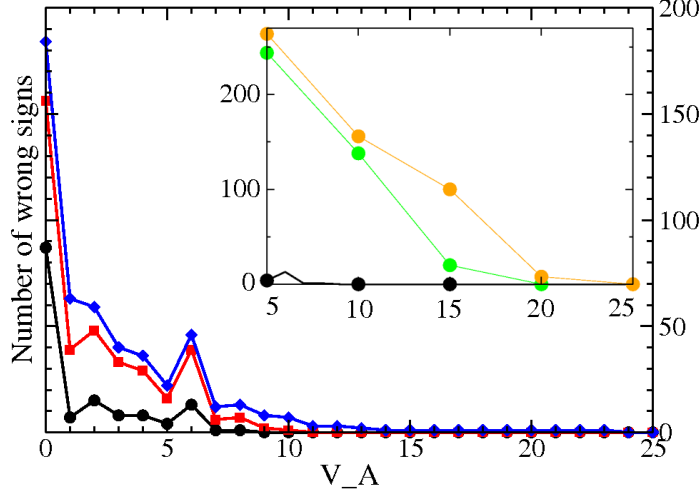
Figure 3.4: Number of wrong signs of transition dipole moments for the $A(^1\Sigma_u^+)$ Na_2 potential by including an ever increasing number of excited vibrational states, where the black circle, red square, and blue diamond lines denotes signal strength greater than 1×10^{-2}, 1×10^{-4}, and 1×10^{-6} of the peak signal, respectively. The small inset describes the same physical argument with different uncertainties in the measured signal strength (green: 5% uncertainty; orange: 10% uncertainty).

As shown in Fig. (3.4), the number of wrong computed signs of transition dipole moments (TDMs) for the $A(^1\Sigma_u^+)$ Na_2 potential decreases to zero as the number of excited vibrational states increases. The total number of transition lines between $\nu_A = [0 - 25]$ and $\nu_X = [0, 60]$ states is 1586. In Fig. (3.4), black circle denotes the data for signals strength greater than 1×10^{-2} of the peak signal, for which there are 623 transition lines. By increasing number of excited vibrational states and extending Δ, the calculated potential and the associated wavefunctions become more accurate, which directly improves the calculated signs of TDMs. We notice that, in Fig. (3.4), there are a total of 908 transitions whose signals strength are greater than 1×10^{-6} of the peak signal, signs for all of which are computed correctly when all $\nu_A = [0 - 25]$ states are included.

The results of our calculation for the $B(^1\Pi_u)$ potential, using the same number of states, are shown in Fig.3.5. Table 3.2 shows the RMS errors of the calculated $B(^1\Pi_u)$ potential in the different regions using the FC approximation and going beyond it.
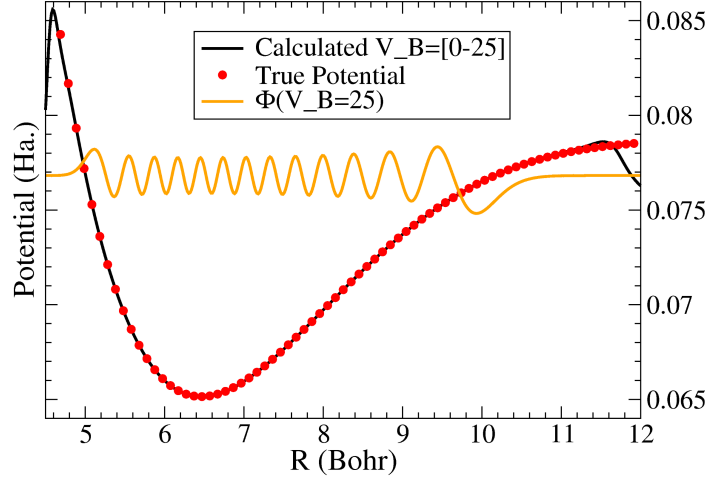
Figure 3.5: The extracted potential from Eq. (3.21) for the B($^1\Pi_u^+$) state.

Quite naturally, the FC approximation is most accurate near the equilibrium region where the wave functions are more tightly localized.

Na$_2$ Transition Dipole Function

As an application of the above procedure we have calculated the transition-dipole function $\mu_{e,g}(\mathbf{R})$ for the X($^1\Sigma_g^+$)←A($^1\Sigma_u^+$), B($^1\Pi_u^+$) transitions. Figure 3.6a shows the dipole function $\mu_{X,A}(R)$ produced using the $\nu_X = [0-60]$ and $\nu_A = [0-25]$ states. The extracted $\mu_{X,A}(R)$ function is in excellent agreement with the *ab-initio*

Region	R_{left}	R_{right}	RMS FCA	RMS Beyond FCA
Deep Well	LTP(0)	RTP(0)	0.11	0.07
Well	LTP(5)	RTP(5)	0.12	0.08
Left end	LTP(25)	LTP(23)	2.63	2.19
Right end	RTP(23)	RTP(25)	0.88	0.75
Global	LTP(25)	RTP(25)	0.33	0.29

Table 3.2: RMS errors (in cm^{-1}) of the B($^1\Pi_u^+$) potential in different regions, extracted using the FC approximation and beyond, where LTP(ν) and RTP(ν) denote the left-turning-point and right-turning-point of a given ν^{th} vibrational state.

one. It starts deviating from it only in the $R < 5.5$ Bohr and $R > 9.5$ Bohr deep tunneling regions.

Figure 3.6b shows the dipole function $\mu_{X,B}(R)$ using of the $\nu_X = [0-60]$ and $\nu_B = [0-25]$ states, where, similarly, $\mu_{X,B}(R)$ becomes less accurate in the deep tunneling region of the high-lying states of $\phi_s(\nu_B)$.

3.3.3 Robustness

In order to test the robustness of this procedure against insufficient or inaccurate fluorescence data, we performed several calculations. We considered the following sources of errors:

1. Missing lines, such as those connected with the low lying excited vibrational states.

2. Errors in the magnitudes of the measured $|d_{i,s}|^2$ line strengths.

Missing Lines.

As described above, in order to build the potential we start with the lowest vibrational states, e.g. $\nu_A = 0$, and construct the well region. Then, by iteratively including higher states, we extend the range of the inverted potential in a stepwise fashion. Note, not all transition data are required to be available because only 39.3% of the transitions are of real usefulness because the intensities of all the other transition are less than 1% of the highest transition intensity.

If the fluorescence lines associated with the lowest states are unavailable it would seem that this procedure might run into difficulties. This however is not the case, as we show by performing the potential extraction of the $A(^1\Sigma_u^+)$ state using only the $\nu_A = [1-25]$ or $\nu_A = [2-25]$ states. Fig. 3.7 shows the potentials extracted with the deficient data as compared to the complete $\nu_A = [0-25]$ case. Figure 3.7 clearly shows that this procedure is stable even when the fluorescence data for the $\nu_A = 0, 1$ states are unavailable.

One extreme case is that only a few emission bands from highly energetic vibrational states are available. In this case, it is still possible to generate a global potential with an RMS error of a few cm^{-1}. Table 3.3 shows the RMS error analysis for the global potential with the use of different number of transition bands, where we assume the available emission data are from $\nu_A = [20-25]$ highly energetic vibrational states. It is obvious that, even with only four vibrational states,
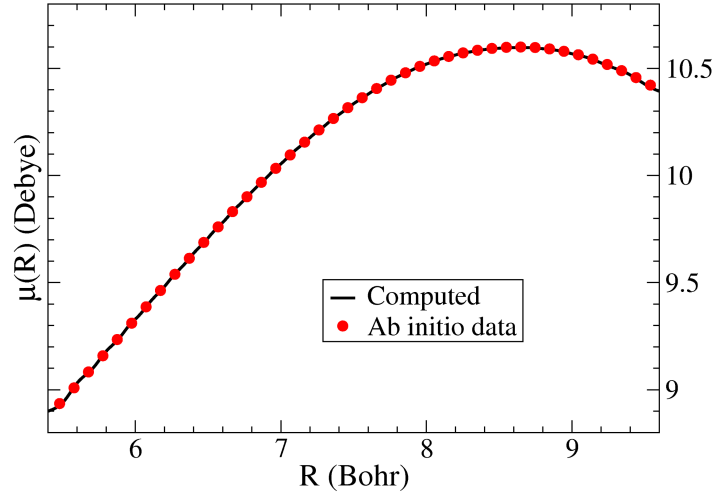
(a)
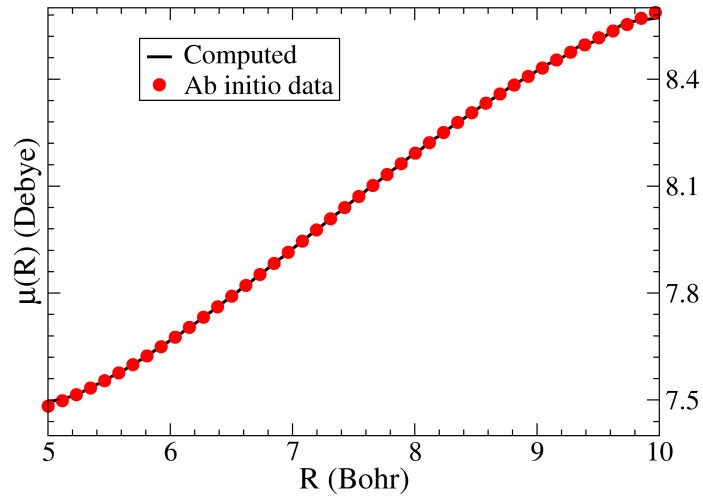
(b)

Figure 3.6: (a) The extracted dipole function $\mu_{X,A}(R)$ for transitions between the $X(^1\Sigma_g^+)$ and $A(^1\Sigma_u^+)$ potentials. (b)The extracted dipole function $\mu_{X,B}(R)$ for transitions between the $X(^1\Sigma_g^+)$ and $B(^1\Pi_u^+)$ potentials.
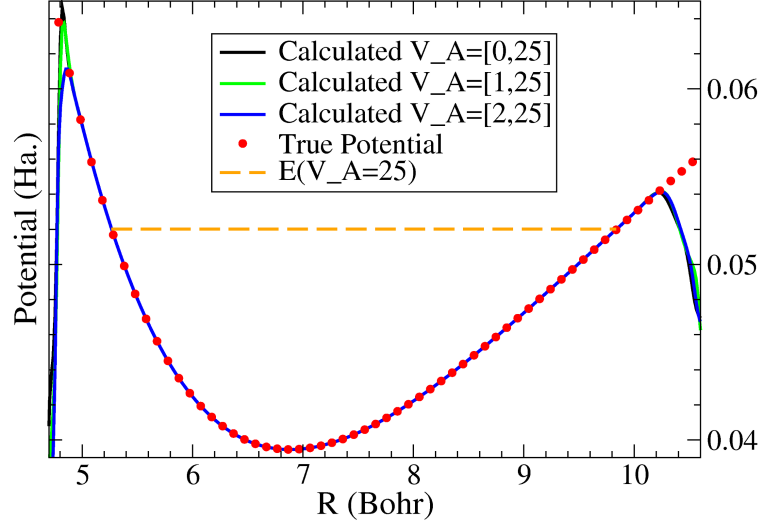
Figure 3.7: Computed A $^1\Sigma_u^+$ potentials with $\nu_A = [0-25]$, $[1-25]$ and $[2-25]$ states.

the global potential can be generated with an impressive accuracy with a 2.6 cm^{-1} error. This can be easily applied to experiments to locate the optimal intermediate state, which has good Frank-Condon overlaps with both the initial and final states, in the creation of low-vibrational states of diatomic molecules [30, 129, 130].

Errors in $|d_{i,s}|^2$.

To address this situation we have introduced random errors to the $|d_{i,s}|^2$ data and repeated the extraction of the potentials in the presence of such errors. The errors

ν_A used	RMS (cm^{-1})
$[24-25]$	7.8
$[23-25]$	4.1
$[22-25]$	2.6
$[21-25]$	2.0
$[20-25]$	1.7

Table 3.3: Global RMS errors of the A($^1\Sigma_u^+$) potential with different number of transition bands from only a few highly excited vibrational states ν_A.
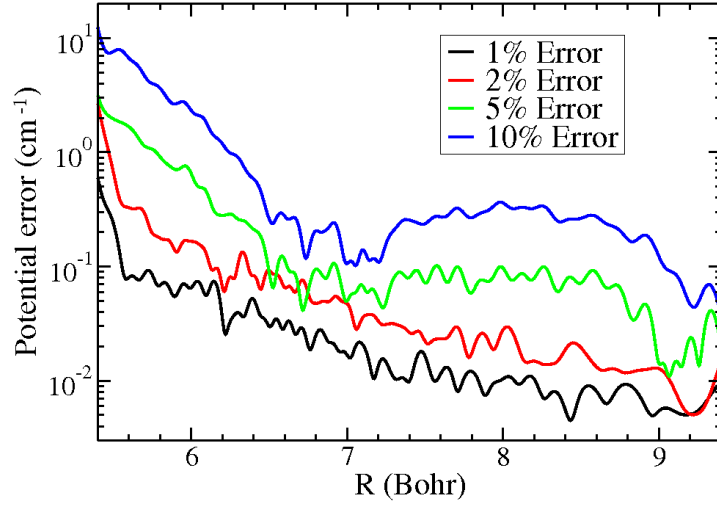
(a)
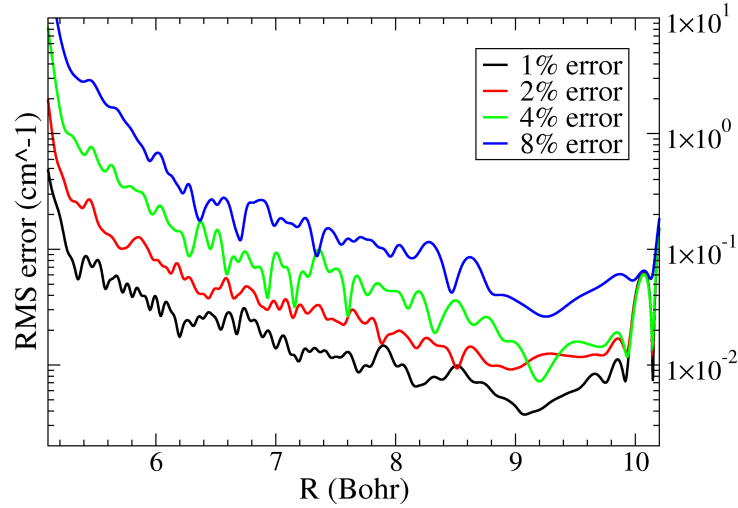
(b)

Figure 3.8: (a) The deviations of the average extracted $A(^1\Sigma_u^+)$ potential relative to the true *ab-initio* potential as a function of R, for different RMS errors of the simulated fluorescence line strengths. (b) Root-mean-square (RMS) errors of the constructed B $^1\Pi_u^+$ potential with a varying degree of errors in the experimental fluorescence data. $|d_{i,s}|^2$.

67

in $|d_{i,s}|^2$ were generated in a random fashion of 1%, 2%, 5% and 10% RMS errors relative to the average $|d_{i,s}|^2$ values. In Fig. (3.8a) we show the deviation from the *ab-initio* potential of the average $A(^1\Sigma_u^+)$ numerical potential at different R-values extracted from such data for the above magnitudes of errors. In Fig. (3.4) we also show the number of wrong calculated signs for the TDMs for the $A(^1\Sigma_u^+)$ potential with 0% (black), 5% (green), and 10% (orange) RMS errors in the measured signal strength, $|d_{i,s}|^2$, where signs for all 623 transition lines for signals strength greater than 1×10^{-2} of the peak signal are computed correctly! Figure (3.8a) and Fig. (3.4) demonstrate a remarkable robustness against inaccuracies in the experimental fluorescence data: Percentage-wise the deviations from the *ab initio* potential are much smaller than the relative experimental RMS error. We note that, in addition, no attempt was made to smoothly interpolate the numerically obtained average extracted potential values. It stands to reason that when such interpolations are introduced, the deviations from the true potential would be further reduced.

Similarly, in Fig. (3.8b) we show the deviation from the *ab-initio* potential of the average $B\ ^1\Pi_u^+$ numerical potential at different R-values extracted from such data, for the above magnitudes of errors. Figure (3.8b) demonstrates the remarkable robustness against inaccuracies in the experimental fluorescence data: Percentage-wise the deviations from the "true" potential are much smaller than the relative experimental RMS error.

3.4   Continuum States

We present an extension to the bound-continuum cases of our bound-bound inversion scheme for extracting excited state potentials and transition-dipoles from fluorescence data. The procedure involves the discretization of the continuous spectrum using box-normalization. The addition of the continuous spectrum guarantees completeness of the basis set used for the implicit expansion of the unknown excited state vibrational wave functions. Here we show how to extend these ideas by incorporating spectral information of bound-continuum transitions. We do so by discretizing the continuum, thereby circumventing the need for solving for the general phases associated with continuum-to-bound transitions.

We first show that the use of bound state information alone is insufficient in many cases, including the extraction of the $Na_2\ C(^1\Pi_u)$ electronic potential. In this demonstration we use an *ab initio* $V_g(R)$ potential [127], which is in agreement with

other sources [131–133]). Given $V_g(R)$, we generate χ_i, and E_i. We then use the *ab initio* [127] excited state potential, $V_e(R)$, to simulate the experimental emission spectrum to the ground state, consisting of $\omega_{i,s}$ and $|d_{i,s}|$. In order to determine the phases (signs, in the case of bound-bound transitions) of $d_{i,s}$, which enter Eq. 3.21, we begin with an initial estimate of $V_e(R)$. Given this estimate, we calculate an initial estimate of the signs of $d_{i,s}$. Since near the equilibrium position R_e, most diatomic potentials can be approximated by the Morse potential,

$$V_M(R) = D_e \left(e^{-2\beta(R-R_e)} - 2e^{-\beta(R-R_e)} \right) + T_e, \tag{3.28}$$

we perform a least-squares fit of the Morse parameters: T_e, D_e, and β to match a few of the transition frequencies $\omega_{s;i=0}$ to the $(E_s - E_i)/\hbar$ analytical values generated by $V_M(R)$.

A rough approximation as to the value of R_e can be made by observing the stationary-phase point associated with the transition intensity $|d_{s=0,i}|$ from the excited ground state $s = 0$, the flexibility allowed for in this value is shown below.

Using this method we have computed the $C(^1\Pi_u)$ potential. The end result shown in Fig. 3.9 matches the *ab initio* potential to a root-mean-squared (RMS) accuracy of 0.1 cm^{-1} in the Δ region. The potential extends well beyond the turning points of the highest $\phi_s(\nu_C)$ state, and fails only when the magnitudes of all the $\phi(\nu_C = 0-32)$ states have become so small in the classically forbidden region that the calculation becomes numerically unstable.

Restrictions

In view of the above one would like to use as many $\phi_s(R)$ states as possible. However the number of $\phi_s(R)$ states is restricted because we cannot always maintain C_s of the following completeness condition close enough to unity

$$1 \geq C_s \equiv \sum_{i=1}^{i_{max}} |\langle \chi_i | \phi_s \rangle|^2, \tag{3.29}$$

where i_{max} is the highest ground vibrational state included in the expansion (Eq. 3.16).

Figure (3.9) clearly shows the limited extent for which the Na$_2$ C$(^1\Pi_u)$ potential can be computed based solely on bound-bound transition data. Of the approximately 73 bound states in C$(^1\Pi_u)$ we are only able to accuracy include up to state $s = 32$
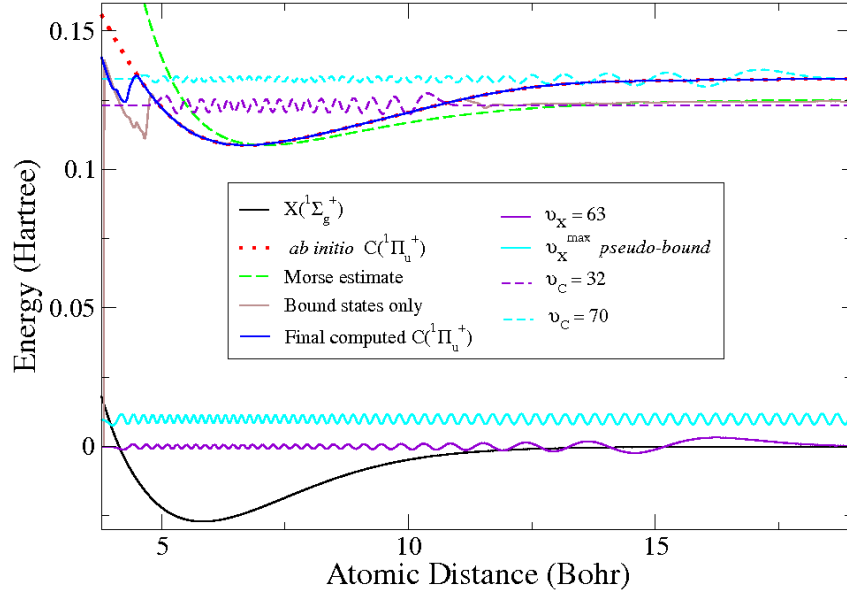
Figure 3.9: (Black line) - the ground $X(^1\Sigma_g^+)$ Na$_2$ state. (Red dots) - *ab initio* energies of the excited $C(^1\Pi_u)$ potential; (Green dashed line) - the initial Morse fit. (Brown line) - the partial Na$_2$ $C(^1\Pi_u)$ potential extracted using only the $s = [0, 32]$ excited bound states and the $i = [0, 63]$ vibrational ground states. (Violet) - the highest vibrational states used. (Blue) - the entire excited $C(^1\Pi_u)$ potential extracted using the $s = [0, 110]$ states. (Cyan) - the highest vibrational state used. This extraction can only be done when we incorporate transitions to the continuum of the ground $X(^1\Sigma_g^+)$ state. The RMS deviation of the potential extracted in this way from the *ab initio* potential is 0.1 cm^{-1}.

(upper grey line) using the $i = [0, 63]$ bound states of $X(^1\Sigma_g^+)$ in the expansion. Thus, it is not possible to further increase the range of the extracted potential by simply including higher $(s > 32)$ states without first increasing the size of our basis set for expansion. Thus the only solution is to enlarge our basis by including the $X(^1\Sigma_g^+)$ continuum states. We discuss how to implement this approach and deal with the continuous spectrum in the next section.

3.4.1   Box Normalization

As mentioned above, we wish to include the continuum states in our procedure in order to satisfy the completeness condition [134, 135]

$$\sum_{i=1}^{i_{max}} |\chi_i(\mathbf{R})\rangle\langle\chi_i(\mathbf{R})| + \int |\chi(k, \mathbf{R})\rangle\langle\chi(k, \mathbf{R})| \ dk = \mathbf{1} \qquad (3.30)$$

over as large a range of $\mathbf{R}$ values as possible. However, dealing directly with the continuum states is difficult because the transition dipole matrix elements, $d_{s,k}$, are complex numbers when $|k\rangle$ are scattering states. To avoid this difficulty we replace the true scattering states, $\chi(k, \mathbf{R})$, with discretized box-normalized [136–139] scattering states, $\chi_k(\mathbf{R})$. In this way we are in effect binning the continuous spectrum into discrete intervals, each being represented by a box-normalized state. We have that,

$$\int |\chi(k, \mathbf{R})\rangle\langle\chi(k, \mathbf{R})| \ dk \approx \sum_{k}^{k_{max}} |\chi_k(\mathbf{R})\rangle\langle\chi_k(\mathbf{R})| \qquad (3.31)$$

In order to bin $d_s(k)$, the "true" bound continuum dipole matrix-elements, we compare $d_{k,s}$, the dipole matrix elements for the box-normalized states, with integrals over a range of continuous $d_s(k)$ values,

$$\overline{d_{k,s}} \equiv \int_{k-\delta_{k_-}}^{k+\delta_{k_+}} d_s(k') \ dk' \qquad (3.32)$$

where $\delta_{k_-} = (E_k - E_{k-1})/2$ and $\delta_{k_+} = (E_{k+1} - E_k)/2$. In order to do that we first compute the "true" bound-continuum $d_s(k)$ matrix elements using the artificial channel method (ACM) [51–53], for all the transitions between the $s = 1, ..., 40$ vibrational states of the Na_2 $C(^1\Pi_u)$ to continuum states whose energies start at
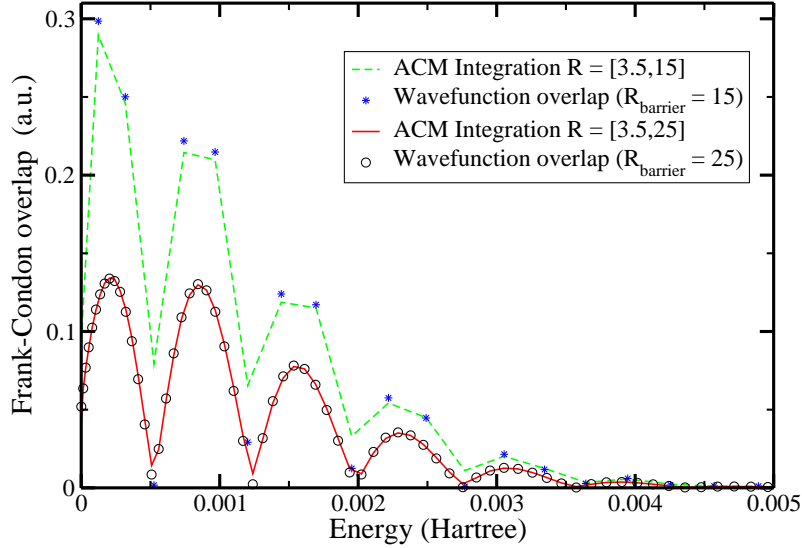
Figure 3.10: The $d_{s,k}/\overline{\mu}$ Franck-Condon factors from the $s = 40$ state of the Na$_2$ C($^1\Pi_u$) state to the discretized continuum states of the X($^1\Sigma_g^+$) state for two different boxes: Blue stars - the $R = [0 - 15]$ box results; black circles - the $R = [0 - 25]$ box results. The "exact" $d_s(k)/\overline{\mu}$ values, as obtained using the ACM scheme, are marked by a dashed green line for the $[3.5 - 15]$ Bohr range and as a red line for the $[3.5 - 25]$ Bohr range .

just above the dissociation limit of X($^1\Sigma_g^+$).

Using two normalization boxes, the inner wall of both of which is placed at $R = 0$ and the outer walls - at either $R = 15$ Bohr or at $R = 25$ Bohr, we calculate $\overline{d_{k,s}}$ according to Eq. (3.32) and compare them to $d_{k,s}$. The results are shown in Figs. 3.10. We see that the smaller normalization box results in substantial inaccuracies due to the very sparseness of the box-normalized levels. As we increase the size of the box, the density of the box-normalized states increases, and so does the accuracy of the binning, resulting in an excellent agreement for $R = 25$ Bohr (and even for $R = 20$ Bohr) between $\overline{d_{k,s}}$ and $d_{k,s}$.

The success of the box normalization procedure allows us to use the set of $d_{k,s}$ matrix elements in exactly the same way we use any set of bound-bound matrix elements in our bound-bound inversion procedure, enabling us to use the information contained in the bound-continuum transitions. In this way we have effectively converted the difficult bound-continuum phase problem into the sign-determination problem of the bound-bound case.

We can therefore extend the excited wave function expansion of Eq. (3.16) over
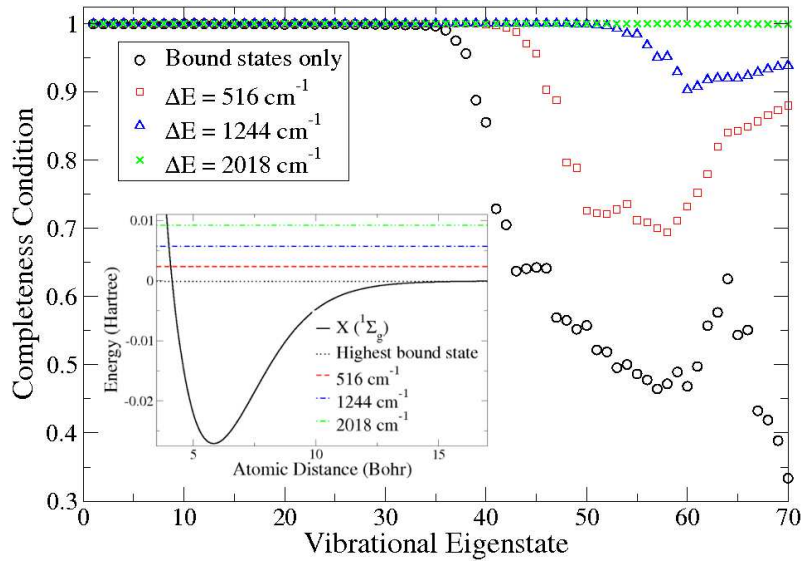
Figure 3.11: The values of C_s of Eq. (3.29), representing the completeness condition, for each of the ϕ_s states of the $C(^1\Pi_u)$ potential, as more and more $X(^1\Sigma_g^+)$ $(\chi_i + \chi(k))$ vibrational states are included in the expansion. Shown are C_s values for $i = 1, ..., 63$ (black circles); when we add to these states all the $\chi(k)$ continuum states below 516 cm^{-1} (red squares); all the continuum states below 1244 cm^{-1} (blue triangles); and all the continuum states below 2018 cm^{-1} (green x's). The inset shows these energy levels relative to the dissociation energy of the $X(^1\Sigma_g^+)$ potential.

all available states. The quality of this expansion for each individual excited state can be expressed via the C_s completeness parameter of Eq. (3.29), which approaches unity when the basis becomes complete. In Fig. 3.11 we plot the value of C_s for each of the bound states ϕ_s of $C(^1\Pi_u)$ when we include 63 vibrational bound state in $X(^1\Sigma_g^+)$ ($\circ$), and when we add box-normalized continuum states covering an energy range of 516 cm^{-1} ($\square$), 1244 cm^{-1} ($\triangle$), and 2018 cm^{-1} ($\times$). As expected, the number of excited states that can be accurately represented increases with the increase in basis set, until all the bound states of $C(^1\Pi_u)$ can be well reproduced by the ground states expansion.

3.4.2 Extraction of the Entire Na$_2$ $C(^1\Pi_u)$ Potential

In Fig. 3.9 we have shown how the inclusion of continuum state allows us to extract the *entire* Na$_2$ $C(^1\Pi_u)$ potential curve. In order to do so we have supplemented the bound-bound transitions (including the $i = 1, ..., 70$ bound states) with the box-normalized continuum states whose energies reach 2000 cm^{-1} above the dissociation limit. The box-normalized continuum state of the highest energy considered is also shown in the figure. We have incorporated only half of the transitions (those with probability $> 0.1\%$) and obtained RMS deviation from the exact potential of less than 0.1 cm^{-1}.

3.5 Double Well

3.5.1 Morse Model

In order to show that our approach is capable of extracting potential energy curves with several minima, we have examined a model double-Morse potentials of the form,

$$V(R) = f(R)V_1(R) + [1 - f(R)]V_2(R), \tag{3.33}$$

where $f(R)$ is a smooth switching function

$$f(R = (1 + \tanh[(R - 9.12)/0.3])/2 \tag{3.34}$$

and V_1 and V_2 are Morse potentials whose parameters are, $De_1 = 8 \times 10^{-3}$ a.u., $\beta_1 = 0.2952$ a.u., $Re_1 = 6.94$ Bohr, $De_2 = 6 \times 10^{-3}$ a.u., $\beta_2 = 0.29$ a.u., and $Re_2 = 10$ Bohr. By adopting the same approach and using the FCA, we extract

the potential by adding vibrational states ν in Eq. (3.21). Fig. 3.12 shows the building process of the double-well potential obtained by considering the transitions associated with the $\nu = [0-11]$ states. The reason behind the successful construction lies in the extension of the wave function beyond the classical turning points. Thus, though the $\nu = 5$ vibrational state is well localized in the left well, the wave function $\phi(\nu = 5)$ spills over to the second well, thereby enabling the accurate extraction of the second minimum.
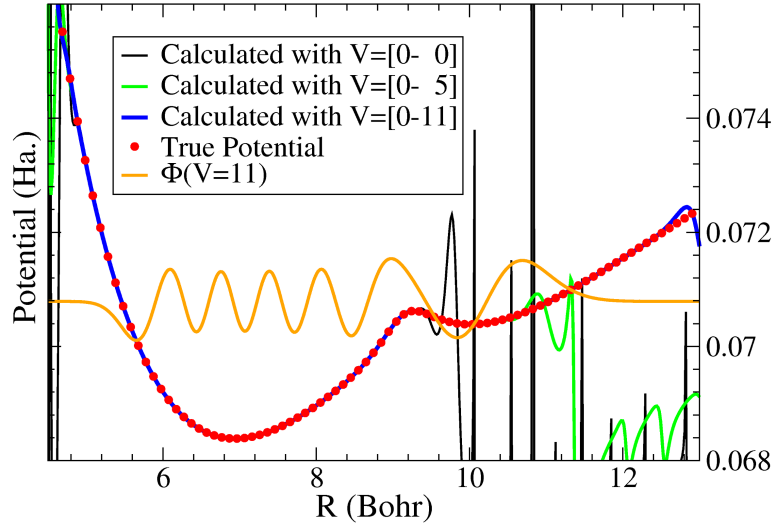
Figure 3.12: Step-wise construction of a model double-well potential.

3.5.2 Extraction of the Na$_2$ 2$^1\Sigma_u^+$(3s+4s) Double Well Potential

As a more sophisticated demonstration of the use of continuum states, we present the extraction of a double well potential, that of the Na$_2$ 2$^1\Sigma_u^+$(3s+4s) state [100, 127, 140]. In this $\Sigma_g^+ \rightleftharpoons \Sigma_u^+$ transition we use for simplicity only the rotation-less 2$^1\Sigma_u^+$(3s+4s) states. These states are coupled optically to the $J = 1$ X$^1\Sigma_g^+$ rovibrational levels, hence we add a centrifugal potential of $1/(MR^2)$ to the electronic ground state potential.

With the use of only the bound states of X($^1\Sigma_g^+$), we are restricted by the lack of completeness to reconstructing the 2$^1\Sigma_u^+$(3s+4s) potential at energies below $E_{s=5}$

of the deeper well. In contrast, the addition of continuum transitions over a range of about 2300 cm^{-1} above the ground state dissociation limit, allows for over 110 bound states of the $2^1\Sigma_u^+$(3s+4s) potential to be accurately expanded in the ground state basis set.

In Fig. 3.13 we show how the piecewise potential re-construction proceeds. We start with the $s = 5$ bound state (blue dashed line) and proceed to the $s = 13$ level (green dot-dashed line). This level yields the first indication that an additional well might exist (brown colored lines): The inclusion of the $s = 13$ state causes the potential to exhibit a new oscillatory behavior at a region which up till now was smoothly increasing.
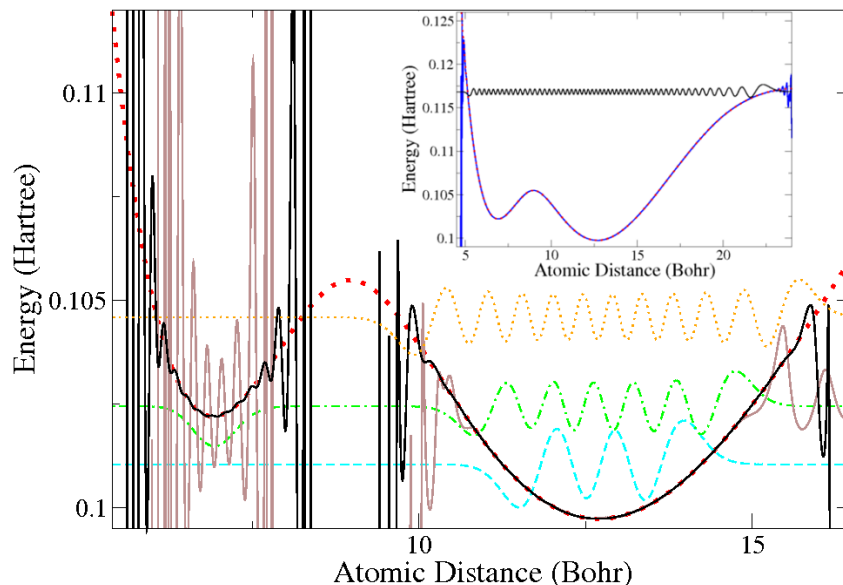
Figure 3.13: The wave functions of the fifth vibrational state (dashed) shows the maximal energy to which we are able to re-construct the Na$_2$ $2^1\Sigma_u^+$(3s+4s) potential using only the bound states of the X($^1\Sigma_g^+$) state. In contrast, the inclusion of continuum states up to the 2300 cm^{-1} above the dissociation threshold allows for a complete re-construction of the potential curve. The $s = 13$ vibrational level (dot-dashed) exhibits the first indication that an additional well (brown line) might exist. Using this information to smoothly extrapolate the next potential iteration reveals more of the second well (black line). The two wells and the barrier between them assume their fully developed forms (dotted line) when the $s = 27$ state is introduced. The inset shows the complete re-construction (blue line) of the $2^1\Sigma_u^+$(3s+4s) potential using up to the $s = 110$ state (black line). The RMS deviation of this potential from the *ab initio* one (red dots) is less than 1 cm^{-1}.

We thus proceed by averaging over the highly oscillating region on the left and

linearly extrapolating the inner and outer regions of the two wells. The new set of eigenstates thus obtained account to some extent for the contribution of the second well. As we introduce new eigenstates and iterate this procedure, the potential begins to converge in the two well regions (see black line in Fig. 3.13). Upon reaching level $s = 27$ (dotted-line) we have fully resolved the potential hump between the wells due to the information contained in the tunneling tails of the vibrational wave functions. Continuing onward, we end the construction of this potential at the $s = 110$ vibrational state ($E_{110} \sim 0.116833$ a.u.) finding that we have extracted the repulsive wall of the double well potential nearly 1000 wave-numbers above the known atomic asymptote of Na(3s) + Na(4s) (0.11728 Hartree at about 56.7 Bohr [100, 140]). The blue curve in Fig. 3.13 displays the final result constituting the extraction of the double well potential to within 1 cm^{-1} RMS error.

One drawback of the present inversion is that our procedure so far assumes the FCA which is not justified in the present case because there is a substantial difference [141, 142] between the dipole function at each well. Thus one has to go beyond the FCA, as we will show in Sec.3.7 (see Ref. [7]). However, first, we also introduce an approach to image diatomic potentials using different rotational bands.

3.6   Rotational States

Here we demonstrate how to image diatomic potentials using data from different rotational bands. We will assume that we have emission spectrum for only two excited rovibrational states exist: (s, J_1) and (t, J_2) where $s \neq t$ and $J_1 \neq J_2$. Recall that we need at least two states in our fundamental expression to kill the nodal behavior in the denominator. Thus, we wish to express the excited state electronic PES as:

$$V_{ex}(R) = f\left(V_{gr}(R), \chi_i[J_1'], \chi_m[J_2'], \omega, J_1, J_2\right) \tag{3.35}$$

where $V_{gr}(R)$ is the ground state PES, ω is the transition frequency, and $\chi_i[J_1]$ and $\chi_m[J_2]$ are ground state rovibrational wavefunction with angular momentums of J_1' and J_2', respectively. For simplicity, we will use i, j, s to denote the quantities associated with transitions from (s, J_1) and use m, n, t to denote the quantities associated with transitions from (t, J_2).

3.6.1 Inversion Formula for R and P Branches

Consider when we use only one state, (s, J_1), and we take the R branch first: $(s, J_1) \to (i_1, J_1 - 1)$. The previous inversion formula for the Q branch [143, 144]

$$V_{ex}(R)(\text{Q branch}) = \frac{\sum_{i,j} d^*_{i,s} d_{j,s} \omega_{i,s} \chi^*_i(R) \chi_j(R)}{|\sum_i \chi_i(R) d_{i,s}|^2} + V_{gr}(R), \qquad (3.36)$$

then becomes

$$\left[V_{ex}(R) + \frac{J_1(J_1 + 1)}{2\mu R^2} \right] (\text{R branch}) = \frac{\sum_{i,j} d^*_{i,s} d_{j,s} \omega_{i,s} \chi^*_i(R) \chi_j(R)}{|\sum_i \chi_i(R) d_{i,s}|^2} + \left[V_{gr}(R) + \frac{J_1(J_1 - 1)}{2\mu R^2} \right], \qquad (3.37)$$

and thus

$$V_{ex}(R)(\text{R branch}) = \frac{\sum_{i,j} d^*_{i,s} d_{j,s} \omega_{i,s} \chi^*_i(R) \chi_j(R)}{|\sum_i \chi_i(R) d_{i,s}|^2} + V_{gr}(R) - \frac{2J_1}{2\mu R^2}. \qquad (3.38)$$

As before, we add a summation over all s to express a more general term which avoids nodal structure in the denominator of Eq. [3.38]

$$V_{ex}(R)(\text{R branch}) = \frac{\sum_s \sum_{i,j} d^*_{i,s} d_{j,s} \omega_{i,s} \chi^*_i(R) \chi_j(R)}{\sum_s |\sum_i \chi_i(R) d_{i,s}|^2} + V_{gr}(R) - \frac{2J_1}{2\mu R^2}. \qquad (3.39)$$

And, similarly for the P branch transition the inversion formula is given by

$$V_{ex}(R)(\text{P branch}) = \frac{\sum_s \sum_{i,j} d^*_{i,s} d_{j,s} \omega_{i,s} \chi^*_i(R) \chi_j(R)}{\sum_s |\sum_i \chi_i(R) d_{i,s}|^2} + V_{gr}(R) + \frac{2J_1}{2\mu R^2}. \qquad (3.40)$$

3.6.2 Inversion Formula for Different Rotational States, J_1 and J_2

Now we consider the probable scenario that there are only two sets of emission data ready to be used: (s, J_1) and (t, J_2). However, with limited source of experimental measurements, as in Ref. [145], there is often not much freedom to choose two excited states within the same branch and the same rotational quantum number. Let us take the case that $J_1 \neq J_2$ but they both correspond to the R branches, i.e. transitions for $(s, J_1) \to (i, J_1 - 1)$ and $(t, J_2) \to (m, J_2 - 1)$. The inversion formula

using these two excited states is derived similar to before (Eq. (3.39))

$$
\begin{aligned}
V_{ex}(R)(\text{R branch}) &= \frac{\sum_{i,j} d_{i,s}^* d_{j,s}\left(\omega_{i,s} - \frac{2J_1}{2\mu R^2}\right)\chi_i^*(R)\chi_j(R)}{|\sum_i \chi_i(R)d_{i,s}|^2 + |\sum_m \chi_m(R)d_{m,t}|^2} \\
&+ \frac{\sum_{m,n} d_{m,t}^* d_{n,t}\left(\omega_{m,t} - \frac{2J_2}{2\mu R^2}\right)\chi_m^*(R)\chi_n(R)}{|\sum_i \chi_i(R)d_{i,s}|^2 + |\sum_m \chi_m(R)d_{m,t}|^2} \\
&+ V_{gr}(R). \tag{3.41}
\end{aligned}
$$

Again, we use i, j, s to denote the quantities associated with transitions from (s, J_1) and use m, n, t to denote the quantities associated with transitions from (t, J_2).

Again, the general form for using more vibrational states with the same J_1 and/or J_2 numbers can be derived by including summations over these labels to improve extraction accuracy:

$$
\begin{aligned}
V_{ex}(R)(\text{R branch}) &= \frac{\sum_s \sum_{i,j} d_{i,s}^* d_{j,s}\left(\omega_{i,s} - \frac{2J_1}{2\mu R^2}\right)\chi_i^*(R)\chi_j(R)}{\sum_s |\sum_i \chi_i(R)d_{i,s}|^2 + \sum_t |\sum_m \chi_m(R)d_{m,t}|^2} \\
&+ \frac{\sum_t \sum_{m,n} d_{m,t}^* d_{n,t}\left(\omega_{m,t} - \frac{2J_2}{2\mu R^2}\right)\chi_m^*(R)\chi_n(R)}{\sum_s |\sum_i \chi_i(R)d_{i,s}|^2 + \sum_t |\sum_m \chi_m(R)d_{m,t}|^2} \\
&+ V_{gr}(R). \tag{3.42}
\end{aligned}
$$

Likewise, the inversion formula can be derived in a similar fashion for pure P branch transitions as well

$$
\begin{aligned}
V_{ex}(R)(\text{P branch}) &= \frac{\sum_s \sum_{i,j} d_{i,s}^* d_{j,s}\left(\omega_{i,s} + \frac{2J_1}{2\mu R^2}\right)\chi_i^*(R)\chi_j(R)}{\sum_s |\sum_i \chi_i(R)d_{i,s}|^2 + \sum_t |\sum_m \chi_m(R)d_{m,t}|^2} \\
&+ \frac{\sum_t \sum_{m,n} d_{m,t}^* d_{n,t}\left(\omega_{m,t} + \frac{2J_2}{2\mu R^2}\right)\chi_m^*(R)\chi_n(R)}{\sum_s |\sum_i \chi_i(R)d_{i,s}|^2 + \sum_t |\sum_m \chi_m(R)d_{m,t}|^2} \\
&+ V_{gr}(R). \tag{3.43}
\end{aligned}
$$

Simple extensions include finding mixed branch transitions for different rotational

states: namely for R+P branches:

$$
\begin{aligned}
V_{ex}(R)(\text{R+P branches}) \;=\;& \frac{\sum_s \sum_{i,j} d^*_{i,s} d_{j,s} \left(\omega_{i,s} - \frac{2J_1}{2\mu R^2}\right) \chi^*_i(R)\chi_j(R)}{\sum_s |\sum_i \chi_i(R)d_{i,s}|^2 + \sum_t |\sum_m \chi_m(R)d_{m,t}|^2} \\
+\;& \frac{\sum_t \sum_{m,n} d^*_{m,t} d_{n,t} \left(\omega_{m,t} + \frac{2J_2}{2\mu R^2}\right) \chi^*_m(R)\chi_n(R)}{\sum_s |\sum_i \chi_i(R)d_{i,s}|^2 + \sum_t |\sum_m \chi_m(R)d_{m,t}|^2} \\
+\;& V_{gr}(R);
\end{aligned}
\tag{3.44}
$$

for R+Q branches:

$$
\begin{aligned}
V_{ex}(R)(\text{R+Q branches}) \;=\;& \frac{\sum_s \sum_{i,j} d^*_{i,s} d_{j,s} \left(\omega_{i,s} - \frac{2J_1}{2\mu R^2}\right) \chi^*_i(R)\chi_j(R)}{\sum_s |\sum_i \chi_i(R)d_{i,s}|^2 + \sum_t |\sum_m \chi_m(R)d_{m,t}|^2} \\
+\;& \frac{\sum_t \sum_{m,n} d^*_{m,t} d_{n,t} \left(\omega_{m,t}\right) \chi^*_m(R)\chi_n(R)}{\sum_s |\sum_i \chi_i(R)d_{i,s}|^2 + \sum_t |\sum_m \chi_m(R)d_{m,t}|^2} \\
+\;& V_{gr}(R);
\end{aligned}
\tag{3.45}
$$

and for Q+P branches:

$$
\begin{aligned}
V_{ex}(R)(\text{Q+P branches}) \;=\;& \frac{\sum_s \sum_{i,j} d^*_{i,s} d_{j,s} \left(\omega_{i,s}\right) \chi^*_i(R)\chi_j(R)}{\sum_s |\sum_i \chi_i(R)d_{i,s}|^2 + \sum_t |\sum_m \chi_m(R)d_{m,t}|^2} \\
+\;& \frac{\sum_t \sum_{m,n} d^*_{m,t} d_{n,t} \left(\omega_{m,t} + \frac{2J_2}{2\mu R^2}\right) \chi^*_m(R)\chi_n(R)}{\sum_s |\sum_i \chi_i(R)d_{i,s}|^2 + \sum_t |\sum_m \chi_m(R)d_{m,t}|^2} \\
+\;& V_{gr}(R).
\end{aligned}
\tag{3.46}
$$

Lastly, a generalized inversion formula of Eq. (3.21) using all three branches can be given, where the R branch involves the $J' = J_1 \to J'' = J_1 + 1$ transitions, the Q branch would correspond to the $J' = J_2 \to J'' = J_2$ transitions, and the P branch - to the $J' = J_3 \to J'' = J_3 - 1$ transitions. Using standard spectroscopic notation ground states are denoted by J'', and we use J' for the excited state.

$$
\begin{aligned}
V_{\text{ex}}(R)(\text{R+Q+P branches}) \;=\; & \frac{1}{A}\Bigg\{\sum_s\sum_{i,j} d_{i,s}^* d_{j,s}\left(\omega_{i,s}-\frac{2J_1}{2\mu R^2}\right)\chi_i^*(R)\chi_j(R) \\
& +\; \sum_t\sum_{m,n} d_{m,t}^* d_{n,t}\left(\omega_{m,t}\right)\chi_m^*(R)\chi_n(R) \\
& +\; \sum_u\sum_{k,l} d_{k,t}^* d_{l,u}\left(\omega_{k,u}+\frac{2J_3}{2\mu R^2}\right)\chi_k^*(R)\chi_l(R)\Bigg\} \\
& +\; V_{gr}(R),
\end{aligned}
\tag{3.47}
$$

where $A \equiv \sum_s |\sum_i \chi_i(R)d_{i,s}|^2 + \sum_t |\sum_m \chi_m(R)d_{m,t}|^2 + \sum_u |\sum_l \chi_l(R)d_{l,u}|^2$. Note, a summation over J_1, J_2 and J_3 can be made when more than one rotational excited states exist within the same branch.

3.7 Extensions

In this section we present two works which extend our inversion method. The first to multi-dimensional potentials [6]:

(A) X. Li and M. Shapiro, *Inversion of two-dimensional potentials from frequency-resolved spectroscopic data*, J. Chem. Phys. **134**, 094113 (2011) ,
and the second to obtaining solutions beyond the FCA [7]:

(B) X. Li and M. Shapiro, *The Dipole Correction Method for Extracting Excited State Potentials and Electronic Transition Dipoles from Fluorescence Data*, Isr. J. Chem. **52**, 1-7 (2012) .

The author was intimately involved in the discussions and verification of the results leading to manuscript (A), although, the writing and processing was solely carried-out by Dr. Xuan Li with the support of Dr. Moshe Shapiro. The work contained in (B) is an elaboration of results already presented (see Sec. (3.2.3)). The author participated closely in discussions leading to the manuscript, which was composed and submitted by Dr. Xuan Li and Dr. Moshe Shapiro

3.7.1 Two Dimensional Potentials

To date, the determination of multi-dimensional PESs have relied on *ab initio* [34] or semiempirical [35–38, 117–119] quantum chemistry computations. Unfortunately,

these calculations are not capable of finding the spectroscopic line positions to the same accuracy as experimental measurements, this is in particular true for PES with many degrees of freedom (DOF). A lot of effort [81, 89, 98, 146–149, 149, 150]. has been put forth into studying polyatomics, however, the Hamiltonians based on internal modes becomes complicated due to distortions in the normal mode structure due to anharmonic couplings, Duschinksy rotations [151], and rotational (Coriolis) couplings [152]. Even though new coordinates which diagonize the kinetic energy operator may simplify matters [56], no systematic approach exists for extracting a PES for experimental data.

Here, we review the extension of the inversion procedure that was used to obtain one-dimensional PES from the spectroscopic line positions and line strengths for diatomic molecules. The model is based on representing a linear triatomic molecule with two degrees of vibrational freedom, or, a torsion and bending mode within a polyatomic system. For complete details see Ref. [6]

Linear Triatomic Model

For modeling a linear triatomic molecule with two vibrational DOF, we can define two independent coordinates:

$$
\begin{aligned}
R &= x_1 - \frac{m_2 x_2 + m_3 x_3}{m_2 + m_3} \ , \quad \text{and,} \\
r &= r_1 = |x_3 - x_2| \ ,
\end{aligned}
\tag{3.48}
$$

where m_i and x_i are the masses and one-dimensional positions of the three atoms respectively. The two-dimensional potential model, $V(\mathbf{R})$, will be represented as a sum of independent, one-dimensional, potentials between each atom. For instance, the pairwise potentials between atoms i and j will be given as $V_k(r_k)$, $k \neq i, j$ where r_k, $k \neq i, j$ is the distance between the two atoms i and j. Therefore, the ground state PES will be given as

$$
V_g(r_1, r_2, r_3) = V_1^g(r_1) + V_2^g(r_2) + V_3^g(r_3) \ ,
\tag{3.49}
$$

where the $V_k^g(r_k)$, $k = \{1, 2, 3\}$, potentials can be taken as three Na_2 $X(^1\Sigma_g^+)$ ground state potentials [127].

The excited state potential, $V_{\text{ex}}(\mathbf{R})$, will be modeled in the same way except for a three-body term to account for distortions, as well as, a constant term giving the
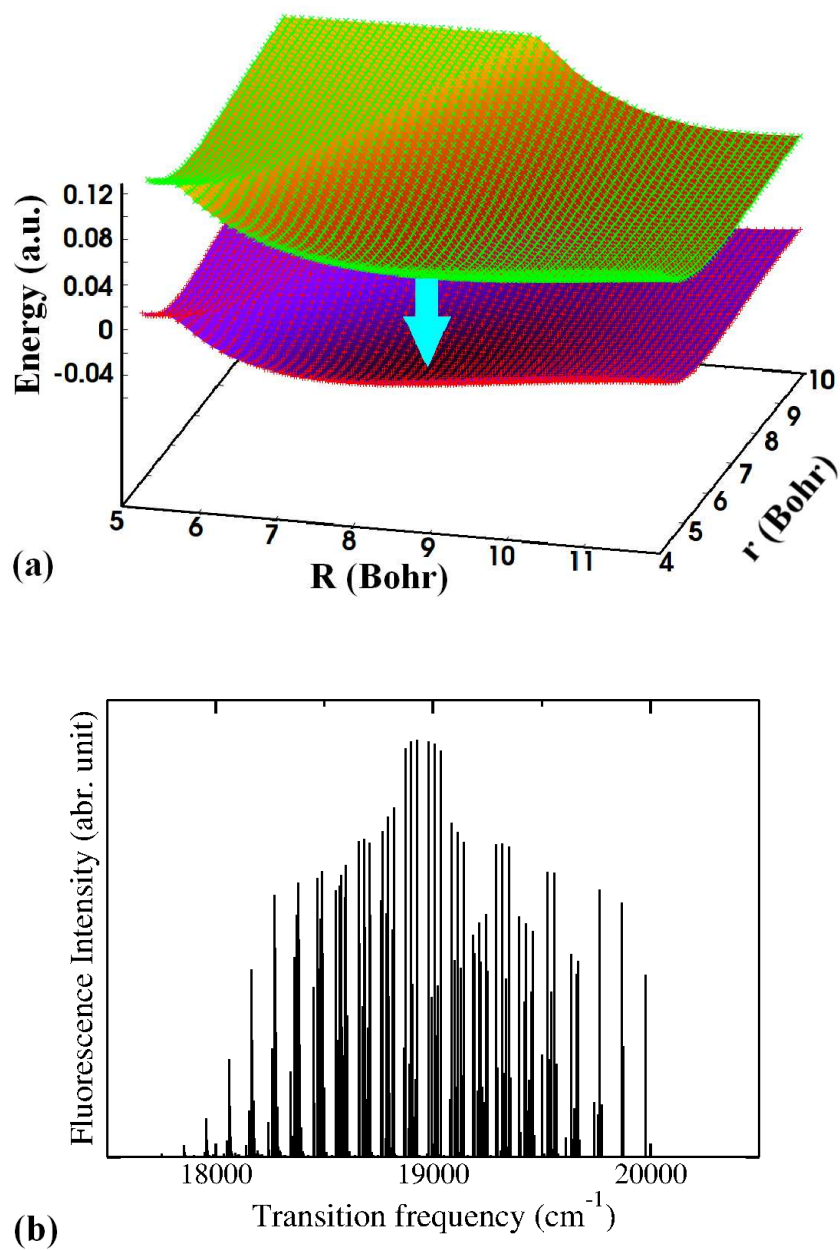
Figure 3.14: (a) A schematic illustration of two 2D PES. (b) Fluorescence lines associated with a typical spectrum of the system in (a). Image taken from Ref. [6]

energy shift between the ground and excited state PES. Similar to the ground state,

$$
\begin{aligned}
V_{\text{ex}}(r_1, r_2, r_3) &= V_1^e(r_1) + V_2^e(r_2) + V_3^e(r_3) \\
&+ V_{3b}(r_1, r_2, r_3) - E_{shift},
\end{aligned} \tag{3.50}
$$

where the $V_k^e(r_k)$ represent pairwise potential between atoms i and j, however we now use the Na_2 $B(^1\Pi_u)$ excited state potentials ([127]) for their expression. The three-body potential will be defined as

$$
V_{3b} = D_{3b} \; e^{\left[-\sum_k \left(r_k - r_k^{eq}\right)^2/\Delta R^2\right]}, \tag{3.51}
$$

where $D_{3b} = -0.02$ a.u., $r_3^{eq} = r_1^{eq} = 0.5 r_2^{eq} = 6$ Bohr, and $\Delta R = 8$ Bohr. And, the energy shift will be equal to $E_{shift} = E(Na_{3p}) - E(Na_{3s})$.

Fig. (3.14a) gives a schematic illustration of the two-dimensional PES as a function of the two internal coordinates. The simulated frequency-resolved spectrum between rovibrational eigenstates of these two surfaces is shown in Fig. (3.14b). With our objective being to determine the excited state potential from the intensity fluorescence data, we follow our inversion procedure, and first make an initial guess for the excited state potential. For this we use a sum of Morse potentials,

$$
V_k^M = D_k^e \left[\exp(-\beta_k(r_k - r_k^{eq})) - 1\right]^2 + T_k^e. \tag{3.52}
$$

where, as before, we can estimate the Morse parameters D_k^e, T_k^e, r_k^{eq} and β_k using lower transition frequencies, $\omega_{i,s}$, to some, say $i = 1$, ground vibrational level, we hope to roughly estimate V_{ex} about its minimum position (R^{eq}, r^{eq}), as

$$
V_{ex} \approx V_1^M(r_1) + V_2^M(r_2) + V_3^M(r_3) - E_{shift} \; . \tag{3.53}
$$

And as before, the distribution of $|d_{i=1,s}|^2$ for the low lying excited ϕ_s states can be used to estimate r_k^{eq}.

This approximation for V_{ex} now allows for an initial estimate of the (unknown) signs of the transition dipole matrix elements, $d_{i,s}$, using Eq. (3.13) (recall that the magnitudes of the real bound-bound matrix elements) are already known from experiment). Then, using Eq. (3.21) including only a few low-lying rovibrational excited states, a new estimate of $V_{\text{ex}}(R, r)$ about (R^{eq}, r^{eq}) can be calculated. Iterating this procedure until convergence, and then extrapolating the potential in both R and r

directions allows for the entire surface of the electronic excited state to be generated. We show the results of the extraction in Fig. (3.15) against the "true" PES. The
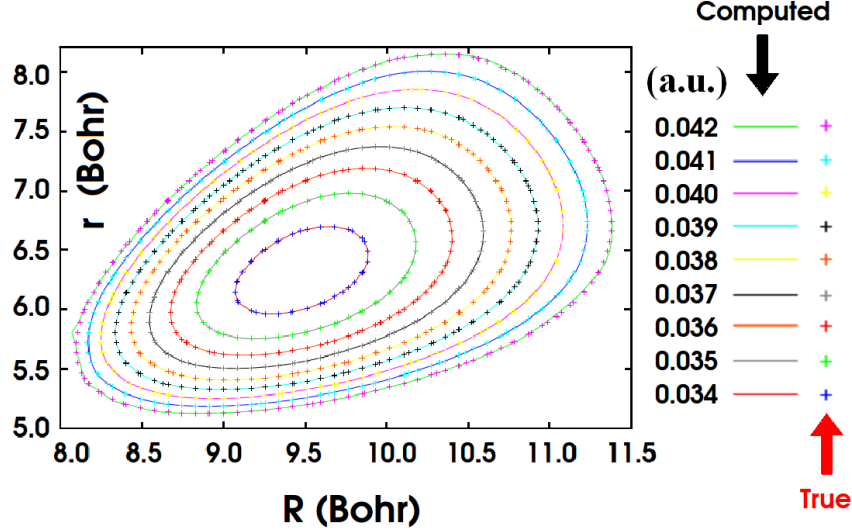
Figure 3.15: A comparison between a PES extracted using Eq. (3.21), using only the $s = 1 - 10$ states, with $E(s = 10) = 3.602 \times 10^{-2}$ a.u. (full lines), and the "true" PES (points). Image taken from Ref. [6]

calculated potential, which used the ten lowest rovibrational states in the excited potential, required 335 of the low lying ground vibrational states We find excellent agreement between the two surfaces, with average RMS errors of approximately 0.01 cm^{-1}. (see Ref. [6] for more details of the results).

The two dimensional inversion approach also works for more complicated excited state potentials, V_{ex}, such as those possessing multiple minima. Using the same excited state PES as earlier (Eq. (3.50)), we can add an additional three body term, V'_{3b}, with parameters given by $D'_{3b} = -0.003$ a.u., $r_3^{eq} = r_1^{eq} = 0.5 r_2^{eq} = 7.2$ Bohr, and $\Delta R = 0.5$ Bohr, to generate a second local minima. Shown in Fig. (3.16a) is this "true" potential compared with the results of the extraction using excited rovibrational levels $s = 1 - 6$. First, we see that the results match very well, with RMS errors below 0.1 cm^{-1} (see Ref. [6] for more details). However, it is important to note that the energy level of the highest rovibrational state, $E(s = 6) = 0.03539$ a.u., is in fact *lower* than the energy of the local minimum (0.03554 a.u.). Thus the ability to resolve the second local minima occurs solely due to the information contained in the classically-forbidden region of the vibrational wavefunctions. In
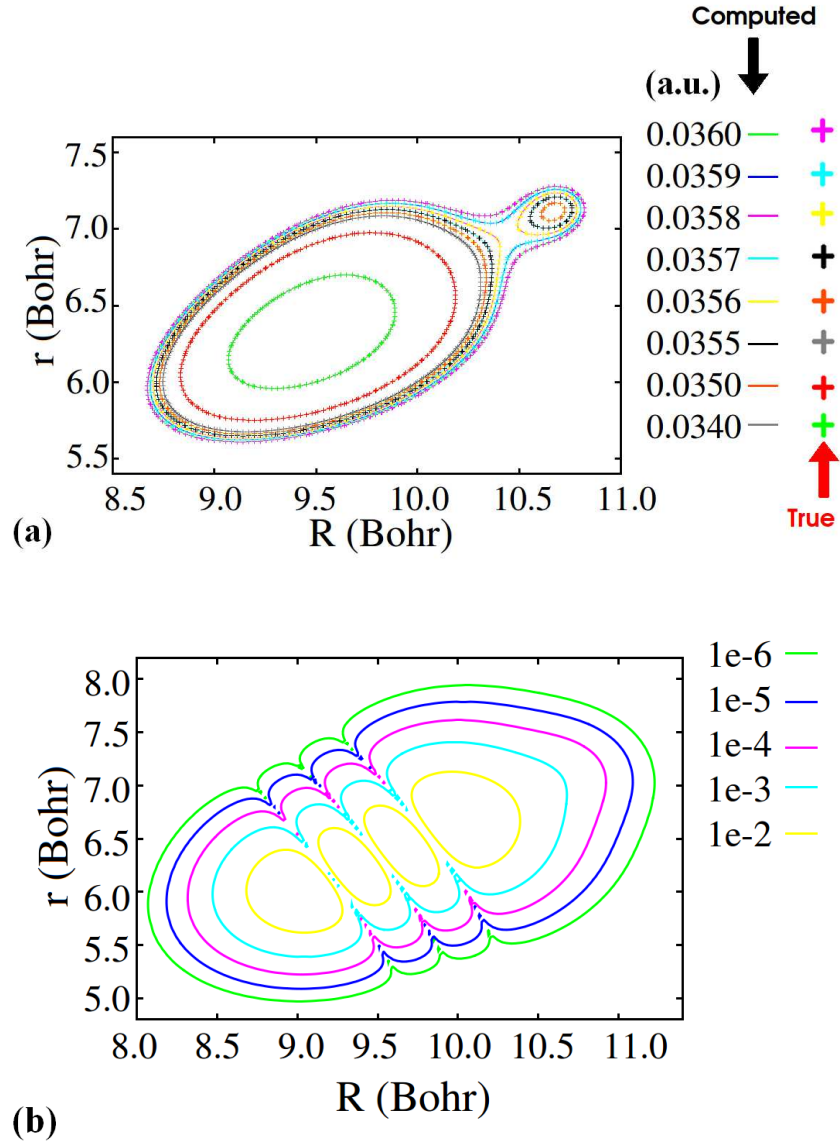
Figure 3.16: Extraction of a double-well PES: (a) A comparison between the PES extracted using Eq. (3.21) (full lines), and the "true" PES (points), having used only the $s = 1 - 6$ states, with $E(s = 6) = 3.54 \times 10^{-2}$ a.u.; (b) $|\phi_6(R, r)|^2$ - the probability-density for the highest state used.

Fig. (3.16b), we plot the probability-density associated with the highest energetic state ($s = 6$) used in the extraction. This illustrates that the tunneling tails of the vibrational wave functions spread across the molecular space and allows for the accurate determination of the PES well beyond the classical allowed region. Finally, out of the 4800 possible emission lines of non-negligible strengths which could have been used, only one fourth were included in the calculation. As we have encountered earlier, weak transitions lines, particularly those with large uncertainties [143, 144] can be removed from the computation without detrimental effects.

This inversions of a two-dimensional excited state PES from emission (or absorption) line positions and intensities opens up the door to extracting more complicated structures, such as three-dimensional PES and those of nonlinear molecules. Also, similar to the diatomic case [143, 144], given knowledge of the excited PES, it will be of great interest to determine (the $\mathbf{R}$ coordinate dependence of) the electronic transition dipole function. Having the transition dipole function, then permits us to move beyond the Franck-Condon approximation (FCA) to obtain a more accurate solution to the PES.

3.7.2 Dipole Correction Extension

As we have shown in this chapter, we are able to extract excited state electronic potentials and the nuclear coordinate dependence of the transition dipole function from spectroscopic data by using the Franck-Condon approximation (FCA). However, for many situations [141, 142], the FCA may not be justified because there could be a substantial variation in the dipole function across the region spanned by the potential. In Sec. 3.2.3, we briefly suggested an approach for extending our inversion procedure beyond the FCA. Here, we review the work of collaborators (see Ref. [7]) which continued on this idea and gives the specific accuracy improvements. It should be noted that this technique is applicable to any other inversion schemes which are based on the FCA (*e.g.* method of Avisar and Tannor [153, 154]).

In the following presentation, we also further address an inherent limitation often found in experimental data, namely, that not all of the desired data is available. In particular, it can be easier to label transition lines in a spectrum to/from low-lying states and highly-excited states [33]. Thus, in the case when no information is available for the majority of the intermediate states of an PES, inversion methods such as RKR are not possible. However, as we demonstrate below by using the Q-branch transitions from only a few low-lying states ($s = 0 - 5$) and some highly-

excited states ($s = 20 - 23$) with large rotational constants ($J' = 44$), our approach is still capable of obtaining great results.

Na$_2$ A State
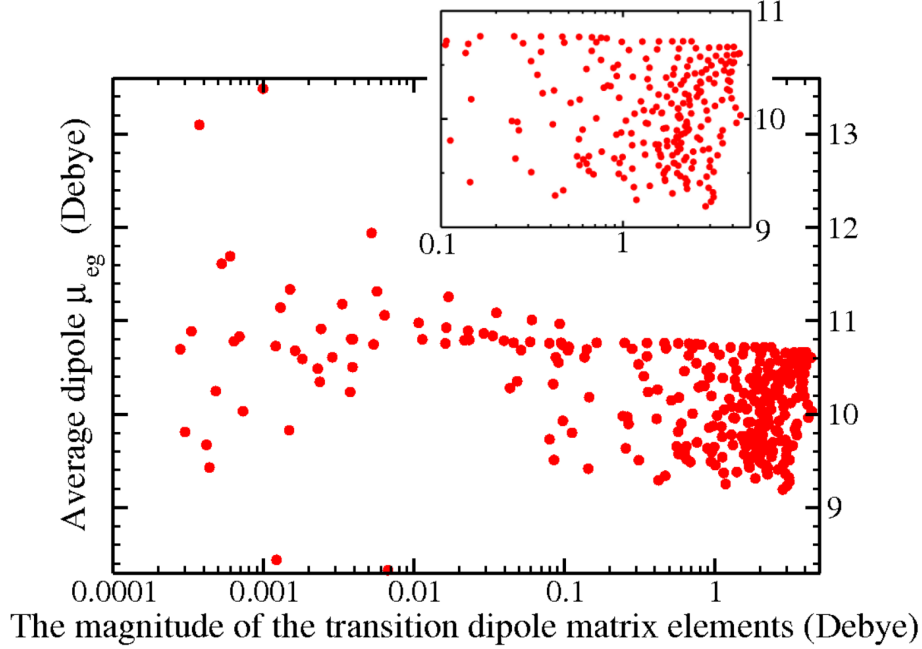
Figure 3.17: The average transition dipole moment $\bar{\mu}_{e,g}$ of Eq. (3.13) for transitions from $|s = 0 - 10, J' = 45, \text{A } ^1\Sigma_u\rangle$ to the $|i = 0 - 54, J' = 44, \text{X } ^1\Sigma_g\rangle$ states as a function of the transition magnitude, $|d_{i,s}|$. Figure and caption taken from Ref. [7].

As mentioned, the accuracy of the inverted potential using Eq. (3.21) and the transition dipole function using Eq. (3.24) is limited by the validity of the FCA. In order to test this assumption, we would like to look at the true variation of the average dipole, $\bar{\mu}_{e,g}$, for different vibrational quantum numbers of the ground (g), and excited (e) state potentials. Using the $|\nu = 0 - 10, J' = 45, \text{A } ^1\Sigma_u\rangle$ to $|\nu = 0 - 54, J' = 44, \text{X } ^1\Sigma_g\rangle$ transitions in Na$_2$, we plot, in Fig. 3.17, $\bar{\mu}_{e,g}$ as a function of the transition magnitudes, $|d_{i,s}|$. Instead of these plotted points for $\bar{\mu}_{e,g}$ falling on a horizontal line (as would be the case when FCA is valid), we find a standard deviation of the points from the average value of the dipole is $\sim 6.6\%$. To take this variation into account, our objective will be to use the information of the

$\mu_{e,g}(R)$ function derived in Eq. (3.24) to improve our inversion method.

By rearranging Eq. 3.13, we can get an expression for the excited state rovibrational eigenstates

$$\phi_s(R) = \frac{\sum_i \chi_i(R) d_{i,s}}{\mu_{e,g}(R)}, \tag{3.54}$$

in terms of the ground rovibrational states, $\chi_i(R)$, the TDMe, $d_{i,s}$, and the transition dipole function, $\mu_{e,g}(R)$. These eigenstates can then be used to recompute the overlap integrals with the ground states as follows

$$f_{i,s} \equiv \langle \chi_i \mid \phi_s \rangle = \int dR \frac{\sum_j \chi_j(R) d_{j,s} \chi_i(R)}{\mu_{e,g}(R)}. \tag{3.55}$$

Then these new values allow for us to write the potential inversion formula without employing the FCA as

$$V_{\text{ex}}(R) = \frac{\sum_s \sum_{i,j} f_{i,s}^* f_{j,s} \omega_{i,s} \chi_i^*(R) \chi_j(R)}{\sum_s |\sum_i \chi_i(R) f_{i,s}|^2} + V_g(R). \tag{3.56}$$

Now we have a dipole correction method to Eq. (3.21) which proceeds in the following manner:

1. Compute $V_{\text{ex}}(R)$ and $\mu_{e,g}(R)$ using our original approach within the FCA

2. Compute the lowest eigenfunction $\phi_{s=0}(R)$ of $V_{\text{ex}}(R)$ and use Eq. (3.13) improve $\mu_{e,g}(R)$.

3. Use the improved $\mu_{e,g}(R)$ and Eq. (3.55) to improve the $f_{i,s}$ overlap integrals for $s = 0, 1$.

4. Finally, use the overlap integrals and Eq. (3.56) to improve the inverted potential, $V_{\text{ex}}(R)$.

5. Iterate steps 2–4 for an increasing number of the excited states (e.g. $s = 0, 1$), until all available excited rovibrational states, ϕ_s have been included.

Notice, that this iterative process uses both the intensities and frequencies of the experimental data to improve the potential and the transition dipole function simultaneously.

The success of this approach is demonstrated with corrections to the extracted $A(^1\Sigma_u^+)$ excited state potential of Na_2 using fluorescence data to the ground $X(^1\Sigma_g^+)$

state. Note that we use *ab initio* potentials and transition dipole functions of Schmidt et al.[127] to simulate the experimental fluorescence data. In particular, we use the rovibrational state $s = [0-10]$ and $i = [0-54]$, in the $J' = 45 \rightarrow J'' = 44$ P-branch, where s and i label the excited and ground states respectively. In Fig. 3.18a, we plot the difference between the computed and the true potentials as a function of the internuclear distance for our original procedure and after using the dipole correction method. It can clearly be seen that going beyond the FCA improves the accuracy of the extracted $A(^1\Sigma_u^+)$ potential by up to a factor of 20. As expected the determination of the transition dipole function is improved by a similar factor, as shown in Fig. 3.18b.

Unlike our previous FCA-based inversion schemes [143, 144], this study iteratively improves the signs and magnitudes of the overlap integrals, $f_{i,s}$, instead of only finding the signs of the transition dipole matrix elements. This occurs as a result of iteratively obtaining more and more accurate representations of the excited rovibrational eigenstates due to utilizing the transition dipole function. We demonstrated this in Fig. 3.19a and Fig. 3.19b, where we plot the errors in the extracted wave functions, $\phi_{s=0}(R)$ and $\phi_{s=5}(R)$, as a function of the radial distance, R, for the two cases (with and without FCA). And, as anticipated a factor of 10 improvement is seen in the wavefunction accuracy.

Na$_2$ B State

We now demonstrate how the dipole correction procedure improves the inversion results even when limited spectroscopic data is available. Using the excited B $^1\Pi_u$ electronic potential of Na$_2$, we consider only the Q branch transitions ($J' = 44 \rightarrow J'' = 44$) between the rovibrational states in the $X^1\Sigma_g^+$ state and the six low-lying states ($s = 0-5$) and the four most highly-excited states ($s = 20-23$) of the B state. In Fig. 3.20 we see the same results as earlier, the differences between the computed and the true potential (a) and transition dipole function (b) as a function of the internuclear distance is improved by a factor of 10-20 when performing the dipole correction. Similar to before, we obtain a global RMS error of 0.08 cm^{-1} over an energy range of 2300 cm^{-1}, and an RMS error about the minimum of 0.02 cm^{-1}, using only 10 rovibrational states of the B potential.

As with our original formulation, the accuracy of the inversion is reliant on the degree with which we satisfy the completeness condition. Namely, how well can the excited rovibrational wave functions, ϕ_s, be expressed as a linear combination of the
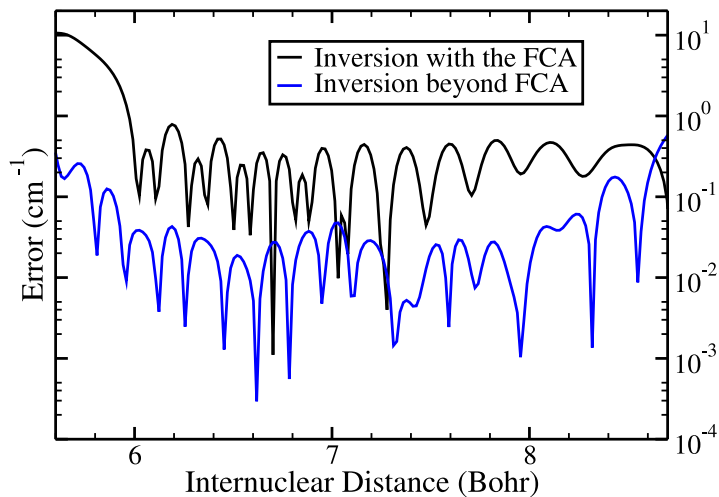
(a)
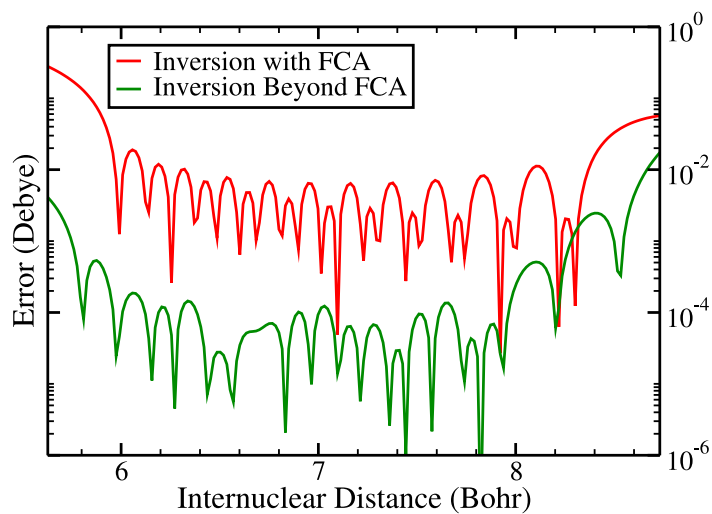
(b)

Figure 3.18: A comparison of the "dipole correction" and the FCA-based inversions of the Na$_2$ A $^1\Sigma_u^+$ potential and the A $^1\Sigma_u^+ \rightarrow$ X$^1\Sigma_g^+$ electronic transition function. (a) Differences (in cm^{-1}) between the inverted and the true potential; (b) Differences (in Debye) between the inverted and the true electronic transition dipole function. Figure and caption taken from Ref. [7].

(a)

(b)
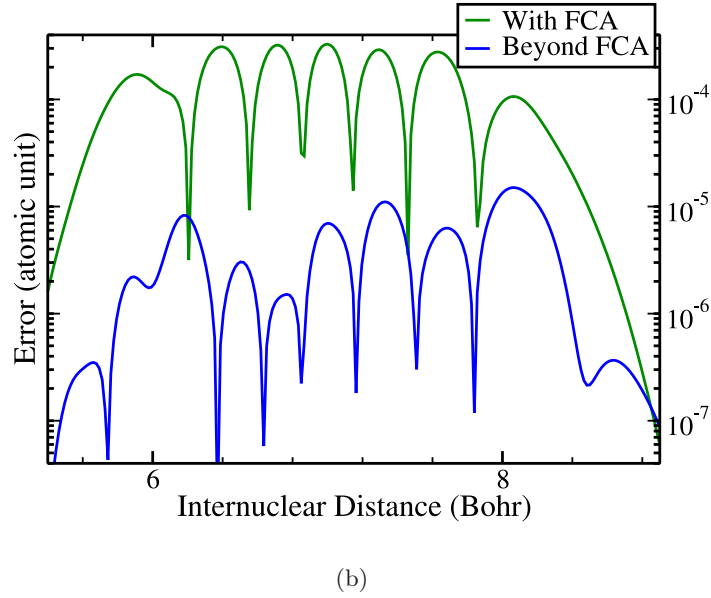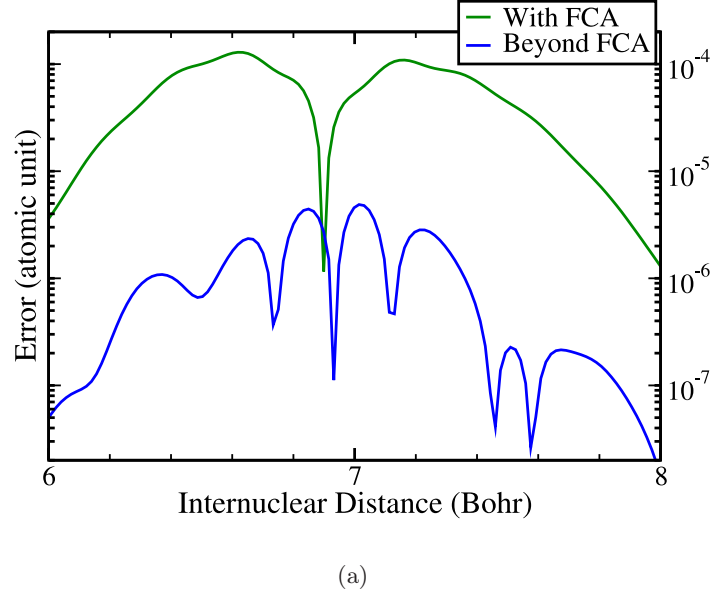
Figure 3.19: A comparison between the accuracies of the computed vibrational wave functions as derived by the FCA-based inversion and the "dipole correction" inversion for (a) $\phi_{s=0}(R)$ and (b) $\phi_{s=5}(R)$. Figure and caption taken from Ref. [7].
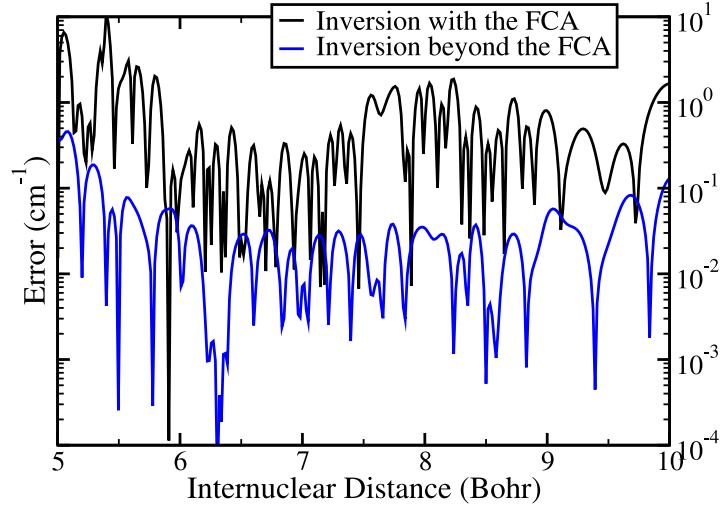
(a)
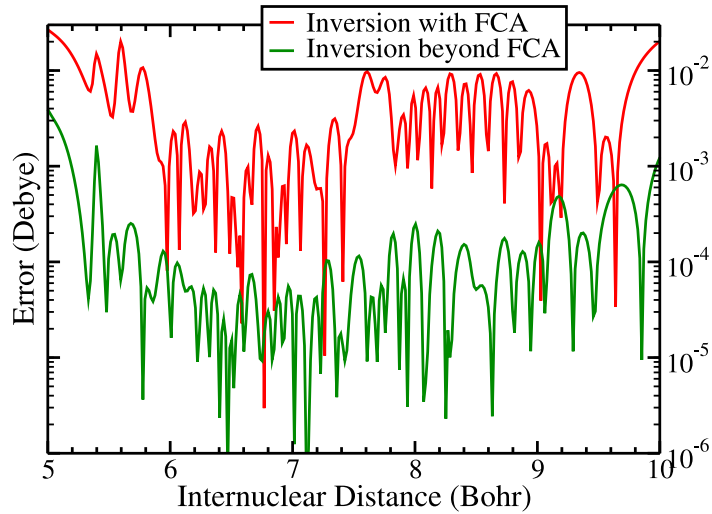
(b)

Figure 3.20: A comparison between the "dipole correction" and FCA-based inversions of the Na$_2$ B $^1\Pi_u$ potential and the B $^1\Pi_u \rightarrow$ X$^1\Sigma_g^+$ transition dipole function. (a) Differences (in cm^{-1}) between the inverted and the true potential; (b) Differences (in Debye) between the inverted and the true electronic transition dipole function. Figure and caption taken from Ref. [7].

ground vibrational states, χ_i. To this end, it may be necessary to include continuum states to satisfy completeness [155], a point which has already been address in Sec. 3.4 (and Ref. [128]).

3.8 Summary

We have presented a way of solving the "spectroscopic phase", namely the extraction of the signs of transition-dipole matrix elements from their measured absolute-squared values. We have shown that given the transition-dipole amplitudes it is possible to generate the excited state potential(s) and transition dipole moment(s) within (to global RMS error of 0.11 cm^1) and beyond ($0.03 - 0.1$ cm^{-1}) the FC approximation. This implies that line positions can, in general, be calculated to within 0.01 cm^{-1}. The procedure, which was demonstrated numerically for the diatomic (Na$_2$) case, is in principle valid for any polyatomic molecule. It has been shown that the inversion formula, as well as the procedure, works for a modeled two-dimensional potential [6].

One strong requirement of our approach is the ability to correctly assign the spectral lines to the right pair of ground and excited state eigenvalues. Otherwise, the fundamental inversion equation (Eq. (3.21)) which includes a double summation over the frequencies and transition dipole moments between particular ground and excited eigenstate doesn't make sense. Fortunately, not all lines need to be assigned. As we have shown, only a few excited eigenstates are necessary to extract the full potential curve. A more critical restriction is that those excited states included in the calculation can be nicely expanded in the GS basis (*e.g.* that the completeness condition is fulfilled). This is because the errors in the potential will grow quadratically with errors in the completeness condition (see Eq. (3.21)). Therefore, our procedure works best when the electronic GS spans a similar or greater radial range that the electronic excited state. For instance, it is preferable for the long range behavior of the GS to be $\frac{C^3}{R^3}$ and that of the excited state to be $\frac{C^6}{R^6}$ rather than *vice versa*. However, one advantage to this summation over transition dipole moments (TDMs) in the basis set expansion is the robustness of our procedure to random errors in the spectroscopic data. We have shown that we can achieve great results with even 10 % random errors in the transition magnitudes, and we attribute this to the summation averaging over the random fluctuations. Though in the general case, the tolerable size of these random errors is difficult to define since it depends

on the system's characteristics such as the number of GS levels included in the basis set. One should note that any GS eigenstates having weak TDMs to an excited state included in the calculation can be omitted in the expansion (and thus does not require assignment). Lastly, although we haven't explicitly proven that our method will converge to a unique solution, we expect this to be the case due to the uniqueness of the expanded excited eigenstates and knowledge of their eigenvalues, which together with a Hamiltonian of a given form fully specifies the potential term.

3.8.1 A Brief Comparison

Where our method excels over other approaches is in cases when the excited state potential is not well represented by a standard model or when only a few energy levels are known (but most of their TDMs have been resolved).

RKR methods perform well for heavier molecules where the WKB approximation is most valid, and when the PES is low dimensional and simple in form. It is known to break down for irregularly shaped PESs, such as those with a "barrier", "shelf" or multiple minima. RKR results are given in tabular form and defined only for regions of the PES covered by the spectroscopic data. Moreover, the RKR approach doesn't provide any information in how to extrapolate beyond regions lacking experimental data. Determining all the energy levels can be a cumbersome task which requires a relatively large number of empirical molecular constants with most of them having little physical significance.

DPF approaches require a well-behaved analytical potential model that can be used in the fitting procedure. Poorly chosen functions result in nonphysical behavior occurring in either the short-range or long-range regions. To accurately describe non-standard potential curves with irregular portions, higher order polynomials must be used, which leads to greater difficultly in converging the results. This high degree of parametrization, which is also necessary as the dimensionality of the system increases, tends to become very computationally expensive. In contrast, our inversion procedure performs equally well for irregularly shaped potentials, and scales much better for multidimensional cases. Our results typically converge for each iteration in the construction after a few cycles, independent of the potential form or dimensionality. Thus we require far fewer time-consuming diagonalizations of the system before converging.

Ab-initio quantum chemistry calculations which have begun to yield reasonable results for small molecular systems, are limited in their availability and are difficult

to implement individually for a case of interest. Also, they tend to struggle either at short or large interatomic distances due to the balance between accounting for the electron exchange and charge overlap at short ranges, and the effects of weak long-range forces which should be treated perturbatively. These calculation become greatly complicated as the number of atoms in polyatomic molecules increases and require significant computer resources. In contrast, our procedure is simple to implement and can reproduce equally accurate results at all ranges of the potential, given that the excited states can be well described in the ground state basis. The computational time for the FCA approach is estimated to scale as $N_b \times t_{\text{diag}}$, where N_b is the total number of excited rovibrational states used in Eq. [3.47], and t_{diag} is the time required to calculate the eigenstates from the constructed PES. The dipole correction method requires additional effort which is estimated to scale as $N_b \times N_b/2 \times t_{\text{diag}}$. Thus, for the one dimensional diatomic case, where the value of t_{diag} is on the order of seconds, the required computational time is rather short. For multi-dimensional case, past work (see Ref. [38]) involving the realistic calculation of several hundred eigenstates, has required computational times on the order of hours, making the inversion process more expensive, yet more efficient than other approaches which require a greater number of diagonalizations.

Chapter 4

Molecular Wavefunction Imaging

4.1 Introduction

As the field of quantum information processing progresses into the experimental domain, it becomes increasingly necessary to develop techniques for the non-destructive detection and reconstruction of (complex) wave functions. Such reconstruction is needed for the verification of the initial preparation; the detection of errors due to decoherence and noise; the determination of the fidelity of the logical operations and for the read-out of the final state. In the last few years, molecules have emerged as promising media for large-scale quantum computations, partly due to the existence of strong dipole-dipole interactions that serve as a resource for two-qubit operations [156–161]. A number of theoretical and experimental publications demonstrating feasible read/write operations [75, 162–166] and logic gates [167–173] have been published, with the read-out amounting to the retrieval of both the amplitude and the phase of a molecular wave packet [125, 174–177]. There have been several techniques for imaging molecular wave packets, each with their own drawbacks, already suggested.

4.1.1 Quantum State Tomography

One such technique based on quantum state tomography, [75, 174, 175, 178] which has been mainly applied to photonic states, uses a sequence of identical measurements within a series of different bases to completely reconstruct the quantum wavefunction.

Developed by Walmsley [8], molecular emission tomography measures the spectrum of fluorescence from a molecule at many different times for many different orientations of the phase space coordinates. For an excited vibrational wavepacket, this measurement obtains a quasi-probability distribution of the vibrational mode of a molecule.
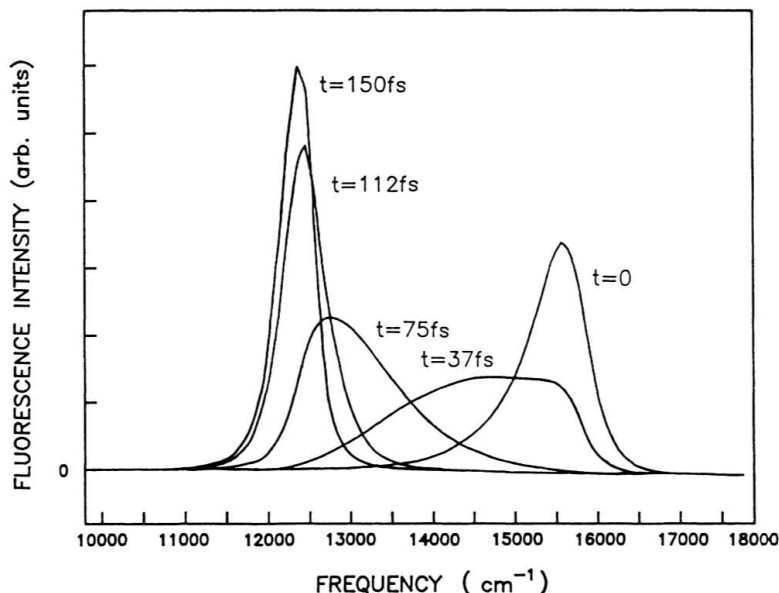
Figure 4.1: Gating fluorescence of an excited vibrational wavepacket in Na$_2$ for the gate positions $t = O$, 37, 75, 112, and 150 fs relatively to the pump pulse. Taken from Ref. [8]

In Fig. (4.1), the spectra of the gated fluorescence, calculated using the up-conversion technique (Sec. (2.4.2)), is shown for an excited wavepacket in Na$_2$ [8]. Semi-classically we would expect that a molecule will emit a photon at time T of energy equal to the difference between potential energy at an internuclear distance, $R(T)$, of the position of the initial wavepacket and the final electronic state. Thus, as the wavepacket oscillates in the potential, the fluorescence intensity as a function of wavelength should change correspondingly in time. Assuming, for a molecular ensemble, that the total fluorescence intensity is constant in time (*i.e* the Franck-Condon approximation where value of the transition dipole moment is constant), then the results of Fig. (4.1) should be a good representation of the shape of the wavepacket as a function of internuclear distance at different times. As can be seen, the wavepacket only samples a small range of difference potential when near the turning points leading to the narrow spectrum. Whereas, when the the wavepacket has a higher velocity it traverses over a wider range of potential energies causing the broader spectrum. By assuming that the wave packet propagates in a harmonic potential it is possible to use these probability distributions to generate the Wigner function of the state of the molecule [174]. Unfortunately, molecular imaging tomog-

raphy requires a very large number of measurements, such as different phase-space orientations, and is restricted to working well only in the harmonic approximation.

4.1.2 Algebraic-Inversion

Another technique [125, 176, 177] involves the (algebraic) inversion of the time-dependent fluorescence intensity. It is also possible[125, 126] to reconstruct an unknown excited state $\Psi(\mathbf{R}, t)$ by assuming that it can be expanded in terms of N of the excited vibrational eigenstates,

$$\Psi(\mathbf{R}, t) = \sum_{s=1}^{N} a_s \phi_s(\mathbf{R}) \exp(-iE_s t),$$

using the fluorescence signal $F(t)$, given[125, 126] as,

$$F(t) = \sum_{i} \sum_{s,s'} \left(\omega_{i,s} \omega_{i,s'} \right)^{\frac{3}{2}} d_{s,i} d_{i,s'} a_s^* a_{s'} e^{-i(E_s - E_{s'})t},$$

provided we know the $d_{i,s}$ amplitudes (including their signs). According to Eq. (3.21) this knowledge is enough to determine $V_{\text{ex}}(\mathbf{R})$, which in turn determines ϕ_s. The expansion coefficients a_s can then be determined by "strobing" the fluorescence at $N(N-1)/2$ time points and solving a set of quadratic[125, 126] or linear, "holographic"[179], equations. Under conditions pertinent to most electronic transitions, namely, when the Franck-Condon approximation is justified, the previous procedure of extracting the dipole moment phases [126] did not work well. The main limitation of this method is that the conversion of the bi-linear $a_{s'}^* a_s$ products to individual a_s coefficients is very sensitive to experimental errors.

4.1.3 Interferometric Approaches

This inordinate sensitivity to experimental errors can be overcome by linearizing the problem, as done in the "quantum state holography" method [179, 180] and other linear interferometric approaches [165, 166, 181–183]. However, these linear wave-packet interferometry (WPI) techniques encounter limitations related to evolving the target and reference wave packets on similar potential energy surfaces (PES) [184]. In addition, they are insensitive to any target probability amplitudes resulting from nonlinear excitation process involving eigenstates with small Frank-Condon factors to the initial states [184]. Using a non-linear WPI approach [185, 186], Cina and

Humble proposed a remedy to these problems and a resolution to the hindrance of linear-WPI methods associated with the reconstruction of unknown target wave packets on ill-characterized high-lying potentials. Their approach is based on using a pair of phase-related pulse pairs which produce a signal that is quadrilinear in the incident field amplitudes. Though, success of their approach relies on the existence, and detailed information, of an auxiliary intermediate electronic state used for the propagation of the reference wave packet. Moreover, it is not clear how uncertainties in this reference wave packet affect the fidelity of their reconstruction. Thus, we find that hampering all wave-packet interferometry (WPI) approaches remains the necessity, and accurate characterization, of some reference electronic state.

4.1.4 CARS Imaging

Correlation functions and/or wave-packet overlaps have also been accessed without the need of reference wave packets, instead through the use of Coherent Anti-Stokes Raman Scattering (CARS) spectroscopy [153, 154, 187–190].

The CARS process is a third-order nonlinear optical process involving three laser beams which interact with molecular (vibrational) states in much the same way as in Raman spectroscopy. However, unlike Raman whose signal relies on a spontaneous transition, CARS provides a coherently driven transition giving rise to a signal that is quadratically stronger and can be collected much faster in practical situations ($\sim 10^5$) than that of Raman transitions. Moreover, because CARS uses two laser frequencies to interact resonantly with a specific molecular vibration the signal is relatively high frequency (thus minimal fluorescence interference) and provides better resolutions. A good review of CARS can be found in Ref. [191].

Milner *et. al.* [192, 193] developed a technique for characterizing the molecular vibrations of polyatomic molecules by performing a cross-correlation frequency resolved optical gating (XFROG) of the CARS signal. XFROG is an extension, based off the original FROG method of Trebino [194], which was initial designed for the complete temporal and spectral characterization of ultrashort laser pulses. The procedure measures the cross-correlation between a known and unknown electric field by focusing the two (pulses) together in a nonlinear medium. The spectrum of the nonlinear signal, which manifest itself as nonresonant sum frequency generation in a non-linear crystal, is then measured with a spectrometer for many delay points. Using the data from both the frequency and time domains, XFROG is capable of providing accurate spectral intensity and phase retrieval of the unknown electric field.

The combined XFROG CARS approach thus allows for the extraction of the amplitude and phase information of molecular vibrations in a iterative process. However, the technique has only been demonstrated from ground electronic state vibrations, and is sensitive to one-photon resonances effecting the reference field.

Recently, Avisar and Tannor [153, 154, 190] have also applied a CARS scheme to imaging multi-dimensional wave packets. In their approach the first of the CARS pulses acts as the excitation field, creating wavepacket in an excited PES. Then, the second pulse dumps the population back into the ground state, before the third pulse returns that population to the excited state again. By performing a Fourier transform along the time delay of the second field, the excited wave packet's cross-correlation function with the vibrational eigenfunction of the ground state PES can be related to the third order polarization given as the CARS signal. Since their relations involves a direct correspondence with elements of the raw CARS signal, significant discrepancies arises once reasonable errors are included in the experimentally data [195]. In addition, their method has so far been applied only to the special case of a $\delta(t - t_0)$ pulse, where the wavepacket $\Psi(\mathsf{r}, t_0)$ is known at t_0 as being a simple replica of the ground energy eigenstate, $\chi_g(\mathsf{r})$. This is only reasonable once a large number of excited states have been included, which is at odds with the solution they provide to the unknown phase problem of the dipole matrix elements that requires exponential time with the number of states.

4.1.5   Kinetic Energy Distribution and Coulomb Explosion

Lastly, kinetic energy distributions of nuclei and photo-electrons or coulomb explosion [196–200] techniques provide a good basis for wave function reconstruction [201, 202]. These methods are however destructive, as they involve the ionization and/or the break-up of molecules.

4.1.6   Preamble

In many approaches the stumbling block appears to be the extraction of the *phases* of the relevant (e.g. fluorescence, photo-absorption) amplitudes. This problem is also related to the reconstruction of unknown time-evolving quantum states [125, 126, 179, 184–186, 203]. Given that such states can be prepared (e.g., by photo-excitation with an ultrashort pulse of light) in multiplicity of replicas, then the relatively tiny fraction of the replicas that manage to fluoresce during the 100fsec-1psec time scales

of interest ought to yield information about the state of the majority of the (non-fluorescing) replicas in an essentially quantum-non-demolition manner. Tomographic methods that have been tried [8, 75, 204] appear to be inaccurate far from the harmonic limit. Again, the crux to such state reconstruction is the extraction of the phases of the fundamental transition-dipole amplitudes that mediate the information from the few fluorescing replicas of the unknown state to the observer.

We describe a method that extracts the excited wave packet amplitudes and phases from the time dependent intensity of fluorescence. The method works by taking a series of finite time Fourier transforms at the $(\omega_{s',s})$ beat frequencies of the data [48]. In this way one performs a one-by-one extraction of the expansion coefficients of the unknown wave packet. The method requires no reference state, yet because of the relatively long time averaging, it is extremely robust and is much less sensitive to experimental errors compared to the other mentioned schemes. Our approach also avoid the application of the Franck-Condon approximation, which is a necessary assumption in nearly all tomographic, interferometric and CARS imaging proposals. In contrast to destructive methods, because, typically spontaneous emission lifetimes are relatively long ($10^{-8} - 10^{-6}$ seconds), only $10^{-6} - 10^{-5}$ of the excited molecules fluoresce over the 1 - 10 ps time span of interest, thus making fluorescence based methods essentially non-destructive over such short time spans.

In addition to molecular wave packet imaging, by using the well known perturbative regime connection between the field and the material expansion coefficients, our method (following a single calibration run), can be used to extract any electromagnetic (e.m.) field whose time dependent intensity function is known. The problem of extracting the phases of the e.m. fields has received much attention in recent years. There now exist a panoply of methods [205–208] which can be roughly categorized as *interferometric* [194, 209–211] and *non-interferometric* [212–215]. These methods which involve non-trivial non-linear mixing and iterative solutions of integral equations, work best for ultrashort laser pulses of large bandwidths. They do not work as well for relatively longer ($10^{-11} - 10^{-10}$ seconds) pulses of narrower bandwidths, where our method remains successful.

4.2   Theory

4.2.1   Imaging Method

We consider the short laser pulse excitation of $\chi_g(\mathsf{r})$, a rovibrational energy eigenstate belonging to the ground electronic state, where r is a (collective) nuclear coordinate, to form a wave packet $\Psi(\mathsf{r}, t)$ moving on an excited electronic state, given as

$$\Psi(\mathsf{r}, t) = \sum_s a_s \phi_s(\mathsf{r}) \exp(-iE_s t/\hbar - \gamma_s t/2). \tag{4.1}$$

In the above, $\phi_s(\mathsf{r})$ are the excited rovibrational eigenstates of energies E_s, a_s, are the expansion coefficients of Ψ in terms ϕ_s, and γ_s are the (spontaneous emission) decay rate of each ϕ_s state, which are expressed as [125]

$$\gamma_s = \sum_f A_{f,s} \tag{4.2}$$

where $A_{f,s}$ are Einstein A-coefficients, given, in atomic units, as

$$A_{f,s} = \frac{4\omega_{f,s}^3}{3c^3} |\mu_{f,s}|^2, \tag{4.3}$$

and $\mu_{f,s} \equiv \langle \chi_f | \mu | \phi_s \rangle$ are the dipole matrix elements between the electronically excited energy eigenstates, ϕ_s, and the ground energy eigenstates, χ_f.

We have shown in the past [6, 128, 143, 144] that knowledge of $|\mu_{f,s}|^2$, the magnitude-squared of the dipole matrix elements, which can be determined directly from the frequency-resolved fluorescence (absorption) spectrum, coupled with knowledge of the ground state potential to (from) which emission (absorption) occurs, enables the extraction of the phases of $\mu_{f,s}$. Thus, the only remaining unknowns are the amplitudes $|a_s|$ and phases δ_s of the a_s expansion coefficients. As shown below, these quantities can be extracted from the time-dependent fluorescence of $\Psi(t)$ into various rovibrational ground states.

Following Ref. [125] we write the rate of the time dependent fluorescence as

$$R(t) = \sum_{s,s'} a_s^* a_{s'} C_{s,s'} \exp(-i\omega_{s,s'} t - (\gamma_s + \gamma_{s'})t/2) \tag{4.4}$$

where $\omega_{s,s'}$ are "beat" frequencies [48], defined as, $\omega_{s,s'} = (E_s - E_{s'})/\hbar$, and $C_{s,s'}$ is

a time-independent molecular matrix, given as

$$C_{s,s'} = \frac{2}{3c^3} \sum_f (\omega_{f,s}^3 + \omega_{f,s'}^3) \langle \phi_s | \mu | \chi_f \rangle \langle \chi_f | \mu | \phi_{s'} \rangle. \tag{4.5}$$

Over typical short time scales of interest (e.g., ~ 1 ps) the decline in population due to fluorescence is negligible, allowing us to disregard γ_s. Writing a_s explicitly as $a_s = |a_s| \exp(i\delta_s)$ we obtain that

$$R(t) = \sum_{s,s'} C_{s,s'} |a_s||a_{s'}| \exp\left(i\omega_{s,s'}t + i\delta_{s,s'}\right) \tag{4.6}$$

where $\delta_{s,s'} = \delta_s - \delta'_s$. We now select a specific (s, s') component of the $R(t)$ signal by calculating at each beat frequency its "fFT" - the $\omega_{s,s'}$ Fourier integral calculated over long finite time T. The filtering method works because all the $\omega \neq \omega_{s,s'}$ components decay as $1/T$. Explicitly,

$$\frac{1}{T} \int_0^T dt R(t) \exp(-i\omega t) = \frac{1}{T} \int_0^T dt \sum_{s,s'} C_{s,s'} |a_s||a_{s'}| \exp(i\delta_{s,s'}) \exp(i(\omega_{s,s'} - \omega)t)$$

$$= \begin{cases} C_{s,s'} |a_s||a_{s'}| \exp(i\delta_{s,s'}), & \text{for } \omega_{s,s'} = \omega \\ i\frac{C_{s,s'} |a_s||a_{s'}| \exp(i\delta_{s,s'})}{(\omega_{s,s'}-\omega)T} \left(\exp[i(\omega_{s,s'} - \omega)T] - 1\right), & \text{for } \omega_{s,s'} \neq \omega. \end{cases} \tag{4.7}$$

Thus, by choosing sufficiently long integration times T, satisfying $T \gg 1/\min |\omega_{s,s'} - \omega|$ for $\omega_{s,s'} \neq \omega$, our method amplifies just one pre-chosen (s, s') beat term out of the $R(t)$ signal, while eliminating all others. The absolute value of each (s, s') term can be taken together with the knowledge of $C_{s,s'}$ to generate a set of equations containing products of the unknown amplitudes $|a_s||a_{s'}|$, which can then be solved, in the least-squares sense, to obtain the coefficient amplitudes $|a_s|$. Using Eq. (4.7) we determine $\delta_{s,s'}$ for all s and s', given which, we extract the individual state phases δ_s (up to an arbitrary overall phase). For diatomic vibrational spacings of ~ 1000 cm^{-1}, the integration time must be at least 1 ps to ensure a filtering accuracy of $\sim 1\%$. We find that the long integration times tend to wash out measurement errors in the time-dependent fluorescence, rendering the method, as we show in detail below, quite robust against such errors. Because most systems will be over-determined (having roughly $s^2/2$ equations for s unknowns), it is possible to increase the accuracy and reduce the integration time by using as many redundant equations as possible. In addition, by subtracting out of $R(t)$ the (s, s') terms whose values have already

been determined, we highlight the remaining (possibly weakly contributing) terms, thereby increasing their accuracy.

4.2.2 Electromagnetic Field Determination

Our ability to determine (the amplitude and phase of) excited state coefficients makes it possible to use the same setup to extract the excitation pulse's electric field. We again envision a molecule, initially in one of the electronically ground vibrational states χ_g, with energy E_g, being excited by an electric field

$$\vec{\varepsilon}(t) = \hat{\epsilon} \, \mathcal{R}_e \left\{ \mathcal{E}(t) \exp(-i\omega t) \right\} \tag{4.8}$$

where $\hat{\epsilon}$ is the polarization direction. Our aim here is to determine $\mathcal{E}(t)$ - the (complex) pulse envelope, and ω - the carrier frequency of the pulse. Provided that the Rabi angle $\theta = \int dt \Omega(t) << \pi$, where the Rabi frequency $\Omega(t) = \vec{\mu} \cdot \hat{\epsilon} \, \mathcal{E}(t)/\hbar$, the light-matter interaction can be treated perturbatively. Thus, a time-dependent wave packet will be created in the excited state as in Eq. (4.1) with excited state coefficients given by

$$a_s = 2\pi i f(\omega_{s,g}) \mu_{s,g}, \tag{4.9}$$

where $\mu_{s,g} = \langle \phi_s | \mu | \chi_g \rangle$ are the known dipole matrix elements between the ground χ_g and excited ϕ_s rovibrational states and $f(\omega_{s,g}) \equiv \int dt \mathcal{E}(t) \exp[i(\omega_{s,g} - \omega)t]$. Using the method of the previous section to determine the excited state coefficients a_s, we obtain the complex values of the frequency spectrum $f(\omega_{s,g})$ from Eq. (4.9) as,

$$f(\omega_{s,g}) = \frac{a_s}{2\pi i \mu_{s,g}}. \tag{4.10}$$

By tuning the pulse to excite multiple vibrational (or rotational) excited states, we have devised a complex-valued spectrometer with a resolution given by the spacing between energy levels. For pulses within the limit set by one over the sampling interval (up to several picosecond for rotational spacing) we can perform a discrete Fourier transform to obtain an image of its temporal profile. The bandwidth of the pulses must, of course, be restricted by the energy span of the optically accessible excited states.

4.3 Results

The wave packet imaging and pulse characterization techniques are demonstrated by performing numerical simulations on sodium dimer (Na_2) wave packets. We assume that a molecules, initially in the $X^1\Sigma_g^+$ ground rovibrational state ($v = 0; J = 0$) gets excited by a short laser pulse to a $J = 1$ wave packet of vibrational eigenstates belonging to the $A^1\Sigma_u^+$ electronic state. These states decay to either $J = 0$ or $J = 2$ (the P- and R-branches), generating fluorescence to all the vibrational states of $X^1\Sigma_g^+$ that enter the summation implicit in $C_{s,s'}$ of Eq. (4.5). Below we present the results for two types of (*"transform-limited"* and *"non-trivial linearly chirped"*) excitation pulses, omitting from the results excited states with populations $< 0.1\%$ because their effect on the fluorescence intensity is negligible.

4.3.1 Transform-Limited Pulse

We first consider the case in which a $50fs$ Gaussian pulse of $\sim 10^{12}$ W/cm^2 with carrier frequency of 15802 cm^{-1} excites the $v = (2 - 12); J = 1$ rovibrational states of the A state. The time-resolved fluorescence, shown in Fig. 4.2a, is generated by time-averaging the output of Eq. (4.4) over 70 fs intervals, providing a temporal resolution that has been experimentally demonstrated using both optical gating [75] and up-conversion [4, 5] techniques. In Fig. 4.2b, displaying two different times, $t = 0$ (red circles) and $t = 1ps$ (blue squares), we demonstrate that the imaged wave packet (solid lines) reproduces perfectly the "true" wave packet. Even when a random 10% Gaussian noise is introduced into the fluorescence data, the imaged wave packet is seen to coincide to better than 1% root-mean squared (rms) with the "true" one. This robustness is likely due to the averaging over by the long time integration of error-generated signal fluctuations.

Using Eq. (4.10) we can now deduce the frequency spectrum of the pulse at a discrete set of frequencies corresponding to the location of the absorption lines. Figure 4.2c exhibits excellent agreement between the "true" real part (blue circle), imaginary part (green squares) and absolute value (black bars) relative to the corresponding values of the imaged pulse. The displayed temporal pulse was generated from the discrete Fourier components as obtained by our method by performing discrete Fourier transforms at the discrete frequencies. Figure 4.2d shows the amplitude (solid line) and real part (dashed-line) of the result against that of the "true" electric field (red circles and green crosses, respectively).
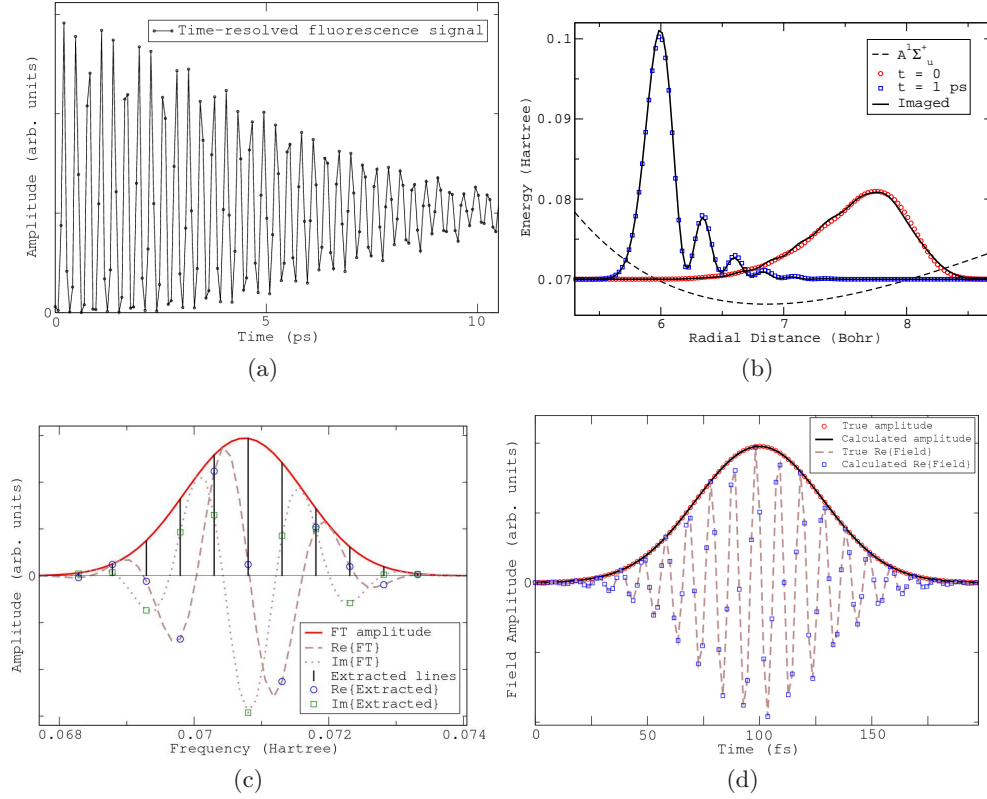
Figure 4.2: (a) Temporal fluorescence captured over 10 ps. (b) Actual and imaged excited state wave packets on $A^1\Sigma_u^+$ potential of Na_2 at t=0 and 1 ps. (c) Spectrum of the initial excitation pulse, showing absorption lines corresponding to the excited rovibrational eigenstates. (d) Temporal pulse profile of 50 fs width. The displayed real part of the electric field demonstrates good phase extraction.

4.3.2 Linearly-Chirped Pulse
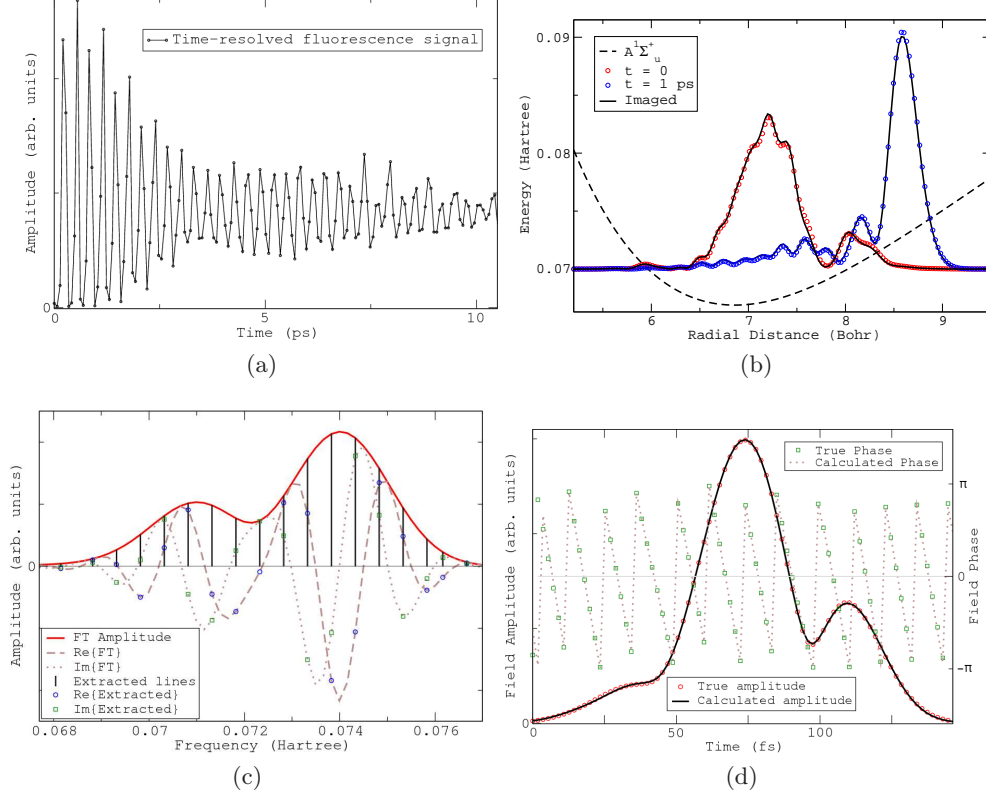
Figure 4.3: (a) Temporal fluorescence captured over 10 ps. (b) "True" (circles) and imaged (full lines) excited state wave packets moving on the $A^1\Sigma_u^+$ potential of Na_2 at $t = 0$ and $t = 1$ ps. (c) The spectrum of the initial excitation pulse, showing absorption lines corresponding to the excited rovibrational eigenstates. (d) Temporal pulse amplitude and the $-\pi$ and π phase of the field at each instant.

We have performed calculations similar to those of the previous section for linearly chirped pulses. The results are shown in Fig. 4.3d. The frequency profile, seen in Fig. 4.3c, has sufficient bandwidth to excite ~ 18 rovibrational states ($v = (2 - 19), J = 1$) with population $> 0.1\%$. We have computed the time-resolved fluorescence signal, adding 5% of random Gaussian noise to each time-averaged (~ 70 fs) data point, from which, using our method, we have extracted the excited state coefficients. The results of the wave packet imaging are found to be within 1% rms of the "true" values. Figure 4.3b compares the "true" (discrete points) wave function at the pulse center ($t = 0$) and at some later time ($t = 1$ ps), with the imaged values

(solid lines).

The $f(\omega_{s,g})$ discrete frequency components of the laser field, extracted from the a_s coefficients via Eq. (4.10), are displayed in Fig. 4.3c. The Fourier transform of these points gives us the temporal shape of the pulse. Figure 4.3d exhibits an excellent agreement between the "true" and imaged time dependent pulse amplitude and phase, correctly identifying the linear chirp of the field.

4.4 Summary

We have presented a method which reconstructs excited-state molecular wave packets (and e.m. field amplitudes) by selecting each beat component of the fluorescence signal using finite-time Fourier transforms calculated at each beat frequency. The procedure requires a pre-calibration involving the frequency resolved spectrum from which we extract the relevant dipole matrix elements to the final states. The integrating time over the temporal fluorescence is bound between two limits: It must be longer than the inverse of the energy splitting between adjacent vibrational states ($\sim 50fs$); and it must be shorter than the average decay time of the rovibrational levels ($\sim 10ns$). Within this range our method exhibits impressive robustness to random errors in the experimental signal.

Using the acquired knowledge of the excited coefficients to characterize the excitation pulse is a novel approach especially suitable for femtosecond pulses. Contrary to currently available methods, the experimental procedure and mathematical analysis needed to reconstruct the pulse is simple and straightforward.

Chapter 5

Extraction of Transition Dipole Moments

5.1 Introduction

Molecules interact with light via their electric (or magnetic) multipole moments, however largely we may use the dipole approximation, and only consider their transition dipole moments (TDM). Whereas the $|\langle \chi_f | \mu | \psi_s \rangle|^2$ between $| \chi_f \rangle$ and $| \psi_s \rangle$ energy eigenstates can be deduced from the strength of frequency-resolved spectral lines, it is much more difficult to use such data to determine the phases of the TDMs. Knowledge of these signs is however vital in many applications [125, 163, 164, 168, 170, 172, 173, 216]. For example, in the short pulse productions of wave packets [125, 216], the fluorescence signal is composed of the beatings between many transitions whose signs fundamentally affect the observations. The determination of the TDM's phases is highly desirable for such applications as these wave packet dynamics[125, 216] and quantum computation operations on atomic/molecular systems [163, 164, 168, 170, 172, 173].

The well-known "inverse scattering" problem [50] involves determining the phase of the complex-valued scattering amplitudes [43, 44] from (differential) cross section measurements. In bound-bound molecular spectroscopy the analogous "phase problem" is less daunting because the relevant amplitudes are $\langle \chi_f | \mu | \psi_s \rangle$ - the transition-dipole matrix elements (TDMs) which are *real*. The "phase problem" is thus reduced to a sign determination.

We have previously shown [128, 143, 144] in Chapter 3, that given the squares of the TDMs, we are able to derive the TDMs amplitudes and perform a point-by-point construction of the excited Born-Oppenheimer potential energy surface (PES) from which the emission occurs. In Chapter 4, we have also shown [176, 177, 217] that we can image time-evolving wave packets. However, the use of frequency resolved data entails satisfying certain "completeness conditions" [128, 143, 144]. Operationally,

this means that we need to know the magnitudes of spectral lines linked to a large number of final (electronically-ground) rovibrational states. At present such extensive data is not yet available.

An alternative method for TDM sign determination proposed in the past is based on the semi-classical stationary phase approximation. It assumes that $\langle \chi_f | \mu | \psi_s \rangle$ in a progression of $| \chi_f \rangle$ states, must go through zero and change sign whenever $|\langle \chi_f | \mu | \psi_s \rangle|^2$ hits a minimum (node) as s is varied. Unfortunately, this approach is often unreliable because the nodes can be very closely spaced (due to high kinetic energy or small transition amplitudes). In addition, the single stationary phase approximation fails for many cases, especially in the long wavelength regime, or when the main contributions to the TDMs come from the vicinity of the classical turning points.

In the present work we consider using time-resolved data [216], containing in principle information about many spectral transitions, as an effective way of overcoming the dearth of frequency resolved data noted above. We show that it is possible to use such data to derive the phases of individual TDMs between energy eigenstates. The method uses Bi-chromatic Coherent Control (BCC) [218] in conjunction with the performance of a finite-time Fourier transform [217] at various $(\omega_{s',s})$ beat components [48] of time-resolved fluorescence data. In the present use of BCC, one interferes between the stimulated emissions to a pre-determined ground state of a chosen pair of states that are part of the wave packet. When the relative phase between the two external light fields matches the relative phase of the two TDMs linked to a common ground state, the depletion of the Fourier transform of the signal at the $\omega_{s,s'}$ beat frequency, giving the $(\psi_s, \psi_{s'})$ pair contribution, is maximal.

One advantage of this method is that it does not require explicit knowledge of the $\chi_f(\mathsf{r})$ or $\psi_s(\mathsf{r})$ eigenfunctions. Another advantage is that the method is essentially non-destructive: Typically, spontaneous emission lifetimes are $10^{-8} - 10^{-6}$ seconds [48], hence, over the 1 - 10 ps time span of interest only $10^{-6} - 10^{-5}$ of the excited state molecules are destroyed via their decay.

In contrast to frequency-resolved experiments, time resolved experiments[216] that might in principle contain information about many spectral transitions, appear to be available. In the present paper we show how to use such data to derive the phase information for individual transitions between energy eigenstates. The method uses an approach developed for the imaging of molecular wave packets whose constituent energy eigenstates are known[217], in conjunction with Bi-chromatic Coherent Con-

trol (BCC)[218], thereby obviating the need to know the energy eigenstates. In this approach[217], one extracts the excited wave packet amplitudes and phases by taking a series of finite time Fourier transforms at the various $(\omega_{s',s})$ beat frequencies[48] contained in the time resolved fluorescence of the entire wave packet.

The way BCC helps obviate the need to know the constituents energy eigenstates is by inducing stimulated emission from a chosen pair of states comprising the wave packet to a pre-determined ground state. By tuning the relative phase between two external light fields to match the relative phase of two TDM's linked to a common ground state, one can attain maximum depletion of the population of the pair of states (s, s') whose Fourier transform at the beat frequency $\omega_{s,s'}$ is being computed.

5.2 Theory

We consider exciting $\chi_g(\mathsf{r})$, a vibrational energy eigenstate belonging to the ground electronic state, with r being a (collective) nuclear coordinate, by a short laser pulse to form a wave packet $\Psi(\mathsf{r}, t)$ moving on an unknown excited potential energy surface (PES), given as

$$\Psi(\mathsf{r}, t) = \sum_s a_s \psi_s(\mathsf{r}) \exp(-iE_s t/\hbar - \gamma_s t/2). \tag{5.1}$$

Our objective is to determine a_s, the expansion coefficients of Ψ in terms of $\psi_s(\mathsf{r})$, the excited vibrational eigenstates. Using frequency-resolved spectroscopic data, we may assume that we know the energy E_s, and the (spontaneous emission) decay rate, γ_s, for each ψ_s state, written as [125]

$$\gamma_s = \sum_f A_{f,s} \tag{5.2}$$

where $A_{f,s}$ are Einstein A-coefficients, given, in atomic units, as

$$A_{f,s} = \frac{4\omega_{f,s}^3}{3c^3} \left| \mu_{f,s} \right|^2, \tag{5.3}$$

with $|\mu_{f,s}| \equiv |\langle \chi_f | \mu | \psi_s \rangle|$ being a set of transition dipole matrix elements (TDM's) linking the electronically excited energy eigenstates and the ground energy eigenstates, χ_f.

In the past we have shown [6, 128, 143, 144] that knowledge of $|\mu_{f,s}|^2$ and the ground PES, enable the extraction of the phases of $\mu_{f,s}$ as well as the excited PES,

knowing which, we can calculate the excited state eigenstates $\psi_s(\mathbf{r})$. This information, together with knowledge of the excitation laser field, is sufficient for the determination of the expansion coefficients a_s, from which we can obtain the entire excited state wave packet $\Psi(\mathbf{r}, t)$. There are however difficulties in implementing this procedure in practice due to the scarcity of frequency-resolved studies that record *all* the transitions mandated by the *completeness* requirement of the method.

For this reason we now introduce an alternative approach that uses *time-resolved* data for the determination of the phases of $\mu_{f,s}$. The method, which by its very nature requires a less complete set of measurements, harnesses a technique recently developed by us for the imaging of excited wave packets moving on *known* PES[217]. It is based on writing the rate of the time-resolved fluorescence from the excited state wave packet of Eq. (5.1) as[125]

$$R(t) = \sum_{s,s'} a_s^* a_{s'}^* C_{s,s'} \exp(-i\omega_{s,s'}t) \tag{5.4}$$

where $\omega_{s,s'} = (E_s - E_{s'})/\hbar$ are "beat" frequencies [48], and $C_{s,s'}$ is a time-independent molecular matrix, given as

$$C_{s,s'} = \frac{2}{3c^3} \sum_f (\omega_{f,s}^3 + \omega_{f,s'}^3) \langle \psi_s | \mu | \chi_f \rangle \langle \chi_f | \mu | \psi_{s'} \rangle. \tag{5.5}$$

In the above we have neglected the decay due to spontaneous emission because for τ (the time scale of interest) of ~ 1 ps, $\gamma_s \tau << 1$. In other words, due to the relatively long spontaneous emission lifetimes of $10^{-8} - 10^{-6}$ seconds, only $10^{-6} - 10^{-5}$ of the excited molecules decay over the 1 - 10 ps time span of interest.

We now select[217] a specific (s, s') component of the $R(t)$ signal by calculating over time T the finite time Fourier transform (fFT) of $R(t)$ at each $\omega_{s,s'}$ beat frequency. In this way we filter out all other $\omega \neq \omega_{s,s'}$ components, which decay as $1/T$. We have that,

$$R(\omega) \equiv \frac{1}{T} \int_0^T dt R(t) \exp(i\omega t) \approx |C_{s,s'}||a_s||a_{s'}| \exp\left[i(\delta_{s,s'} + \xi_{s,s'})\right] \quad \text{for } \omega = \omega_{s,s'}, \tag{5.6}$$

where $\xi_{s,s'}(= 0, \pi)$ is the phase of the real matrix $C_{s,s'}$, and $\delta_{s,s'} = \delta_s - \delta_s'$ is a result

of expressing a_s as $a_s = |a_s| \exp(i\delta_s)$. In contrast, for $\omega \neq \omega_{s,s'}$,

$$R(\omega) = \frac{i}{T} \sum_{s,s'} \frac{C_{s,s'} a_s a_{s'}^* (\exp[i(\omega_{s,s'} - \omega)T] - 1)}{\omega_{s,s'} - \omega} = \mathcal{O}(1/T) \text{ for } \omega \neq \omega_{s,s'}.$$

Thus, in order to filter out all the Fourier components save for the $\omega_{s,s'}$ one, we need to choose $T \gg 1/\min|\omega_{s,s'} - \omega_{t,t'}|$ where $\omega_{t,t'} \neq \omega_{s,s'}$. The relatively long integration times (typically $T \sim 1$ ps) tend to average out random measurement errors in the time-resolved fluorescence, rendering the method quite robust.

Since only the exponential contributes to the complex nature of $R(\omega)$, we can use the outcome of Eq. (5.6) to determine $\delta_{s,s'}$ for all states s and s' up to $\xi_{s,s'} = 0, \pi$. In order to fix the sign of $C_{s,s'}$, (or $\xi_{s,s'}$) thereby resolving the π uncertainty in the phase of a_s, we use BCC[218] to extract the individual TDM's, from which we can, using Eq. (5.5), calculate $C_{s,s'}$. With knowledge of both $C_{s,s'}$ and $\delta_{s,s'}$ we have already shown[217] how to determine the magnitudes of a_s through solving a series of equations for each set of states (s, s').

The present application of BCC[68, 219, 220] consists of applying shortly after the formation of the excited wave packet of Eq. (5.1), a single broadband laser pulse $\epsilon(\omega)$, containing the $\epsilon(\omega_{s,f})$ and $\epsilon(\omega_{s',f})$ Fourier components that couple a pair of excited states ψ_s and $\psi_{s'}$ to a single ground state $|f\rangle$. By manipulating the magnitudes $|\epsilon(\omega_{s,f})|$ and phases $\phi(\omega_{s,f})$ of these two components we can coherently control the population transferred from the ψ_s and $\psi_{s'}$ components of $\Psi(t)$ to $|f\rangle$. The maximum effect will occur when the $\epsilon(\omega_{s,f}) a_s \mu_{s,f}$ product will be identical to the $\epsilon(\omega_{s',f}) a_{s'} \mu_{s',f}$ product which will then interfere constructively. Under these conditions knowledge of $\mu_{s,f}$ will enable us to extract $\mu_{s',f}$ according to,

$$\mu_{s',f} = \frac{a_s \epsilon(\omega_{s,f})}{a_{s'} \epsilon(\omega_{s',f})} \mu_{s,f} = \left| \frac{a_s \epsilon(\omega_{s,f})}{a_{s'} \epsilon(\omega_{s',f})} \right| \exp\left[i(\delta_{s,s'} + \phi_{s,s';f}) \right] \mu_{s,f}. \qquad (5.7)$$

Due to the reality of $\mu_{s',f}$, $\phi_{s,s';f} = \phi(\omega_{s,f}) - \phi(\omega_{s',f})$ must be equal to $-\delta_{s,s'}$ or to $\pi - \delta_{s,s'}$, depending on the sign of $\mu_{s',f}$ relative to $\mu_{s,f}$. Although at this point we do not know the magnitudes $|a_s|$ and $|a_{s'}|$, provided that neither $|a_s| >> |a_{s'}|$ nor $|a_s| << |a_{s'}|$, the population transfer resulting from complete constructive interference will be distinguishable from the case of destructive interference occurring when $\phi_{s,s';f} \rightarrow \phi_{s,s';f} + \pi$.

Noting that we are allowed to choose the phases of all (N_f) $|f\rangle$ states and the

phases of all (N_s) $|\psi_s\rangle$ states at will, then of the $N_s \times N_f$ transitions, we are free to choose the phases (or signs) of $N_s + N_f - 1$ of the TDM's. Therefore, we take all the μ_{s,f_1} associated with one, $|f_1\rangle$, state and all the $\mu_{s_1,f}$ associated with one, $|\psi_{s_1}\rangle$, state to be positive. The phases of the remaining TDM's depend, in addition to the overall phase factor multiplying each individual $|\psi_s\rangle$ or $|f\rangle$ wavefunction, on their detailed shape (*e.g.* nodal structure). Given this choice, it follows from Eq. (5.7) that the sign of every $\mu_{s,f}$ TDM's relative to the sign of μ_{s,f_1} is determined by whether $\phi_{s,s_1;f_1} - \phi_{s,s_1;f}$ is 0 or π.

Once the relative TDM signs are obtained in this manner, we use Eq. (4.5) to compute the $C_{s,s'}$ amplitudes. This allows us to use Eq. (5.6) to lift the π ambiguity in $\delta_{s,s'}$ and obtain the complex a_s amplitudes. We have thus chartered a way, using BCC and fFT, of obtaining both the amplitudes of the TDM's and the characterization of the time evolving wave packet $\Psi(t)$, without ever having computed the basis wavefunctions ψ_s!

The maximum in the population depletion resulting from the above application of BCC is detected as a minimum in $|R(\omega_{s,s'})|$ - the fluorescence Fourier component of Eq. (5.6). We choose this method in preference to other experimental techniques for population detection, such as laser-induced fluorescence(LIF) [221], resonantly enhanced multiphoton ionization (REMPI) [222], or, cross-correlation frequency-resolved optical coherent anti-Stokes Raman scattering (XFROG CARS) [192, 193], because each of the latter approaches requires additional laser fields and might be further complicated by other excitation pathways.

One possible complication that might result is that due to its large bandwidth the BCC pulse might affect other states that are close in energy to the targeted ones. If the BCC Fourier components couple $(s, s+1) \to f$, then they might also stimulate, although to a lesser extent, the $(s+1, s+2) \to f+1$, and $(s-1, s) \to f-1$ transitions. In practice however, as we show below, these ancillary stimulated emission processes, which occur at different frequencies of the pulse, $(\omega_{s+1,f+1}, \omega_{s+2,f+1})$ and $(\omega_{s,f-1}, \omega_{s-1,f-1})$ respectively, do not affect the signs of the $\mu_{s,f}$ derived from the maximal depletion in $|R(\omega_{s,s'})|$.

If cases arise where we find that the integrated signal for the two relative phase case of the BCC field are too similar, and thus indistinguishable, we may additionally tailor the ancillary components of the BCC field. This involves tuning the magnitude and phase of the pulse at the known frequencies $\{w_{s+1,f+1}, w_{s+2,f+1}\}$ and $\{, w_{s,f-1}, w_{s-1,f-1}\}$ in order to reduce the effects of the adjacent BCC processes

on the two excited states ψ_s and ψ_{s+1} of interest. Again, the field magnitudes at their components will be determined from the spectroscopic values of $|\mu_{s,f}|$ while the relative phases between the pairs of frequencies that minimize the coupling will be found to be either $-\delta_{s+1,s+2}$ or $\pi - \delta_{s+1,s+2}$ and $-\delta_{s-1,s}$ or $\pi - \delta_{s-1,s}$ respectively.

5.3   Simulations

5.3.1   Isolated Potential

We demonstrate our imaging procedure using time-resolved fluorescence for an excited sodium dimer (Na_2) wave packet, in a process depicted schematically in Fig.5.1, according to which a molecule, initially in the $X^1\Sigma_g^+$ ground rovibrational state ($|0\rangle = |v = 0; J = 0\rangle$) gets excited by a short ($\delta t \sim 20$fs) laser pulse to a wave packet of vibrational eigenstates belonging to the $A^1\Sigma_u^+$ electronic state. As illustrated in the inset of Fig.5.1, after the excitation pulse is over (at $t \sim 300$fs) we activate a weaker and longer "bichromatic coherent control"(BCC) pulse, dominated by two distinct frequencies that mainly couple two vibrational levels ($|s\rangle, |s'\rangle$) in $A^1\Sigma_u^+$ to the vibrational state $|f\rangle$ of $X^1\Sigma_g^+$.

After the BCC pulse, which we take to be a Gaussian of time-averaged intensity of 3×10^{10}W/cm^2 and bandwidth of 88cm^{-1}, is over (at $t \sim 500$fs), we collect the time-resolved fluorescence resulting from the decay of the population still residing in the excited states.The fluorescence is recorded every ~ 60fs over a period of ~ 10ps, a resolution that is attainable experimentally using up-conversion techniques [4, 5, 75].

As an example we choose a particular case of $\{s = 3, s' = 4, f = 5\}$, and $\mu_{3,5}\mu_{4,5} > 0$. In this case $\phi_{3,4;5} = -\delta_{3,4}$ corresponds to constructive interference, thereby maximizes the $|R(\omega_{3,4})|$ fluorescence depletion rate, whereas $\phi_{3,4;5} = \pi - \delta_{3,4}$ minimizes the fluorescence depletion. In Fig.5.2a we compare the time-resolved $R(t)$ fluorescence rate of Eq. (5.4) with BCC relative phase of $\phi_{3,4;5} = -\delta_{3,4}$, to the $\phi_{3,4;5} = \pi - \delta_{3,4}$ case. As shown in the Fig.5.2a, the result is a small ($\sim 5\%$) reduction in the fluorescence signal which would be difficult to detect experimentally. In contrast, as shown in the Fig.5.2b, the variation of $|R(\omega_{3,4})|$ of Eq. (5.6) with $\phi_{3,4;5}$ is very significant. When we ignore the ancillary transitions (black line), the fluorescence minimum, occurring exactly at $\phi_{3,4;5} = -\delta_{3,4}$, is 250% smaller than the fluorescence maximum, occurring at $\phi_{3,4;5} = \pi - \delta_{3,4}$. The relative difference remains high even when we do take into account the ancillary transitions (blue dashed line),
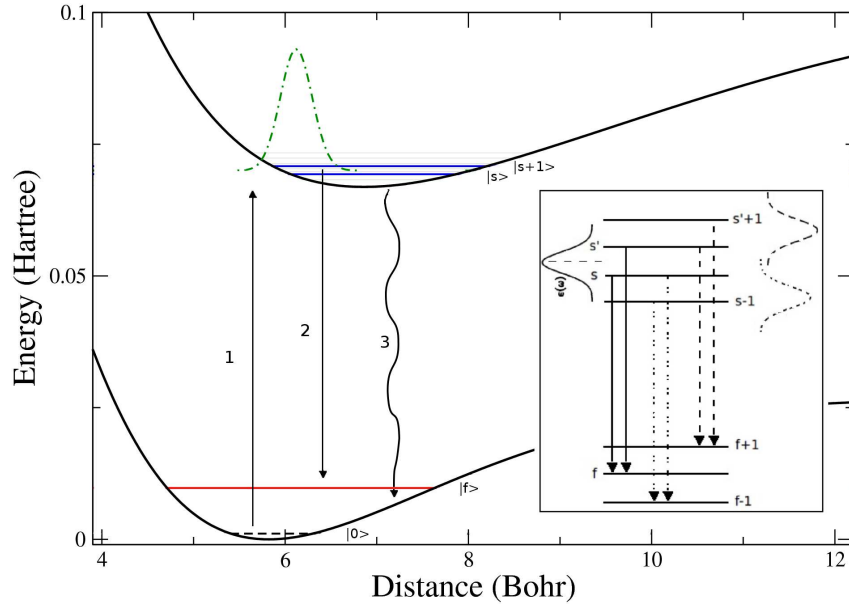
Figure 5.1: (Main drawing) The ground, $X^1\Sigma_g^+$, and first excited, $A^1\Sigma_u^+$, potential energy surfaces of Na$_2$ and a schematic description of the light pulses. Marked as (1) is the pulse exciting the ground vibrational eigenstates $|0\rangle$ to a set of excited vibrational eigenstates $|s\rangle$; (2) the BCC pulse coupling two excited state $|s\rangle$ and $|s'\rangle$ to a ground state $|f\rangle$; (3) the spontaneous emission from the $|s\rangle$ vibrational states of $A^1\Sigma_u^+$ to the $|f\rangle$ vibrational states of $X^1\Sigma_g^+$. (Inset) The BCC stimulated emission process which couples states $|s\rangle$ and $|s'\rangle$ to $|f\rangle$. Some ancillary couplings of adjacent $|s'+1\rangle$ and $|s-1\rangle$ states to different final states $|f\rangle$ may also result.

although the maximum gets shifted slightly to the left. In order to quantify the effect we plot in Fig. 5.2c the contrast ratio

$$C(0, \pi) = \frac{|R(\omega_{s,s'})_0 - R(\omega_{s,s'})_\pi|}{|R(\omega_{s,s'})_0 + R(\omega_{s,s'})_\pi|}, \tag{5.8}$$

where subscript 0 denotes the $\phi_{3,4;5} = -\delta_{3,4}$ phase choice, and subscript π denotes the $\phi_{3,4;5} = \pi - \delta_{3,4}$ phase choice. In Fig.5.2c, we display the contrast $C(0, \pi)$ as a function of the $|\epsilon(\omega_{s,f})/\epsilon(\omega_{s',f})|$ ratio. Since we know from Eq. (5.7) that the constructive interference occurs when $\epsilon(\omega_{s,f_1})a_s\mu_{s,f_1} = \epsilon(\omega_{s',f_1})a_{s'}\mu_{s',f_1}$, the contrast maximum as a function of $|\epsilon(\omega_{s,f_1})/\epsilon(\omega_{s',f_1})|$ immediately yields the $|a_s/a_{s'}|$ ratio (relative to $|\mu_{s,f_1}/\mu_{s',f_1}|$). Once the $|a_s/a_{s'}|$ ratios are known, we can, by varying the state $|f\rangle$, obtain all other $|\mu_{s,f}/\mu_{s',f}|$ TDM ratios.

This procedure is illustrated in Fig.5.2d where we present $|R(\omega_{3,4})_0 - R(\omega_{3,4})_\pi|$ for various final states $|f\rangle$, for a fixed $|\epsilon(\omega_{3,5})/\epsilon(\omega_{4,5})|$ ratio. The variation in the contrast with $|f\rangle$ yields the variation in the $|\mu_{s,f}/\mu_{s',f}|$ TDM ratios.

5.3.2 Coupled Excited State Potentials

A case of great importance and much greater complexity is a wave packet evolving on two coupled electronic states. Here the frequency-resolved methods used by us in the past to extract the TDM's[128, 143, 144], do not work because they rely on the existence of only one excited PES. In this section we demonstrate the viability of the present time-resolved method for such a case by determining the TDM's for the spin-orbit (SO) coupled RbCs system. Here the coupling occurs between the two lowest excited electronic states [223–225].

We simulate the intersystem dynamics assuming that we know the PES of the excited $A^1\Sigma^+$ singlet state and the $b^3\Pi$ excited triplet state[17]. In addition we assume that the electronic transition-dipole[226] and the $A^1\Sigma^+/b^3\Pi$ spin-orbit (SO) coupling [18, 19] functions are known. The above information allows us to calculate the frequency-resolved fluorescence line strengths $|\mu_{s,f}|^2$ of RbCs, where s denotes the vibrational states of the SO coupled $A^1\Sigma^+/b^3\Pi$ excited states, and f denotes the vibrational states of the $X^1\Sigma^+$ ground state[16] (or possibly the $a^3\Sigma^+$ lowest triplet state).

In order to produce the input time-resolved fluorescence we envision using an ultrashort broad-band pulse to excite the $X^1\Sigma^+(|v = 0\rangle)$ state to a wave packet composed of the $|s = 24 - 33\rangle$ vibrational eigenstates of the SO-coupled $A^1\Sigma^+/b^3\Pi$

(a)

(b)

(c)

(d)
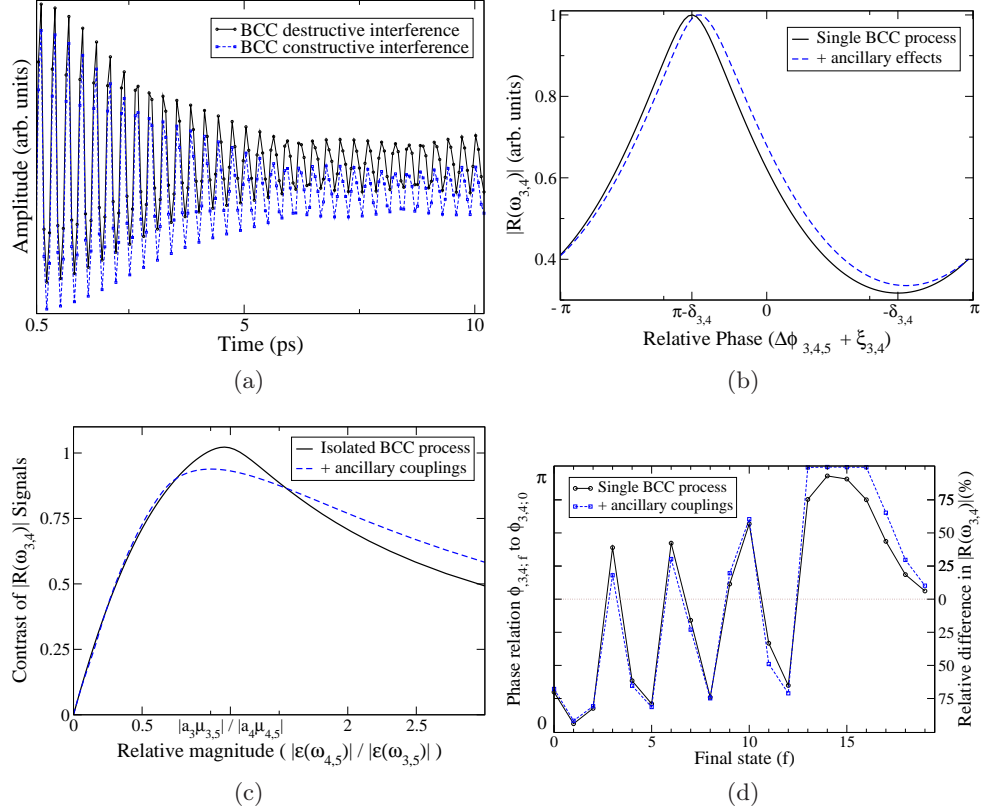
Figure 5.2: **(a)** $R(t)$ captured over 10 ps and strobed every 60 fs in the presence and absence of the BCC field which removes populations from the excited state. **(b)** $|R(\omega_{3,4})|$ as a function of the relative phase $\phi_{3,4;5}$ ranging over $-\pi$ to π. Full black line - f including only states $|3\rangle$ and $|4\rangle$; dashed blue line - the result of including in addition to states $|3\rangle$ and $|4\rangle$ *all* ancillary states. **(c)** The contrast, $C(0,\pi)$, of Eq.(5.8), as a function of $|\epsilon(\omega_{3,5})/\epsilon(\omega_{4,5})|$ - the ratio between the two interfering components of the BCC field, for fixed $|\epsilon(\omega_{3,5})|^2 + |\epsilon(\omega_{4,5})|^2$ sum of intensities. The line codes are as in (b). The maximum contrast marks the point at which $|\epsilon(\omega_{s,f})/\epsilon(\omega_{s',f})| = |a_{s'}\mu_{s',f}/a_s\mu_{s,f}|$, allowing us to extract $|a_{s'}/a_s|$ and (by varying $|f\rangle$) $|\mu_{s',f}/\mu_{s,f}|$. **(d)** $|R(\omega_{3,4})|$ at different $\phi_{3,4;0}$ - $\phi_{3,4;f}$ phase differences for various final states $|f\rangle$.
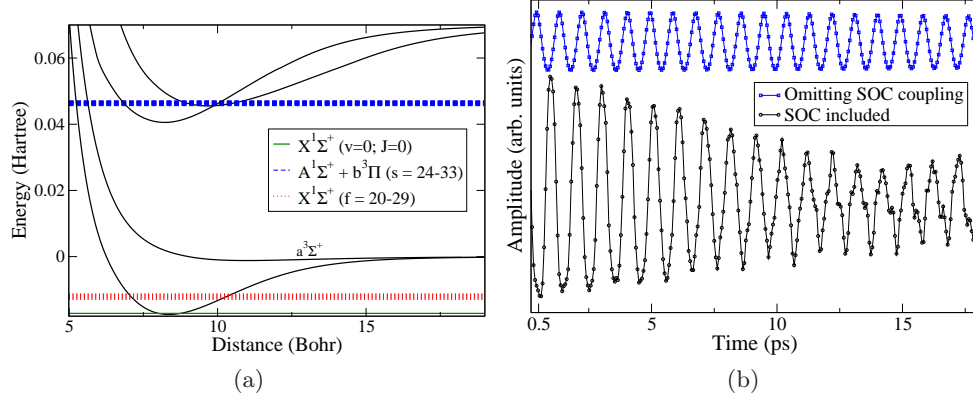
Figure 5.3: (a) Schematic of the RbCs system showing the four PES and the location of some vibrational eigenstates. (b) The resulting temporal fluorescence captures over several picoseconds for when the spin-orbit coupling (SOC) is excluded (blue-square) and included (black-circle).

electronic states. As shown in Fig. 5.3a, these eigenstates straddle the region of crossing between the $A^1\Sigma^+$ and $b^3\Pi$ PES, and in Fig. 5.3b we see the effect of the spin-orbit coupling (SOC) on the time-dependent fluorescence (black-circle) in contrast to the outcome when this coupling is omitted (blue-squares). We next simulate applying a BCC pulse whose $\phi_{s,s';f}$ phase differences between the $\omega_{s,f}$ and $\omega_{s',f}$ frequency components affect the fluorescence to one of the $|f = 20 - 29\rangle$ vibrational states of the $X^1\Sigma^+$ PES.

In Fig. 5.4a we display as blue circles the BCC pulse bandwidth (ranging over $\sim 14 - 22 \text{cm}^{-1}$), and as black bars - the intensities (ranging between $10^6 - 10^{12}$ W/cm^2) used for each $|s\rangle$ and $|s'\rangle$ excited pair and the $|f = 20 - 29\rangle$ final vibrational states for which we extract the TDM's.

We demonstrate, in Fig. 5.4b, a very successful extraction of the SO-coupled singlet/triplet components (a_s) of the excited wave packet for two time points at the excitation pulse center $t = 0$ (blue points), and after 10 ps (red points). The imaged values (thick black line) appear to faithfully reproduce the "true" values, where we have assumed knowledge of the SO-coupled eigenfunctions for presentational purposes. Figure 5.4b exhibits a transition, taking place over the 10 ps time span, from a wave packet (blue curve) centered about the singlet potential minimum, to a wave packet centered about the triplet potential minimum (red curve). A behavior of this sort is only possible if the blue curve is mostly singlet and the red curve is mostly

Figure 5.4: (a) The BCC pulse intensity (black bars) and bandwidth (blue circles) used to achieve sufficient $C(0, \pi)$ contrast (of at least 20%). The range of the pulse intensity used was varied as a function of the final $X^1\Sigma^+$ state ($f = 20 - 29$) probed. (b) Extraction of the singlet and the triplet components of an excited wave packet $\Psi(r, t)$ at $t = 0$, the excitation pulse center ("true" wave packet - blue points) and after 10 ps ("true" wave packet - red points). The imaged wave packet, given at both times as a thick black line, faithfully reproduces the "true" values. Shown also are the $A^1\Sigma_u^+$ (thin black line) and $b^3\Pi$ (dashed line) PES.

triplet. The wave packet, composed of the SO coupled eigenstates, starts out as a singlet because the selection rules of the optical transition from the ground singlet create at t=0 only the singlet part of the wave packet. The temporal evolution of the wave packet which changes the extracted a_s expansion coefficients to $a_s exp(iE_st)$ gradually builds up a triplet component which, as shown in Fig. 5.4b, becomes very prominent at t=10 ps.

5.3.3 LiRb Coupled Potentials

In this section, we demonstrate our TDM extraction procedure using time-resolved fluorescence for an excited lithium-rubidium dimer (LiRb) wave packet evolving on the spin-orbit (SO) coupled $A^1\Sigma_u^+$ and $b^3\Pi$ electronic states [33, 227–229]. In Fig. 5.5a, we depict the ground state singlet, $X^1\Sigma_g^+$, and triplet $a^3\Sigma^+$, and two lowest excited PES of LiRb. We also schematically present the light pulses. Marked as (1) is a short ($\delta t \sim 20$fs) pulse exciting the ground vibrational eigenstates $|0\rangle = |v = 0; J = 0\rangle$ to a set of SO-coupled excited vibrational eigenstates $|\psi_s\rangle$. Marked as (2) is the BCC pulse, dominated by two distinct frequencies, coupling two excited state $|\psi_s\rangle$ and $|\psi_{s'}\rangle$ to a ground state $|\chi_f\rangle$ in $X^1\Sigma_g^+$ (or $a^3\Sigma^+$). Marked as (3) is the

(a)

(b)
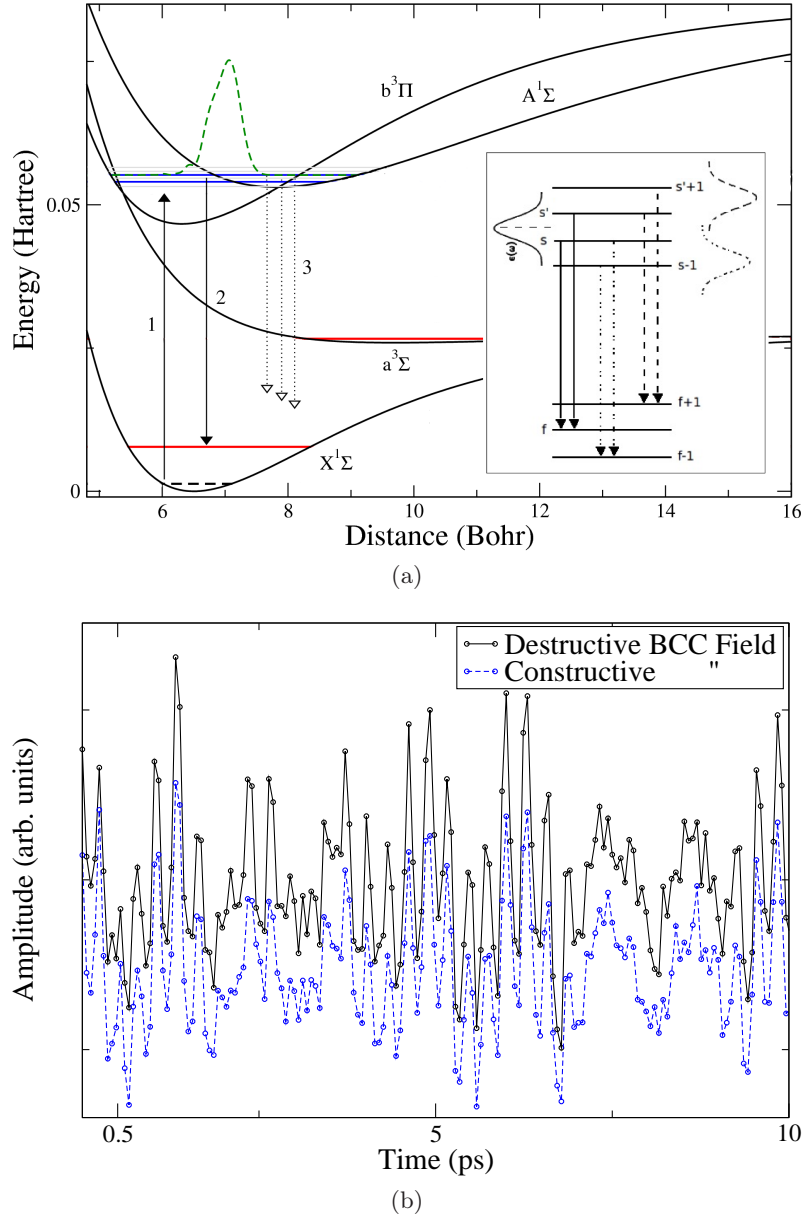
Figure 5.5: **(a)** (Main) Schematics of the LiRb system showing four PES's and select rovibrational eigenstates. (Inset) The BCC stimulated emission process which couples states $|\psi_s\rangle$ and $|\psi_{s'}\rangle$ to $|\chi_f\rangle$. Some ancillary couplings of adjacent $|\psi_{s'+1}\rangle$ and $|\psi_{s-1}\rangle$ states to different final states $|\chi_f\rangle$ may also result. **(b)** Temporal fluorescence captured over 10 ps and strobed every 60 fs for two different relative phase choices of the BCC field which either leaves or removes populations from two (or more) of the excited states.

fluorescence of the molecules remaining in the $|\psi_s\rangle$ vibrational states of $A^1\Sigma_u^+ \sim b^3\Pi$. The fluorescence is to the $|\chi_f\rangle$ vibrational states of the $X^1\Sigma_g^+$ and $a^3\Sigma^+$ states. The fluorescence is collected every ~ 60fs over a period of ~ 10ps. This degree of temporal resolution is possible due to the use of up conversion techniques [4, 5, 75].

BCC to a$^3\Sigma$ State

As an example we choose a particular case of $\{\psi_{17}, \psi_{18}, \chi_{10}\}$, where $\mu_{17,10}\mu_{18,10} > 0$, and $|\chi_f\rangle$ lies in $a^3\Sigma$. In this case $\phi_{17,18;10} = -\delta_{17,18}$ corresponds to constructive interference, thereby minimizing the fluorescence depletion rate (appearing as a maximum in $|R(\omega_{17,18})|$), whereas $\phi_{17,18;10} = \pi - \delta_{17,18}$ maximizes the fluorescence depletion (reducing the signal $|R(\omega_{17,18})|$). In Fig. 5.2a we compare $R(t)$, the time-resolved fluorescence rate of Eq. (5.4) after a BCC pulse (time-averaged intensity of 1×10^{10}W/cm^2 and bandwidth of 36cm^{-1},) with relative phase of $\phi_{17,18;10} = -\delta_{17,18}$, to the case when $\phi_{17,18;10} = \pi - \delta_{17,18}$. As shown in the Fig. 5.2a, there is $\sim 20\%$ reduction in the fluorescence signal between the two cases. For such large differences that can confidently be distinguished experimentally, we immediately know which BCC phases choice lead to constructive (and which to destructive) interference, and therefore have determined the relative phase (or sign) between two TDMs ($\mu_{17,10}$ and $\mu_{18,10}$).

Often the primary time-dependent signals may not be so easily discriminated due to different TDM magnitudes. In this case we turn to the Fourier transform filtering technique. As shown in the Fig. 5.2b, the variation of $|R(\omega_{17,18})|$ of Eq. (5.6) with $\phi_{17,18;10}$ is very significant. We find the minima and maxima occurring at the expected values of $\phi_{17,18;10}$, the ancillary BCC processes having the minor effect of narrowing the range or slightly shifting the extrema points. When we ignore the ancillary transitions (black line), the fluorescence maximum, occurring exactly at $\phi_{17,18;10} = -\delta_{17,18}$, is several times larger than the fluorescence minimum, occurring at $\phi_{17,18;10} = \pi - \delta_{17,18}$. This difference remains high even when we do take into account the ancillary transitions (blue dashed line). In order to quantify this effect we plot in Fig. 5.2c the contrast ratio

$$C(0, \pi) = \frac{|R(\omega_{s,s'})_0 - R(\omega_{s,s'})_\pi|}{|R(\omega_{s,s'})_0 + R(\omega_{s,s'})_\pi|}, \tag{5.9}$$

where subscript 0 denotes the $\phi_{17,18;10} = -\delta_{17,18}$ phase choice, and subscript π denotes the $\phi_{17,18;10} = \pi - \delta_{17,18}$ phase choice. In Fig. 5.6b, we display the contrast
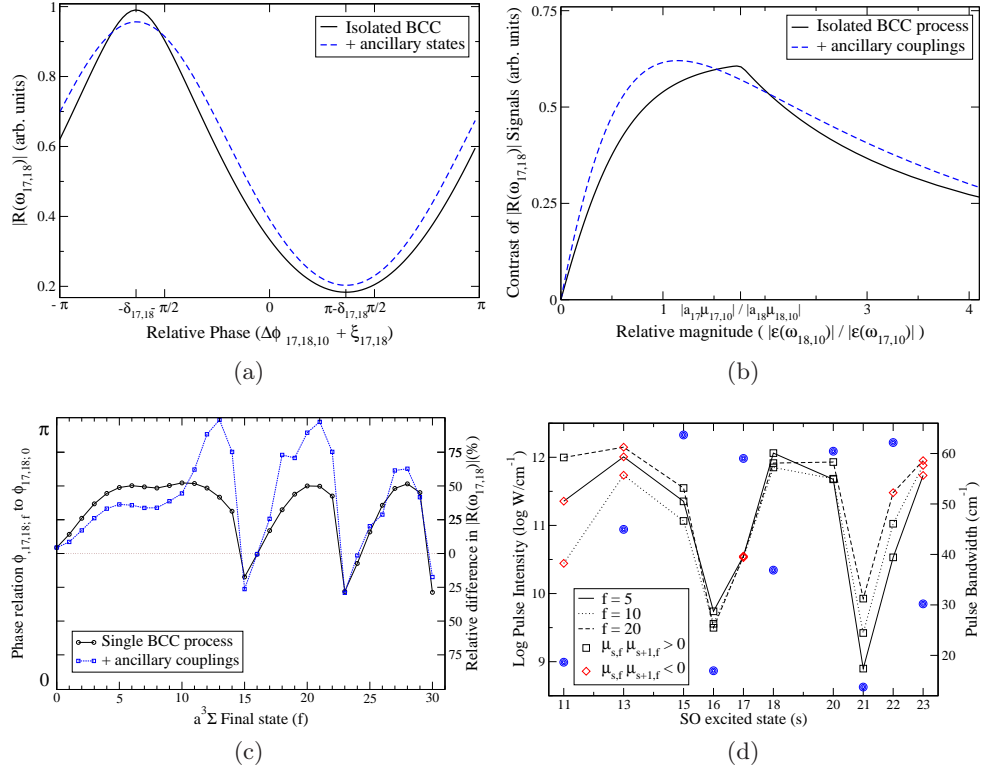
Figure 5.6: **(a)** $|R(\omega_{17,18})|$ as a function of the relative phase $\phi_{17,18;10}$ ranging over $-\pi$ to π. Full black line - including only states $|17\rangle$ and $|18\rangle$; dashed blue line - the result of including in addition to states $|17\rangle$ and $|18\rangle$ *all* ancillary states. **(b)** The contrast, $C(0,\pi)$, of Eq.(5.9), as a function of $|\epsilon(\omega_{17,10})/\epsilon(\omega_{18,10})|$ - the ratio between the two interfering components of the BCC field, for fixed $|\epsilon(\omega_{17,10})|^2 + |\epsilon(\omega_{18,10})|^2$ sum of intensities. The line codes are as in **(a)**. The maximum contrast marks the point at which $|\epsilon(\omega_{s,f})/\epsilon(\omega_{s',f})| = |a_{s'}\mu_{s',f}/a_s\mu_{s,f}|$, allowing us to extract $|a_{s'}/a_s|$ and (by varying $|\chi_f\rangle$) $|\mu_{s',f}/\mu_{s,f}|$. **(c)** $|R(\omega_{17,18})_0 - R(\omega_{17,18})_\pi|$ values at different $\phi_{17,18;0}$ - $\phi_{17,18;f}$ phase differences for various final states $|\chi_f\ran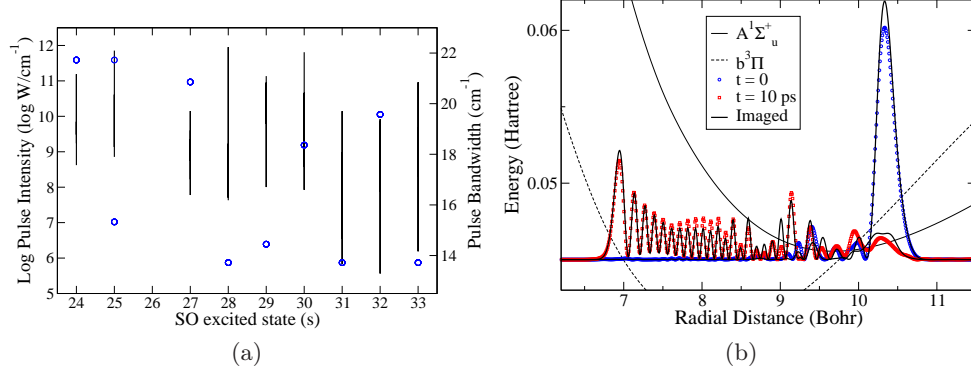gle$. **(d)** The BCC pulse intensity (line-points) and bandwidth (blue circles) used to achieve sufficient $C(0,\pi)$ contrast (of at least 20%). The range of the pulse intensity used is shown for three final $a^3\Pi$ state (χ_f) probed as a function of the lower $A^1\Sigma_u^+ \sim b^3\Pi$ coupled excited state (ψ_s). The red diamonds (black squares) depict what happens when $\mu_{s,f}$ and $\mu_{s+1,f}$ have identical (opposite) signs.

$C(0, \pi)$ as a function of the $|\epsilon(\omega_{s,f})/\epsilon(\omega_{s',f})|$ ratio. Since we know from Eq. (5.7) that the constructive interference occurs when $\epsilon(\omega_{s,f_1})a_s\mu_{s,f_1} = \epsilon(\omega_{s',f_1})a_{s'}\mu_{s',f_1}$, the contrast maximum as a function of $|\epsilon(\omega_{s,f_1})/\epsilon(\omega_{s',f_1})|$ roughly yields the $|a_s/a_{s'}|$ ratio (relative to $|\mu_{s,f_1}/\mu_{s',f_1}|$). This should be in agreement with the $|a_s/a_{s'}|$ ratios obtained from the finite time Fourier transform after we have compute the $C_{s,s'}$ amplitudes using Eq. (4.5). Recall, that we first lift the π ambiguity in $\delta_{s,s'}$ by extracting a series of $\mu_{s,f}\mu_{s',f}$ relations for fixed $(\psi_s, \psi_{s'})$ over a range of final states f. This procedure is illustrated in Fig. 5.6c where we present $|R(\omega_{17,18})_0 - R(\omega_{17,18})_\pi|/R(\omega_{17,18})|$ for various final states $|\chi_f\rangle$ in a$^3\Sigma$, for a fixed $|\epsilon(\omega_{17,f})/\epsilon(\omega_{18,f})|$ ratio. The variation in the contrast with $|\chi_f\rangle$ is related to the variation in the $|a_s\mu_{s,f}/a_{s'}\mu_{s',f}|$ TDM ratios and the BCC field intensity. Due to the nature of the PES, we find $\mu_{s,f}\mu_{s',f} > 0$ for nearly all lower levels in a$^3\Sigma$, with exception to the ambiguous cases where $|\mu_{s,f}|$ becomes very small ($<5\%$ of the average of the TDMs) and we cannot resolve the sign relation with greater than 10% difference (shown in Fig. 5.6c for $f = \{0, 15, 16, 23, 24, 30\}$). The effect of including the ancillary states, which is generally unpredictable without complete knowledge of the system, does not greatly alter the behavior of the integrated fluorescence signal.

In Fig. 5.6d we display as blue circles – the BCC pulse bandwidth (ranging over $\sim 14 - 65\text{cm}^{-1}$), and line-points – the intensities (ranging between $10^9 - 10^{12}$ W/cm^2) used to achieve sufficient $C(0, \pi)$ contrast (of at least 20%). For each $|\psi_s\rangle$ and $|s' = s + 1\rangle$ excited pair and three $|f = 5, 10, 20\rangle$ final vibrational states for which we extract the TDMs, we label the phase relation between the $\mu_{s,f}$ and $\mu_{s+1,f}$ terms as black squares (same sign) or red diamonds (opposite sign). All phases were extracted using experimentally reasonable parameters and found to be in agreement with actual values.

BCC to X$^1\Sigma$ State

Similar to the previous example, we produce the input time-resolved fluorescence by using an ultrashort broad-band pulse to excite the $X^1\Sigma^+(|\chi_0\rangle)$ state to a wave packet composed of the $|\psi_{s=11-23}\rangle$ vibrational states of the SO-coupled $A^1\Sigma^+ \sim$b$^3\Pi$ electronic states. As shown in Fig. 5.5a, these eigenstates straddle the region of crossing between the $A^1\Sigma^+$ and $b^3\Pi$ PES. We next simulate applying a BCC pulse whose $\phi_{s,s';f}$ phase differences between the $\omega_{s,f}$ and $\omega_{s',f}$ frequency components affect the fluorescence to one of the $|f = 0 - 20\rangle$ vibrational states of the X$^1\Sigma^+$ PES. In Fig.5.7a we demonstrate the same calculation as that shown in Fig. 5.6c,
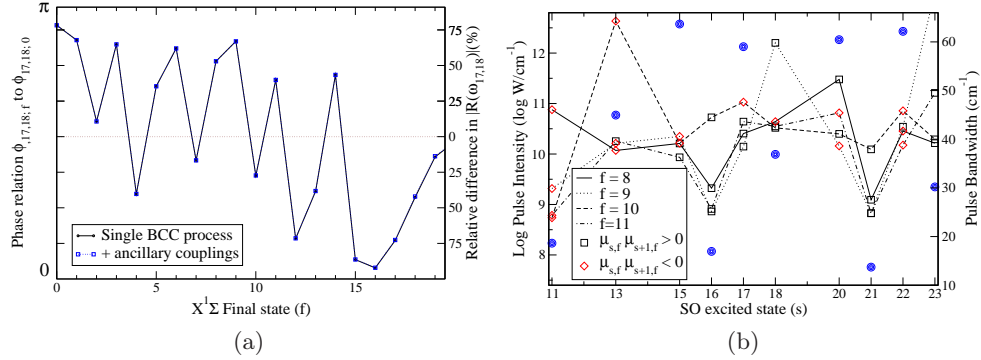
Figure 5.7: **(a)** Absolute difference of $|R(\omega_{17,18})|$ values for 0 and π cases at different $\phi_{17,18;0}$ - $\phi_{17,18;f}$ phase differences for various final states $|\chi_f\rangle$ in $X^1\Sigma$. **(b)** The BCC pulse intensity (line-points) and bandwidth (blue circles) used to achieve sufficient $C(0,\pi)$ contrast (of at least 20%). The range of the pulse intensity used is shown for four final $X^1\Sigma$ state (χ_f) probed as a function of the lower $A^1\Sigma_u^+ \sim b^3\Pi$ coupled excited state (ψ_s). The black squares (red diamonds) represent when $\mu_{s,f}$ and $\mu_{s+1,f}$ have similar (opposite) signs.

though now, with the BCC fields coupling rovibrational levels (χ_f) in the ground singlet state $X^1\Sigma$. We observe that the relative difference between the $|R(\omega_{17,18})_0$ and $R(\omega_{17,18})_\pi|$ values is generally significant enough for reliable differentiation at a fixed field intensity of 10^{10} W/cm^2. That is until the magnitudes of the TDM become very small when as f becomes large $(f \gtrsim 20)$. The location of the points relative to the zero line indicate the phase relation between the $\mu_{s,f}$ and $\mu_{s+1,f}$ values. Our results are in complete agreement with the expected signs for $\mu_{s,f}\mu_{s+1,f}$, and these do not change noticeably with the inclusion of ancillary BCC processes.

Similar to Fig. 5.6d, we provide Fig. 5.7b which depicts the BCC pulse bandwidths (blue circles) and intensities (points) required to achieve sufficient $C(0,\pi)$ contrast (of at least 20%). The pulse parameters are shown for the ψ_s and $\psi_{s'=s+1}$ excited pairs coupling to four consecutive final vibrational states $\chi_{f=8,9,10,21}$ in the $X^1\Sigma$ PES. We label the phase relation between the TDMs, $sgn(\mu_{s,f}\mu_{s+1,f})$, as before (black square – same, red diamond – opposite), and find complete agreement with the expected signs. Only in the cases in which these magnitudes are very small (*e.g.* $\mu_{13,10}, \mu_{18,9}, \mu_{23,9}$), and thus negligible, is the BCC pulse intensity, which is directly related to the strength of the TDMs, beyond that of our perturbative approach.

With knowledge of the magnitude and signs of the TDMs from rovibrational levels in $X^1\Sigma$ to the $A^1\Sigma^+ \sim b^3\Pi$ spin-orbit coupled states, we can extract the a_s
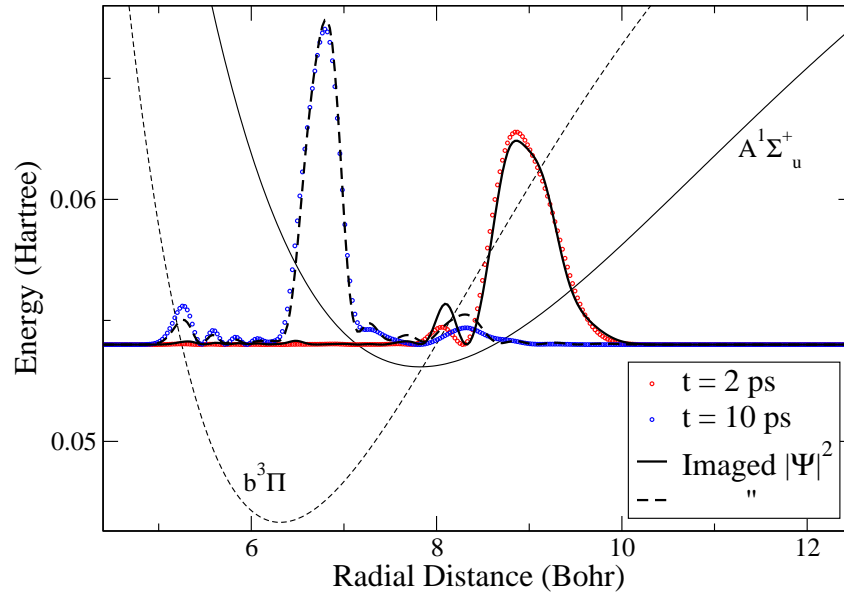
Figure 5.8: Extraction of the singlet and the triplet components of an excited wave packet $\Psi(\mathsf{r}, t)$ at $t = 2$ ps, the excitation pulse centre ("true" wave packet - red points) and after 10 ps ("true" wave packet - blue points). The imaged wave packet, given at both times as a thick black line, faithfully reproduces the "true" values. Shown also are the $A^1\Sigma_u^+$ (thin black line) and $b^3\Pi$ (dashed line) PES.

excited state coefficients of a time-evolving wave packet [176, 177, 217]. In Fig. 5.8 we show results for our wave function imaging performed in this way. We demonstrate a very successful extraction of the complex amplitudes (with average error $\approx$0.2%) at two time points, when $t = 2$ ps (red points), and after 10 ps (blue points). The imaged values (thick black line) appear to faithfully reproduce the "true" values. We see very clearly how a wave packet predominately in the singlet state region leaks into the triplet state after several picoseconds.

5.4 Conclusion

We have shown how time-resolved fluorescence data in conjunction with Bi-chromatic Coherent Control (BCC) can be used to derive the phases as well as the amplitudes of the a_s expansion coefficients of a wave packet $\Psi(r,t) = \sum_s a_s \psi_s(r) \exp(-iE_s t/\hbar)$, where $\psi_s(r)$ are vibrational eigenfunctions. The method can also be used to extract the magnitudes *and* phases of $\mu_{s,f}$, the individual transition dipole matrix-elements (TDM's) between energy eigenstates, ψ_s and ψ_f. The extraction of a_s and $\mu_{s,f}$ does not necessitate having prior knowledge of the PES and/or SO-coupling terms, nor do we need to know the $\psi_s(r)$ functions. Imaging of $\Psi(r,t)$ in coordinate space, would appear to necessitate knowledge the PES because it necessitates knowing $\psi_s(r)$, but as we showed in the past [128, 143, 144, 176, 177, 217], it is possible, using the $|\mu_{s,f}|$ magnitudes, to extract the excited states PES from which we can calculate $\psi_s(r)$.

Chapter 6

Extraction of Non-Adiabatic Couplings

Recent advances in chemical reaction dynamics [230, 231]; the imaging of electronic wave functions [232]; the creation of ultracold molecules [25, 233, 234]; and the use of molecules for quantum information applications [156–159, 161, 161, 167, 169], have stimulated a drive towards a better (preferably representation free) quantification of molecular properties beyond the Born Oppenheimer approximation (BOA). In particular, one would like to develop methods for a point-by-point extraction ("inversion") of excited state potential energy surfaces (PES) and the non-Born-Oppenheimer terms that couple them. So far, such inversion efforts [6, 7, 125, 128, 128, 143] have been applicable only to isolated electronic states where the BOA is valid. The above methods are inapplicable when electronic states interact, giving rise to "avoided crossings" or "conical intersections".

One of the simplest mechanisms for electronic state interactions is that of spin-orbit coupling (SOC) [235, 236]. SOC has been intensely studied in alkali-metal diatomic molecules and has been found to give rise to interesting phenomena such as inter-system crossing [235], "window" states [236], and Feshbach resonances [237–239]. An accurate description of the SOC in a molecule is of vital importance, as it allows for better understanding the internal dynamics and for developing accurate quantum control schemes within these systems.

Traditional *ab initio* methods are not effective at providing this information, since they often ignore the diagonal and off-diagonal corrections to the BOA. Although modern *ab initio* calculations are beginning to reach higher levels of accuracy (within 5 cm^{-1}) [76, 77], many spectroscopic experiments require knowledge of the relevant energies to a much greater precision in order to practically perform the desired measurements [112, 240] (especially in the case of [112] where the measurements were made in a regime where no prior experimental knowledge existed). An alternative, is to iteratively construct a multi-parameter fit of the SOC term to accommodate

experimental data, such as, from laser-induced fluorescence and Fourier-transform spectroscopy. Considerable progress in executing this strategy has been made by Bergeman and others [92–97], however the SOC term obtained in this manner is non-unique. Moreover, the procedure is very difficult to execute because one must obtain the line positions by diagonalizing a large set of differential or (even larger set of) algebraic equations, in each iteration step. Bussery and Aubert-Frécon have derived the full SOC matrix, analytically, for alkali dimers at long-range where SOC effects emerge [112, 241]. Their approach has been used by Le Roy and company [107, 242] to determine for certain states of Li$_2$, the resonance dipole-dipole interaction term C_3 which is the leading long-range contribution to the spin-orbit coupling matrix. Unfortunately, their method suffers from requiring a great amount of spectroscopic information in order to compute the non-adiabatic (spin-orbit) couplings.

The present chapter attempts to remedy many of these drawbacks: We derive a *strict inversion* procedure which extracts the radial dependence of the SOC from experimental data via an analytic formula which directly ties the SOC terms with the observed line positions and their transition-dipole matrix elements (TDMs).

6.1 Theory

We first consider two non-interacting singlet and triplet excited PES within the BOA. The time-independent Schödinger equation for each potential is written as

$$H^S | E^S \rangle = E^S | E^S \rangle \quad \text{and} \quad H^T | E^T \rangle = E^T | E^T \rangle \, , \tag{6.1}$$

where H^S, E^S and $| E^S \rangle$ represent the decoupled singlet Hamiltonian, its respective energy eigenvalues, and their corresponding eigenstates. An analogous definition applies to H^T, E^T and $| E^T \rangle$ for the triplet state. Each of the H^S or H^T Hamiltonians are given as

$$H^S = T_N + W^S, \quad H^T = T_N + W^T, \tag{6.2}$$

where T_N is the nuclear kinetic energy operator and $W^{S(T)}$ are the singlet (triplet) diabatic, or decoupled, potentials. The interaction between these potentials is assumed to arise from the SO term, H^{SO} [235]; similar to Bergeman *el al.* [17, 19] we have neglected other, smaller, non-adiabatic effects such as: hyperfine, Zeeman, spin-spin, *etc.* In the diabatic representation this SO term results in diagonal, $V^D(R)$, and off-diagonal, $V^{OD}(R)$, SO functions of the nuclear coordinate, R.

Following other authors [17, 19, 106, 243], we write the full SOC Hamiltonian in the decoupled singlet and triplet diabatic basis as

$$
\mathsf{H} = \begin{pmatrix} \hat{\mathsf{E}}^S & \mathsf{V}^{OD} \\ \mathsf{V}^{OD\dagger} & \hat{\mathsf{E}}^T + \mathsf{V}^D \end{pmatrix} \tag{6.3}
$$

where $\hat{\mathsf{E}}^S$ and $\hat{\mathsf{E}}^T$ are diagonal matrices of the rovibrational eigenvalues for the singlet and triplet potentials. The dimensions of these matrices are determined by the number of singlet (N_S) and triplet (N_T) eigenvalues, namely, $\hat{\mathsf{E}}^S$ is $N_S \times N_S$, $\hat{\mathsf{E}}^T$ is $N_T \times N_T$, and V^{OD} is $N_S \times N_T$. The rovibrational matrix elements of the SO components are defined as

$$
(V^{OD})_{i,j} = \langle\, E_i^S\, |V^{OD}(R)|\, E_j^T\,\rangle\,, \quad \text{and} \quad (V^D)_{i,j} = -\langle\, E_i^T\, |V^D(R)|\, E_j^T\,\rangle\,, \tag{6.4}
$$

where the integration over the radial-dependent SOC functions, $V^{OD}(R)$ and $V^D(R)$, is taken over R. We diagonalize the full SOC Hamiltonian as

$$
\hat{\mathsf{E}} = \mathsf{U}^\dagger \mathsf{H} \mathsf{U} \tag{6.5}
$$

where $\hat{\mathsf{E}}$ is an $N \times N$ diagonal matrix composed of the full $N = N_S + N_T$ SOC eigenvalues. The unitary matrix, U, is constructed from the corresponding fully interacting eigenstates, in the given basis, arranged in columns. Multiplying the two sides of Eq. (6.5) by U we represent Eq. (6.5) in a 2×2 block form as

$$
\begin{pmatrix} \mathsf{U}_u^S & \mathsf{U}_l^S \\ \mathsf{U}_u^T & \mathsf{U}_l^T \end{pmatrix} \cdot \begin{pmatrix} \hat{\mathsf{E}}_u & 0 \\ 0 & \hat{\mathsf{E}}_l \end{pmatrix} = \begin{pmatrix} \hat{\mathsf{E}}^S & \mathsf{V}^{OD} \\ \mathsf{V}^{OD\dagger} & \hat{\mathsf{E}}^T + \mathsf{V}^D \end{pmatrix} \cdot \begin{pmatrix} \mathsf{U}_u^S & \mathsf{U}_l^S \\ \mathsf{U}_u^T & \mathsf{U}_l^T \end{pmatrix} \tag{6.6}
$$

where the subscripts u and l denote respectively the the upper and lower elements of the diagonal matrix $\hat{\mathsf{E}}$. Writing two equations for the upper portion of Eq. (6.6) gives

$$
\mathsf{U}_u^S \cdot \hat{\mathsf{E}}_u = \hat{\mathsf{E}}^S \cdot \mathsf{U}_u^S + \mathsf{V}^{OD} \cdot \mathsf{U}_u^T \quad \text{and} \quad \mathsf{U}_l^S \cdot \hat{\mathsf{E}}_l = \hat{\mathsf{E}}^S \cdot \mathsf{U}_l^S + \mathsf{V}^{OD} \cdot \mathsf{U}_l^T\,, \tag{6.7}
$$

either of which could be solved directly for the off-diagonal SOC matrix, V^{OD}, assuming that we know the U's and E's. Note that the dimensions of the first equations are $N_S \times N_S$, which can be seen from the dimensions of the sub-matrices U_u^S ($N_S \times N_S$), $\hat{\mathsf{E}}_u$ ($N_S \times N_S$), and U_u^T ($N_T \times N_S$). On the other-hand, the second equation has

dimensions of $N_S \times N_T$ since its constituent sub-matrices are U_l^S ($N_S \times N_T$), $\hat{\mathsf{E}}_l$ ($N_T \times N_T$), and U_l^T ($N_T \times N_T$). Consider the case in which the dimensions of these two equations are the same, namely, that the number of singlet (N_S) and triplet (N_T) eigenvalues are equal, where the total number of SOC states $N = 2N_S = 2N_T$. Now, we may sum the matrix equation in Eqs. (6.7) and rearrange to yield

$$\mathsf{V}^{OD} = \left\{ \mathsf{U}_u^S \cdot \hat{\mathsf{E}}_u + \mathsf{U}_l^S \cdot \hat{\mathsf{E}}_l - \hat{\mathsf{E}}^S \cdot \left(\mathsf{U}_u^S + \mathsf{U}_l^S \right) \right\} \cdot \left\{ \mathsf{U}_u^T + \mathsf{U}_l^T \right\}^{-1} . \tag{6.8}$$

This expression now has the advantages of averaging the result for V^{OD} over more data, and improving the condition number of the matrix targeted for inversion, which would otherwise suffer when a particular SOC state doesn't contain much triplet character (if the columns of U_u or U_l were nearly zero, there may be trouble solving by the use of a matrix inverse). Once V^{OD} is known, we can solve for V^D by using the lower portion of Eq. (6.6), yielding two similar equations,

$$\mathsf{U}_u^T \cdot \hat{\mathsf{E}}_u = \mathsf{V}^{OD\dagger} \cdot \mathsf{U}_u^S + \hat{\mathsf{E}}^T \cdot \mathsf{U}_u^T - \mathsf{V}^D \cdot \mathsf{U}_u^T \quad \text{and} \quad \mathsf{U}_l^T \cdot \hat{\mathsf{E}}_l = \mathsf{V}^{OD\dagger} \cdot \mathsf{U}_l^S + \hat{\mathsf{E}}^T \cdot \mathsf{U}_l^T - \mathsf{V}^D \cdot \mathsf{U}_l^T , \tag{6.9}$$

with dimensions $N_T \times N_S$ and $N_T \times N_T$ respectively. These can easily be combined (when $N_S = N_T$) to give

$$\mathsf{V}^D = \left\{ \mathsf{V}^{OD\dagger} \cdot \left(\mathsf{U}_u^S + \mathsf{U}_l^S \right) + \hat{\mathsf{E}}^T \cdot \left(\mathsf{U}_u^T + \mathsf{U}_l^T \right) - \mathsf{U}_u^T \cdot \hat{\mathsf{E}}_u - \mathsf{U}_l^T \cdot \hat{\mathsf{E}}_l \right\} \cdot \left\{ \mathsf{U}_u^T + \mathsf{U}_l^T \right\}^{-1} . \tag{6.10}$$

It follows from Eq. (6.8) and Eq. (6.10) that we can extract the SO matrices using the diabatic singlet energies $\hat{\mathsf{E}}^S$ and the set of fully interacting eigenvalues $\hat{\mathsf{E}}_u$ and $\hat{\mathsf{E}}_l$, along with their corresponding eigenvectors in the diabatic basis (arranged in U_u^S, U_l^S, U_u^T and U_l^T). We now show how to obtain the latter quantities from photo-absorption or photo-emission data. We start by assuming: (*i*) that W^S and W^T, the "zero-order" decoupled singlet and triplet PES of Eq. (6.2), are known to us, and (*ii*) that we know the TDMs between the physical (fully interacting) excited manifold to some set of N_s lower singlet (s) and N_t lower triplet (t) states that are physically decoupled from one another. The TDMs between the excited, coupled system and the lower states, $| E^s \rangle$ and $| E^t \rangle$, are given as

$$(\mathsf{d}^s)_{k,i} = \langle E_k^s | \mathbf{d} \cdot \hat{\epsilon} | E_i \rangle \quad \text{and} \quad (\mathsf{d}^t)_{m,i} = \langle E_m^t | \mathbf{d} \cdot \hat{\epsilon} | E_i \rangle , \tag{6.11}$$

where $\mathbf{d}$ is the electric dipole operator and $\hat{\epsilon}$ is the polarization direction of the

emitted radiation. Using the definition of U, we can write each fully interacting eigenstates as a sum of excited singlet (S) and excited triplet (T) states

$$| E_i \rangle = \sum_{j=1}^{N_S} (U^S)_{j,i} | E_j^S \rangle + \sum_{j=1}^{N_T} (U^T)_{j,i} | E_j^T \rangle \, , \tag{6.12}$$

where the summation is over the row (j) index of each i column (here we have dropped the superfluous u and l labeling) in the U matrix. Using Eq. (6.12), we can rewrite Eq. (6.11) as

$$(\mathsf{d}^s)_{k,i} = \sum_{j=1}^{N_S} (\mathsf{d}^{s,S})_{k,j} (U^S)_{j,i} \quad \text{and} \quad (\mathsf{d}^t)_{m,i} = \sum_{j=1}^{N_T} (\mathsf{d}^{t,T})_{m,j} (U^T)_{j,i} \tag{6.13}$$

where $(\mathsf{d}^{s,S})_{k,j} = \langle E_k^s | \mathbf{d} \cdot \hat{\epsilon} | E_j^S \rangle$ and $(\mathsf{d}^{t,T})_{m,j} = \langle E_m^t | \mathbf{d} \cdot \hat{\epsilon} | E_j^T \rangle$, are the TDMs between the excited and lower singlet, and triplet, states, respectively. The diagonalizing transformation U, can now be expressed in terms of the TDMs as

$$\mathsf{U}^S = \left(\mathsf{d}^{s,S}\right)^{-1} \cdot \mathsf{d}^s \quad \text{and} \quad \mathsf{U}^T = \left(\mathsf{d}^{t,T}\right)^{-1} \cdot \mathsf{d}^t \, . \tag{6.14}$$

Note that these equations hold true for both the upper (u) and lower (l) labelled blocks. For example, when solving for U_u^S, which has dimensions of $N_s \times N_S$, it is best to take $N_s = N_S$ to ensure that $\mathsf{d}^{s,S}$ is square. In fact, the initial partition into four blocks need not be symmetric, as it is simply a convenient tool. The matrices in the two sets of equation in Eq. (6.7) will initially be of different dimensions, however, we can still proceed with their summation provided that we first expand the vector space of the smaller dimensioned equation to the same size as the large one, placing zeros in its new elements. In determining the "inverses" of non-square matrices, the system will be either over- or under-determined, and we must use mathematical optimization methods to find their pseudo-inverse [244–246] (where only the left (or right) inverse may be defined). This will yield reasonable results provided that the asymmetry of the matrices isn't too great and that their dimensionality is sufficiently large (*i.e.* $N_S \approx N_T \approx N_s \approx N_t \gg 1$).

Substituting the above form of U (Eq. (6.14)) lets us express Eq. (6.8) in terms of the physical, fully interacting, energies and the TDMs, note that the superscripts S_u and S_l will denote singlet states corresponding to their arrangement in the original

U matrix given in Eq. (6.6),

$$
\mathsf{V}^{OD} = \left\{ \left(\mathsf{d}^{s,S_u}\right)^{-1} \cdot \mathsf{d}^s \cdot \hat{\mathsf{E}}_u + \left(\mathsf{d}^{s,S_l}\right)^{-1} \cdot \mathsf{d}^s \cdot \hat{\mathsf{E}}_l - \hat{\mathsf{E}}^S \cdot \left[\left(\mathsf{d}^{s,S_u}\right)^{-1} + \left(\mathsf{d}^{s,S_l}\right)^{-1}\right] \cdot \mathsf{d}^s \right\}
$$
$$
\cdot \left\{ \left[\left(\mathsf{d}^{t,T_u}\right)^{-1} + \left(\mathsf{d}^{t,T_l}\right)^{-1}\right] \cdot \mathsf{d}^t \right\}^{-1}. \quad (6.15)
$$

Similar to the off-diagonal case, we can substitute the expressions for the U's in terms of dipole matrices for the case of the diagonal SO matrix into Eq. (6.10) to obtain

$$
\mathsf{V}^D = \left\{ \mathsf{V}^{OD\dagger} \cdot \left[\left(\mathsf{d}^{s,S_u}\right)^{-1} + \left(\mathsf{d}^{s,S_l}\right)^{-1}\right] \cdot \mathsf{d}^s + \hat{\mathsf{E}}^T \cdot \left[\left(\mathsf{d}^{t,T_u}\right)^{-1} + \left(\mathsf{d}^{t,T_l}\right)^{-1}\right] \cdot \mathsf{d}^t \right.
$$
$$
\left. - \left(\mathsf{d}^{t,T_u}\right)^{-1} \cdot \mathsf{d}^t \cdot \hat{\mathsf{E}}_u - \left(\mathsf{d}^{t,T}\right)^{-1} \cdot \mathsf{d}^t \cdot \hat{\mathsf{E}}_l \right\} \cdot \left\{ \left[\left(\mathsf{d}^{t,T_u}\right)^{-1} + \left(\mathsf{d}^{t,T_l}\right)^{-1}\right] \cdot \mathsf{d}^t \right\}^{-1}.
$$
$$
(6.16)
$$

These expressions are the desired solution for the SO matrix, given in terms of E_k and $(\mathsf{d})_{k,i}$. The energy levels, E_k, and $|(\mathsf{d})_{k,i}|^2$ are routinely measured in high resolution spectroscopy. As we have shown [247, 248], knowledge of these quantities allows us to extract the desired $(\mathsf{d})_{k,i}$ amplitudes. The remaining information needed for Eq. (6.15) is the diabatic energy levels, ($\hat{\mathsf{E}}^S$ and $\hat{\mathsf{E}}^T$), and the TDMs of the decoupled states ($\mathsf{d}^{s,S}$ and $\mathsf{d}^{t,T}$). This information can be computed from the excited, decoupled, diabatic singlet and triplet PES.

In the case of weak SOC, these potentials could be obtained from the ground electronic state and the measured $|(\mathsf{d})_{k,i}|^2$ values for vibrational states which are sufficiently removed from the (near) crossing regions [7, 125, 128, 128, 143]. Since such states will not be as affected by the SO-coupling and retain mostly their singlet or triplet character, their dipole couplings to either the ground singlet or triplet states can be used to reconstruct an accurate representation of the corresponding diabatic potential. As demonstrated by Li *et al.* [7], one is able to extract an excited PES using dipole data from only a few (≈ 5) highly excited rovibrational states of the unknown PES. After determining these PES we can calculate the singlet state rovibrational energies ($\hat{E}^S$) and, within the Franck-Condon approximation, the $\mathsf{d}^{s,S}$ and $\mathsf{d}^{t,T}$ TDMs. When the SOC is strong, and the above inversion does not work, we can either obtain diabatic singlet and triplet potentials from traditional *ab initio* calculations or use those calculated by spectroscopic methods [104, 107, 242].

Lastly, using our calculated results of the two sets of diabatic eigenstates (after

having found their potentials), we may solve Eq. (6.4) in the least-squares sense to obtain a polynomial form for the $\mathsf{V}^{OD(D)}(R)$ function. Or alternatively, we can use completeness (for details see derivation of Eq. (16) in Ref. [144]) to write Eq. (6.4) as

$$V^{OD(D)}(R) = \sum_{i,k} \phi_i^{*S}(R) V_{i,k}^{OD(D)} \phi_k^T(R) \Big/ \sum_j |\phi_j^T(R)|^2, \qquad (6.17)$$

where $\phi_j^S(R) \equiv \langle R| E_j^S \rangle$ and $\phi_j^T(R) \equiv \langle R| E_j^T \rangle$. The resulting SOC function and the known eigenvalues thus lead to the extraction of the full SOC Hamiltonian.

6.2 Results

6.2.1 Weak Coupling - NaK

In this section we describe a set of calculations where we determine the SO coupling function between low-lying electronic states of NaK [249]. We use data from Ref. [11], where it was demonstrated that for the weakly coupled $D(3)^1\Pi$ and $d(3)^3\Pi$ electronic states, the Rydberg-Klein-Rees (RKR) curves are in good agreement with experimental data and can thus be used to define our excited decoupled potentials in the diabatic representation. We have used the ground state singlet($X^1\Sigma^+$) and triplet($a^3\Sigma^+$) states of Ref. [9, 10], together with the transition dipole moments [250, 251] and the SO function [12–15] to produce realistic spectroscopic line-positions and amplitudes, ($|d_{k,i}^s|$ and $|d_{m,i}^t|$), shown in Fig. 6.1a.

We first use the decoupled potentials in the diabatic representation of Ref. [11], to calculate $\mathsf{d}^{s,S}$, the TDM matrix between the two decoupled singlets, $X^1\Sigma^+$ and $D(3)^1\Pi$, and $\mathsf{d}^{t,T}$ the TDM matrix between the two decoupled triplets, $a^3\Sigma^+$ and $d(3)^3\Pi$. Armed with these matrix elements and using a recent development (from Chap. 5 and Refs. [247, 248]) in which we have shown how to extract the signs of the d^s and d^t TDMs from their experimentally derived magnitudes, we can use Eq. (6.14) to extract the SOC eigenstates in the diabatic basis, thus leading us to determine the SOC functions. We illustrate this procedure here by extracting the SOC functions using simulated TDMs between 40 SOC excited eigenstates and two sets of low lying rovibrational eigenstates of the $X^1\Sigma^+$ and the $a^3\Sigma^+$ electronic manifolds. With all the ingredients in place, we now use Eq. (6.15), Eq. (6.16) and Eq. (6.17) to perform a point-by-point extraction of the two SOC terms. We have verified that 40 is the smallest number of states needed to maintain an accuracy of
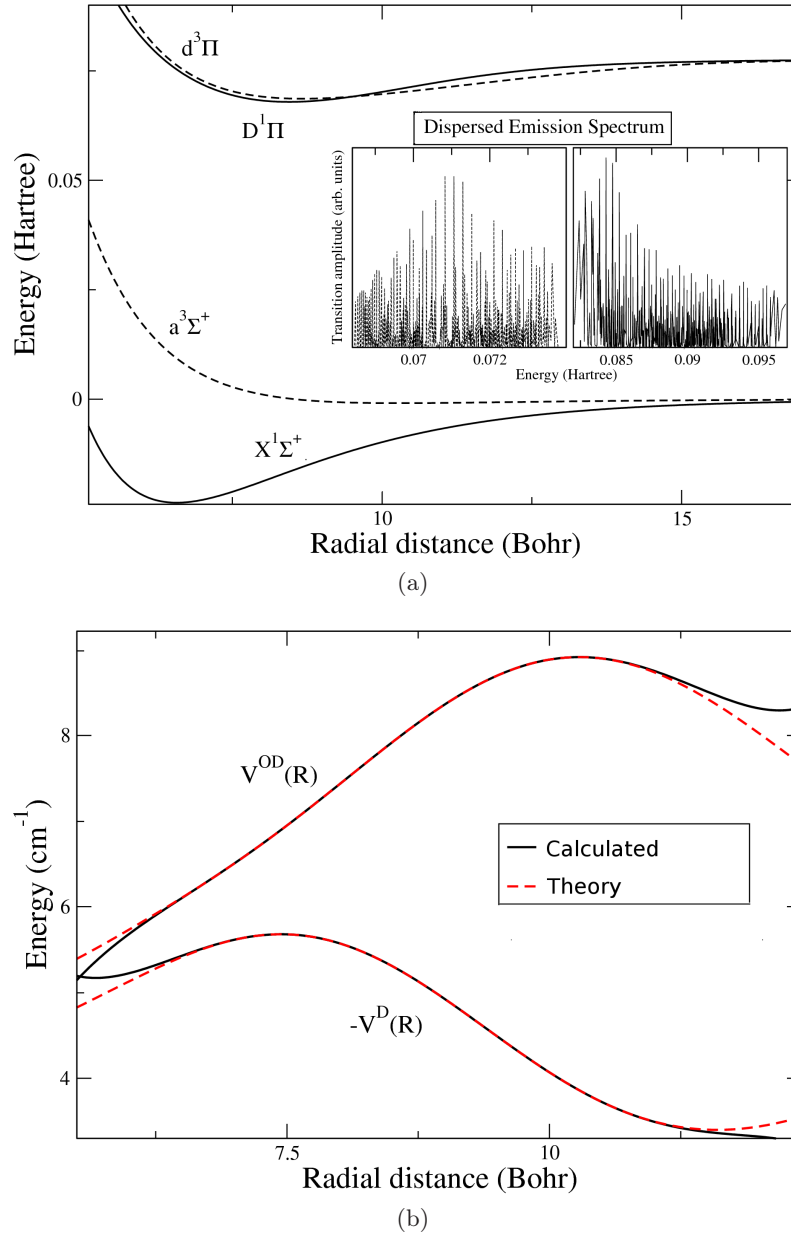
Figure 6.1: (a) (Main) Four NaK potentials in the diabatic representation: Solid lines - the $X^1\Sigma^+$ and $D(3)^1\Pi$ singlet states; dashed lines - the $a^3\Sigma^+$ and $d(3)^3\Pi$ triplet states [9–11]. (Inset) The dispersed emission spectrum from the coupled $D(3)^1\Pi/d(3)^3\Pi$ state to the lowest singlet and triplet states. (b) The "true" (Ref. [12–15]) and extracted SO functions in NaK, exhibiting good agreement for the off-diagonal ($V^{OD}(R)$) term as well as for the diagonal ($V^D(R)$) term.

$< 1\%$ in the extracted SOC functions in the (avoided-)crossing region.

The SOC extracted terms, fitted in Eq. (6.4) by a 5th order polynomial, are shown in Fig. 6.1b where excellent agreement between the "true" and extracted SOC terms is clearly in evidence. As expected, the accuracy of the extraction begins to decrease outside the region spanned by the spatial extension of the eigenfunctions included in the calculation.

6.2.2 Strong Coupling - RbCs

We now address the situation of strong SO-coupling between electronic states, occurring for example in the RbCs molecule [223–225]. To simulate the rotationless fluorescence spectrum of RbCs, we use the $X^1\Sigma^+$ and $a^3\Sigma^+$ low lying PES of Ref. [16], the $A^1\Sigma^+$ and $b^3\Pi$ excited PES in the diabatic representation of Ref. [17], the transition dipole moments of Ref. [226], and the SO functions of Ref. [18, 19] (see Fig.6.2a for diagram). Due to the strong coupling between the $A^1\Sigma^+$ and $b^3\Pi$ states, the RKR method or other inversion schemes [6, 7, 125, 128, 128, 143] fail to generate reasonable candidates for the excited potentials, so instead we use the *ab initio* diabatic potentials from Ref. [17] for this demonstration.

As in the weak coupling case we extract the SOC functions, $V^{OD}(R)$ and $V^D(R)$, from Eq. (6.15), Eq. (6.16) and Eq. (6.17), using the simulated and computed TDMs and eigenenergies. Then, we take these determined SOC functions and the diabatic eigenstates, $|E^S\rangle$ and $|E^T\rangle$, to re-generate the SO-coupling matrix, V^{OD} and V^D using Eq. (6.4). This allows us to re-create the full SOC Hamiltonian (Eq. (6.3)) from the extracted information and thus compare the calculated SOC energies (i.e. the eigenvalues of Eq. (6.3)) obtained through the extraction of the SOC coupling functions with those computed directly from the *ab initio* data.

In Fig. 6.2b we plot the percentage difference between the eigenvalues obtained in these two cases when the total number of SO eigenstates included in the calculation is varied. The comparison is performed over the SO eigenvalues that would experience the greatest energy shifts due to the coupling – those about the (avoided)-crossing region of $A^1\Sigma^+$ and $b^3\Pi$ states. We see that when too few states ($N_{SO} = \{60, 80\}$) are included in the calculation, the coupling between the potentials is not fully characterized and large errors arise in the extracted eigenvalues. However, with 120 SO eigenstates the accuracy becomes quite good ($\approx$ 1-2 cm^{-1}), and the inclusion of more functions doesn't significantly improve the results, which is good news for experimentalists who often don't have all the transition data. The oscillations seen
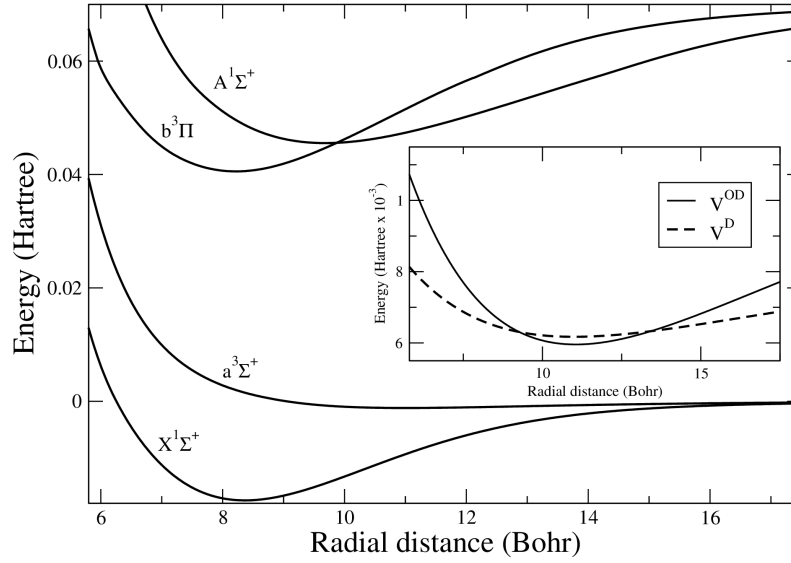
(a)
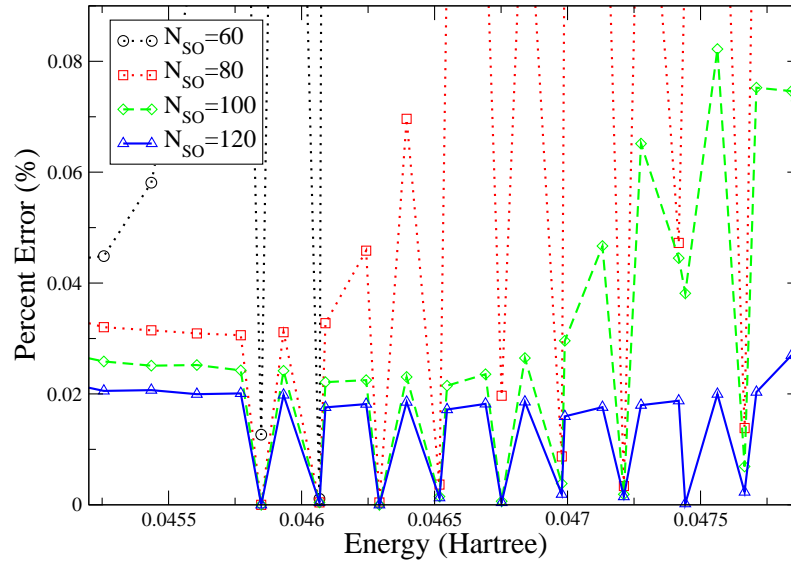
(b)

Figure 6.2: (a) (Main) Solid black lines - the Morse RbCs PES in the diabatic representation [16, 17]; (Inset) The off-diagonal ($V^{OD}(R)$) and diagonal ($V^{D}(R)$) SO functions between the diabatic potentials [18, 19]. (b) Percentage difference between the true and computed SOC eigenvalues calculated in the $A^1\Sigma^+$ and $b^3\Pi$ diabatic crossing region, for a different number of total included eigenvalues.

in the results are due to changes in the singlet-triplet composition of the different SO-eigenstates. We suspect that those states comprising of more triplet character have greater errors due to the additional diagonal coupling term, V^D, being computed in the extraction.

This demonstrates that we can accurately characterized the coupling between the $W^S(R)$ ($A^1\Sigma^+$) and $W^T(R)$ ($b^3\Pi$) potentials such that we can express the SO coupled eigenstates in the $W^{S/T}(R)$ basis states, enabling the accurate imaging of excited wave packets in non-adiabatically coupled systems [217].

6.3   Conclusion

We have performed a point-by-point extraction of the SO-coupling as a function of the nuclear coordinates R using experimental data. Knowledge of the R dependence of these coupling terms enables the generation of the eigenstates of the coupled system and the reconstruction of excited wave packets generated in ultrashort pulse excitation experiments [217]. The procedure uses a formula that expresses the spin orbit coupling matrix in terms of the TDMs and the fully interacting energy levels.

Our method is not limited to this type of interaction: any interaction between electronic states can be extracted in a similar manner. We intend to apply this method to the mapping of non-adiabatic effects, including conical intersections, in polyatomic molecules.

Chapter 7

Final Conclusions

We have outlined several original approaches for extracting molecular information from spectroscopic data. With the increasing breadth of spectral information and improvements in temporal and spatial resolutions, original techniques such as those presented here, may help to better characterize a molecule's structure and behavior. There are now many avenues of research in the molecular sciences, all of which however, require as detailed information as possible on the molecular species at hand. For instances, the formation of ultracold molecules (*e.g.* via the photoassociation of ultracold atoms) relies on accurate molecular information and internal level structure and dynamics. In particular, this requires very good information near the dissociation limit for Feshbach resonances, and accurate knowledge of strongly mixed (singlet-triplet) complexes for transferring molecules to bound states via Raman process. A good description of a system would facilitate studying the properties of molecules such as in: Bose-Einstein condensates and Fermi degenerate gases [25], controlling chemical reactions and collisions [252], and, the quantum computation on aligned molecular dipoles [157]. There has been even been renewed interest in the usage of heteronuclear diatomics for sensitive non-contact probing and mapping of external electric field distribution via changes in LIF [253, 254] to which precise state information would be essential.

The first method involves determining one of the most important concepts of molecular physics [48], the potential energy surface (PES). These structures are fundamental to spectroscopy, chemical kinetics and to the study of the bulk properties of matter. It is used as a concept for both qualitative and quantitative description of molecular properties. Our approach is capable of extracting excited diatomic potentials over energy ranges spanning thousands of wave numbers using only transition spectral data from a few (~ 10) excited rovibrational states. We developed our procedure to include transition information to/from continuum states, address multidimensional surfaces and operate beyond the Franck-Condon approximation (FCA). The ten-fold improvements in accuracy observed when including a dipole

correction is also applicable to any other inversion scheme which are based on the FCA (such as those of Avisar and Tanner [153, 154]). The key requirements for a successful PES construction are, first, sufficient data with reasonably small error bars of relative intensities ($\sim 5\%$) Ref. [143], and next, fulfillment of the completeness condition in order to expand the excited state rovibrational wave function in terms of the ground state wave functions (Ref. [128]). Recently, there have been interesting studies measuring the transition dipole moments over a wide range of transition frequencies to very high accuracy (e.g. Ref. [33] by Dutta *et al*). These studies would serve as a good source for future work to validate our method using experimental data.

On route to inverting the PESs we solved the spectroscopic phase problem. Whereas the magnitudes of the transition dipole matrix elements (TDMe) between energy eigenstates can be deduced from the strength of frequency-resolved spectral lines, yielding the absolute-value-squared of the TDMs, it has much more difficult to use such data to determine the phases of the TDMs. This current approach, however, fails when there exist couplings between the unknown potentials, for instance, due to spin-orbit coupling (SOC). In molecules, SOC causes inter-system crossings (ISC), the nonradiative transition between different spin (e.g., singlet and triplet) states [235]. SOC also gives rise to the formation of "doorway" or "window" states [236], called such, because they enable electric-dipole-induced optical transitions between different spin states. Its determination is vital for many applications, such as the laser cooling of molecular species, which leads towards the formation of Bose-Einstein condensates. In RbCs, SOC is known to promote Feshbach type resonances [237–239] and to affect the "permanent" dipole moment of this molecule, allowing for the tuning of the (dipole-dipole) interactions between trapped RbCs molecules, potentially enabling the performance of quantum simulations in such systems. Using a simulated frequency spectrum of a spin-coupled diatomic system, we have demonstrated the extraction of these coupling matrix elements, as well as, their radial functional dependence. This work opens the door for extracting PESs in the presense of non-adiabatic couplings.

We have also shown how the amplitudes of the electronic TDMs linking the excited and ground rovibrational states, in addition, to the amplitude of time-evolving wave packets can be found from time resolved fluorescence data. By assuming that the time-dependent decay signal is given as $R(t) = \sum_{s',s} a_{s'}^* a_s C_{s',s} \exp(-i\omega_{s',s}t)$, where a_s are the desired expansion coefficients, $\omega_{s',s}$ are (known) *beat* frequencies,

and $C_{s',s}$ are molecular response matrix elements, we have shown how a finite time Fourier transform over the fluorescence data at a given beat frequency will extract out the component of the signal pertaining to the bi-linear $a_{s'}^* a_s$ product. Using this result which assumes knowledge of the amplitudes *and* phases of $\mu_{s,f}$ (the individual transition-dipole matrix-elements (TDMs) between energy eigenstates), one can derive the phases as well as the amplitudes of the a_s expansion coefficients of a wave packet $\Psi(\mathbf{r}, t) = \sum_s a_s \psi_s(\mathbf{r}) \exp(-iE_s t/\hbar)$, where $\psi_s(\mathbf{r})$ are vibrational eigenfunctions. We have demonstrated these imaging results in basic diatomic systems, and also applied this technique to SOC systems where we have seen very clearly how a wave packet, which starts out in the singlet state region, leaks out to the triplet state after several picoseconds.

Although we have shown that for an electronic transition between two Born-Oppenheimer potential energy surfaces (PES), knowledge of one PES allows one to derive the other PES, and the TDM's phases [128, 143, 144], as well as imaging of unknown time-evolving wave packets [176, 177, 217], the method requires data of a large number of spectral lines and of sufficient quality and completeness, which at this stage is only slowly becoming available [33]. Since obtaining the amplitudes of the electronic TDMs linking the excited and ground vibrational states, is the crucial step in both the PES inversion and wavepacket imaging procedures, we developed an alternative approach for their determination. First, we discussed how a semiclassical stationary phase calculation does not give the unknown phases of the TDMs when the wavefunction of the excited state is unknown. Then, we presented an original approach using ultrashort pulses in the molecule-field interaction. The method is based on using bichromatic coherent control (BCC), which uses quantum interferences between different pairs of transitions induced by two external laser fields to coherently deplete the population of (hence the fluorescence from) different pairs of the excited energy eigenstates. The BCC induced depletion is supplemented by the Fourier transform technique on the time-dependent spontaneously emission data to obtain the sign relation between pair of TDMs. Armed with this combined information, of all pairs of sign relations between TDMs, one can conclusively extract the individual phases of the TDMs.

Our various methods, which in general, are found to be quite robust against errors can be readily generalized to other systems, such as *polyatomic* molecules. It would be interesting to apply our work to multi-dimensional problems and to use our procedures to obtained a detailed image of nuclear motions associated with *"in-*

ternal conversions" (transitions between different electronic states of the same spin multiplicity), and *"intersystem crossings"* (transitions between electronic states of different spins). More effort can be put towards the treatment of curve crossing situations, particularly in the case of singlet/triplet interactions. These coupled systems greatly alter structure of both high-resolution and time-resolved spectroscopy, and play a central role in exciting topics such as photosynthesis, where phosphorescence decay times occur on the order of minutes to hours.

Bibliography

[1] J. Brown and A. Carrington, editors. *Rotational Spectroscopy of Diatomic Molecules.* Cambridge University Press, Cambridge, United Kingdom, 2003.

[2] J. M. Merritt, V. E. Bondybey, and M. C. Heaven. Beryllium dimer: Caught in the act of bonding. *Science*, 324(5934):1548–1551, 2009.

[3] W. Demtröder, editor. *Molecular Physics.* Wiley VCH, Weinheim, Germany, 2005.

[4] T. Koyama, M. Nakajima, and T. Suemoto. Nuclear wave-packet oscillations at the F center in KCl and RbCl. *Phys. Rev. B*, 78:155126, 2008.

[5] C. H. Kim and T. Joo. Ultrafast time-resolved fluorescence by two photon absorption excitation. *Opt. Express*, 16(25):20742–20747, 2008.

[6] X. Li and M. Shapiro. Inversion of two-dimensional potentials from frequency-resolved spectroscopic data. *J. Chem. Phys.*, 134(9):094113, 2011.

[7] X. Li and M. Shapiro. The dipole correction method for extracting excited state potentials and electronic transition dipoles from fluorescence data. *Isr. J. Chem.*, 52(5):407–413, 2012.

[8] P. Kowalczyk, C. Radzewicz, J. Mostowski, and I.A. Walmsley. Time-resolved luminescence from coherently excited molecules as a probe of molecular wave-packet dynamics. *Phys. Rev. A*, 42:5622–5626, 1990.

[9] S. Eckel, S. Ashman, and J. Huennekens. Spin-orbit coupling of the NaK $3^3\Pi$ and $3^1\Pi$ states: Determination of the coupling constant and observation of quantum interference effects. *J. Mol. Spectrosc.*, 242:182–194, 2007.

[10] S. Magnier, M. Aubert-Frécon, and Ph. Millié. Potential Energies, Permanent and Transition Dipole Moments for Numerous Electronic Excited States of NaK. *J. Mol. Spectrosc.*, 200:96–103, 2000.

[11] E.A. Pazyuk, A.V. Stolyarov, A. Zaitsevskii, R. Ferber, P. Kowalczyk, and C. Teichteil. Spin-orbit coupling in the $D^1\Pi \sim d^3\Pi$ complex of $^{23}Na^{39}K$. *Mol. Phys.*, 96:955–961, 1999.

[12] A. Drozdova, A. Ross, A. Stolyarov, W. Jastrzebski, and P. Kowalczyk. Coupled-Channel analysis of the $D^1\Pi$ - $d^3\Pi$ complex in NaK : potential energy curves and spin-orbit function. In *Proceedings of the 65th Meeting of the International Symposium On Molecular Spectroscopy*, June 2010.

[13] P. Kowalczyk. Perturbation facilitated observation of the $d^3\Pi$ state in NaK. *J. Mol. Spectrosc.*, 136:1, 1989.

[14] A. Adohi-Krou, W. Jastrzebski, P. Kowalczyk, A.V. Stolyarov, and A.J. Ross. Investigation of the $D^1\Pi$ state of NaK by polarisation labelling spectroscopy. *J. Mol. Spectrosc.*, 250(1):27 – 32, 2008.

[15] A.N. Drozdova, A.V. Stolyarov, W. Jastrzebski, P. Kowalczyk, and A.J. Ross. Coupled-Channel Treatment of the $D^1\Pi$ - $d^3\Pi(e^3\Sigma^+)$ complex in NaK to determine potential energy curves and spin-orbit function. In *Proceedings of the Twenty-second Colloquium on High Resolution Molecular Spectroscopy*, August 2011.

[16] O. Docenko, M. Tamanis, R. Ferber, H. Knöckel, and E. Tiemann. Singlet and Triplet Potentials of the Ground-state Atom Pair Rb + Cs Studied by Fourier-transform Spectroscopy. *Phys. Rev. A*, 83:052519, 2011.

[17] T. Bergeman, C. E. Fellows, R. F. Gutterres, and C. Amiot. Analysis of Strongly Coupled Electronic States in Diatomic Molecules: Low-lying Excited States of RbCs. *Phys. Rev. A*, 67:050501, 2003.

[18] S. Ghosal, R.J. Doyle, C.P. Koch, and J. M. Hutson. Stimulating the Production of Deeply Bound RbCs Molecules with Laser Pulses: The Role of Spin-orbit Coupling in Forming Ultracold Molecules. *New J. Phys.*, 11(5):055011, 2009.

[19] O. Docenko, M. Tamanis, R. Ferber, T. Bergeman, S. Kotochigova, A. V. Stolyarov, Andreia de Faria Nogueira, and C. E. Fellows. Spectroscopic Data, Spin-orbit Functions, and Revised Analysis of Strong Perturbative Interactions for the $A\,^1\Sigma^+$ and $b\,^3\Pi$ States of RbCs. *Phys. Rev. A*, 81:042511, 2010.

[20] M. Tsubouchi, A. Khramov, and T. Momose. Rovibrational wave-packet manipulation using shaped midinfrared femtosecond pulses. *Phys. Rev. A*, 77:023405, 2008.

[21] M. Tsubouchi and T. Momose. Rovibrational wave-packet manipulation using shaped midinfrared femtosecond pulses toward quantum computation: Optimization of pulse shape by a genetic algorithm. *Phys. Rev. A*, 77:052326, 2008.

[22] S. Zhdanovich, A. A. Milner, C. Bloomquist, J. Floss, I. Sh. Averbukh, J. W. Hepburn, and V. Milner. Control of Molecular Rotation with a Chiral Train of Ultrashort Pulses. *Phys. Rev. Lett.*, 107(24), 2011.

[23] K. W. Madison, Y. Q. Wang, A. M. Rey, and K. Bongs, editors. *Annual Review of Cold Atoms and Molecules - Volume 1*. World Scientific, 2013.

[24] M. Lemeshko, R. V. Krems, J. M. Doyle, and S. Kais. Manipulation of molecules with electromagnetic fields. *Mol. Phys.*, 111(12-13):1648–1682, 2013.

[25] L. D. Carr, D. DeMille, R. V. Krems, and J. Ye. Cold and ultracold molecules: science, technology and applications. *New J. Phys.*, 11(5):055049, 2009.

[26] P.F. Bernath and S. McLeod. DiRef, A Database of References Associated with the Spectra of Diatomic Molecules. *J. Mol. Spectrosc.*, 207:287, 2001.

[27] M. Viteau, A. Chotia, M. Allegrini, N. Bouloufa, O. Dulieu, D. Comparat, and P. Pillet. Optical pumping and vibrational cooling of molecules. *Science*, 321(5886):232–234, 2008.

[28] E. R. Hudson, N. B. Gilfoy, S. Kotochigova, J. M. Sage, and D. DeMille. Inelastic collisions of ultracold heteronuclear molecules in an optical trap. *Phys. Rev. Lett.*, 100:203201, 2008.

[29] J. van Veldhoven, H. L. Bethlem, and G. Meijer. AC electric trap for ground-state molecules. *Phys. Rev. Lett.*, 94:083001, 2005.

[30] J. Deiglmayr, A. Grochola, M. Repp, K. Mörtlbauer, C. Glück, J. Lange, O. Dulieu, R. Wester, and M. Weidemüller. Formation of ultracold polar molecules in the rovibrational ground state. *Phys. Rev. Lett.*, 101:133004, 2008.

[31] P. Zabawa, A. Wakim, A. Neukirch, C. Haimberger, N. P. Bigelow, A. V. Stolyarov, E. A. Pazyuk, M. Tamanis, and R. Ferber. Near-dissociation photoassociative production of deeply bound NaCs molecules. *Phys. Rev. A*, 82:040501, 2010.

[32] P. Staanum, A. Pashov, H. Knöckel, and E. Tiemann. $X^1\Sigma^+$ and $a^3\Sigma^+$ states of LiCs studied by Fourier-transform spectroscopy. *Phys. Rev. A*, 75:042513, 2007.

[33] S. Dutta, A. Altaf, D.S. Elliott, and Y. P. Chen. Laser spectroscopy of the $X^1\Sigma^+$ and $B^1\Pi$ states of the LiRb molecule. *Chem. Phys. Lett.*, 511(1âĂŞ3):7 − 11, 2011.

[34] I. N. Levine, editor. *Quantum Chemistry.* Prentice-Hall, Englewood Cliffs, NJ, 1991.

[35] F. O. Ellison. A method of diatomics in molecules I. general theory and application to H_2O. *J. Am. Chem. Soc.*, 85(22):3540–3544, 1963.

[36] J. C. Tully. Diatomics-in-molecules potential energy surfaces. i. first-row triatomic hydrides. *J. Chem. Phys.*, 58(4):1396–1410, 1973.

[37] B. Kendrick and R. T. Pack. Potential energy surfaces for the low-lying $^2A''$ and $^2A'$ States of HO_2: Use of the diatomics in molecules model to fit ab initio data. *J. Chem. Phys.*, 102(5):1994–2012, 1995.

[38] X. Li, D. A. Brue, and G. A. Parker. Potential energy surfaces for the $1^4A'$, $2^4A'$, $1^4A''$, and $2^4A''$ states of Li_3. *J. Chem. Phys.*, 129(12):124305, 2008.

[39] A Derkatch, C Lundevall, L.-E Berg, and P Royen. Lifetime measurements of the $A^2\Pi$ state of BaCl using laser spectroscopy. *Chem. Phys. Lett.*, 332(3-4):278 − 282, 2000.

[40] P. J. Dagdigian, H. W. Cruse, and R. N. Zare. Radiative lifetimes of the alkaline earth monohalides. *J. Chem. Phys.*, 60(6):2330–2339, 1974.

[41] M. A. Ratner. Chemical applications of ultrafast spectroscopy, By Graham R. Fleming, Oxford, New York, 1986. *Int. J. Quant. Chem.*, 31(6):989–989, 1987.

[42] U. Buck. Inversion of molecular scattering data. *Rev. Mod. Phys.*, 46(2), 1974.

[43] R. E. Burge, M. A. Fiddy, M. Nieto-Vesperinas, and M. W. L. Wheeler. The phase problem in scattering theory: the zeros of entire functions and their significance. *Proc. R. Soc. London Ser. A*, 360:25–45, 1978.

[44] H. Nussenzveig. Phase problem in coherence theory. *J. Math. Phys.*, 8, 1967.

[45] J. Tellinghuisen, M. R. McKeever, and A. Sur. Reanalysis of the D-X fluorescence spectrum of I2. *J. Mol. Spectrosc.*, 82(2):225–245, 1980.

[46] J. Tellinghuisen. On the efficiency and accuracy of quantum and classical methods of calculating diatomic spectra. *J. Chem. Phys.*, 80:5472, 1984.

[47] G. Herzberg, editor. *Molecular spectra and molecular structure.* Van Nostrand Reinhold, New York, 1950.

[48] H. Lefebvre-Brion and R. W. Field. *The Spectra and Dynamics of Diatomic Molecules.* Elsevier/Academic, Amsterdam, 1st edition, 2004.

[49] F. Hund. On the interpretation of some appearances in the molecular spectra. *Z. Phys.*, 36:657, 1926.

[50] R. G. Newton, editor. *Scattering Theory of Waves and Particles.* Springer-Verlag, New York, 2nd edition, 1982.

[51] M. Shapiro. Dynamics of dissociation I. computational investigation of unimolecular breakdown processes. *J. Chem. Phys.*, 56(6):2582–2591, 1972.

[52] M Shapiro and R Bersohn. Theories of the dynamics of photodissociation. *Annu. Rev. Phys. Chem.*, 33(1):409–442, 1982.

[53] A. G. Abrashkevich and M. Shapiro. Photoionization of two-electron atoms via the hyperspherical artificial-channel method: Application to H^- and He. *Phys. Rev. A*, 50:1205–1217, 1994.

[54] J. von Neumann and E.P. Wigner. Über das verhalten von eigenwerten bei adiabatischen prozessen. *Z. Physik*, 30:467, 1929.

[55] F. Hund. On the interpretation of molecular spectra: I. *Z. Phys.*, 40:742, 1927.

[56] J. Z. H. Zhang, editor. *Theory and Application of Quantum Molecular Dynamics.* World Scientific, Singapore, 1999.

[57] H. A. Jahn and E. Teller. Stability of Polyatomic Molecules in Degenerate Electronic States. I. Orbital Degeneracy. *Proceedings of the Royal Society of London. Series A - Mathematical and Physical Sciences*, 161(905):220–235, 1937.

[58] R. Renner. On the theory of the interaction between electronic and nuclear motion of three-atomic bar-shaped molecules. *Z. Phys.*, 92:172, 1934.

[59] J. G. Parker. Comparison of experimental and theoretical vibrational relaxation times for diatomic gases. *J. Chem. Phys.*, 41(6):1600–1609, 1964.

[60] R. N. Schwartz, Z. I. Slawsky, and K. F. Herzfeld. Calculation of vibrational relaxation times in gases. *J. Chem. Phys.*, 20(10):1591–1599, 1952.

[61] W.O. Feikema, P. Gast, I.B. Klenina, and I.I Proskuryakov. EPR characterization of the triplet state in photosystem II reaction centers with singly reduced primary acceptor QA. *Biochemica et Biophysica Acta*, 1709:105, 2005.

[62] O. Svelto and D. Hanna, editors. *Principles of Lasers.* Springer Science, New York, NY, 4th edition, 1998.

[63] R. L. Fork, C. H. Brito Cruz, P. C. Becker, and C. V. Shank. Compression of optical pulses to six femtoseconds by using cubic phase compensation. *Opt. Lett.*, 12(7):483–485, 1987.

[64] A. M. Weiner. Femtosecond pulse shaping using spatial light modulators. *Review of Scientific Instruments*, 71(5):1929–1960, 2000.

[65] D. W. Pinkham. *Eigenschaften Angeregter Zustände der Alkalidimeren Li_2, Na_2 und NaLi Sowie deren Kationen aus Ab-Initio-Rechnungen.* PhD thesis, University of Virginia, Charlottesville, VA, 2008.

[66] P. Brumer and M. Shapiro. Control of unimolecular reactions using coherent control. *Chem. Phys. Lett.*, 126:541–546, 1986.

[67] D.J. Tannor and S.A. Rice. Control of selectivity of chemical reaction via control of wave packet evolution. *J. Chem. Phys.*, 83:5013, 1985.

[68] N. Dudovich, D. Oron, and Y. Silberberg. Single-pulse coherently controlled nonlinear raman spectroscopy and microscopy. *Nature*, 418:512–514, 2002.

[69] D. Meshulach and Y. Silberberg. Coherent quantum control of two-photon transitions by a femtosecond laser pulse. *Nature*, 396:239–242, 1998.

[70] D. Meshulach and Y. Silberberg. Coherent quantum control of multiphoton transitions by shaped ultrashort optical pulse. *Phys. Rev. A*, 60:1287–1292, 1999.

[71] A. Weber. *High-resolution Raman Spectroscopy of Gases*. John Wiley & Sons, Ltd, 2011.

[72] S. Gerstenkom and P. Luc. Description of the absorption spectrum of iodine recorded by means of Fourier Transform Spectroscopy : the (B-X) system. *J. Phys. France*, 46(6):867–881, 1985.

[73] A. Stein, A. Pashov, P. F. Staanum, H. Knöckel, and E. Tiemann. The $B^1\Pi$ and $D^1\Pi$ states of LiCs studied by Fourier-transform spectroscopy. *The European Physical Journal D*, 48(2):177–185, 2008.

[74] H. Graener, J. W. Nibler, and A. Laubereau. Picosecond coherent anti-Stokes Raman spectroscopy of molecules in free jet expansions. *Opt. Lett.*, 9(5):165–167, 1984.

[75] T. J. Dunn, J. N. Sweetser, I. A. Walmsley, and C. Radzewicz. Experimental determination of the dynamics of a molecular nuclear wave packet via the spectra of spontaneous emission. *Phys. Rev. Lett.*, 70:3388–3391, 1993.

[76] S. Kotochigova and E. Tiesinga. Ab initio relativistic calculation of the RbCs molecule. *J. Chem. Phys.*, 123(17), 2005.

[77] E. Ahmed, A. Hansson, P. Qi, T. Kirova, A. Lazoudis, S. Kotochigova, A. M. Lyyra, L. Li, J. Qi, and S. Magnier. Measurement of the electronic transition dipole moment by Autler-Townes splitting: Comparison of three- and four-level excitation schemes for the Na$_2$ $A^1\Sigma_u^+$-$X^1\Sigma_g^+$ system. *J. Chem. Phys.*, 124(8), 2006.

[78] J. L. Dunham. The Wentzel-Brillouin-Kramers method of solving the wave equation. *Phys. Rev.*, 41:713–720, 1932.

[79] E. Tiemann, H. Arnst, W.U. Stieda, T. Tõrring, and J. Hoeft. Observed adiabatic corrections to the born-oppenheimer approximation for diatomic molecules with ten valence electrons. *Chem. Phys.*, 67(2):133 – 138, 1982.

[80] J. Y. Seto, R. J. Le Roy, J. Verges, and C. Amiot. Direct potential fit analysis of the $X^1\Sigma_g^+$ state of Rb$_2$: Nothing else will do! *J. Chem. Phys.*, 113(8):3067–3076, 2000.

[81] R. J. Le Roy, Y. Huang, and C. Jary. An accurate analytic potential function for ground-state N$_2$ from a direct-potential-fit analysis of spectroscopic data. *J. Chem. Phys.*, 125(16):164310, 2006.

[82] A. L. G. Rees. The calculation of potential-energy curves from band-spectroscopic data. *Proceedings of the Physical Society*, 59(6):998, 1947.

[83] O. Klein. For the calculation of potential curves for diatomic molecules with spectral help. *Z. Phys.*, 76:226, 1932.

[84] R. Rydberg. Graphical representation of some bound spectroscopic results. *Z. Phys.*, 73:376, 1932.

[85] R. Rydberg. Some potential curves of mercury hydrides. *Z. Phys.*, 80:514, 1933.

[86] A.W. Mantz, James K.G. Watson, K.Narahari Rao, D.L. Albritton, A.L. Schmeltekopf, and R.N. Zare. Rydberg-Klein-Rees potential for the $X^1\Sigma^+$ state of the CO molecule. *Journal of Molecular Spectroscopy*, 39(1):180–184, 1971.

[87] R. J. LeRoy. `RKR1`: A computer program to calculate the potential energy curve. *U. Waterloo Chem. Phys. Research Report*, CP-657R, 2004.

[88] R.B. Gerber, R.M. Roth, and M.A. Ratner. Approximate inversion method for obtaining polyatomic potential energy surfaces from ro-vibrational spectra. *Mol. Phys.*, 44(6):1335–1353, 1981.

[89] R. M. Roth, M. A. Ratner, and R. B. Gerber. Inversion of polyatomic rovibration spectra into a molecular potential energy surface: Application to CO$_2$. *Phys. Rev. Lett.*, 52:1288–1291, 1984.

[90] H. Romanowski, R. B. Gerber, and M. A. Ratner. The anharmonic stretching-bending potential of CO$_2$ from inversion of spectroscopic data. *J. Chem. Phys.*, 88(11):6757–6767, 1988.

[91] D. J. Nesbitt, M. S. Child, and D. C. Clary. Rydberg–Klein–Rees inversion of high resolution van der Waals infrared spectra: An intermolecular potential energy surface for Ar+HF (v=1). *J. Chem. Phys.*, 90(9):4855–4864, 1989.

[92] K. Shimizu and F. Shimizu. Laser induced fluorescence spectra of the a $^3\Pi_u$-X$^1\Sigma_g^+$ band of Na$_2$ by molecular beam. *J. Chem. Phys.*, 78(3):1126–1131, 1983.

[93] M. R. Manaa, A. J. Ross, F. Martin, P. Crozet, A. M. Lyyra, L. Li, C. Amiot, and T. Bergeman. Spin-Orbit Interactions, New Spectral Data and Deperturbation of the Coupled b$^3\Pi_u$ and A$^1\Sigma^+$ States of K$_2$. *J. Chem. Phys.*, 117:11208, 2002.

[94] J. Zaharova, M. Tamanis, R. Ferber, A. N. Drozdova, E. A. Pazyuk, and A. V. Stolyarov. Solution of the fully-mixed-state problem: Direct deperturbation analysis of the A$^1\Sigma^+\tilde{b}^3\Pi$ complex in a NaCs dimer. *Phys. Rev. A*, 79:012508, 2009.

[95] J. Bai, E. H. Ahmed, B. Beser, Y. Guan, S. Kotochigova, A. M. Lyyra, S. Ashman, C. M. Wolfe, J. Huennekens, Feng Xie, Dan Li, Li Li, M. Tamanis, R. Ferber, A. Drozdova, E. Pazyuk, A. V. Stolyarov, J. G. Danzl, H.-C. Nägerl, N. Bouloufa, O. Dulieu, C. Amiot, H. Salami, and T. Bergeman. Global analysis of data on the spin-orbit-coupled A$^1\Sigma_u^+$ and b$^3\Pi_u$ states of Cs$_2$. *Phys. Rev. A*, 83:032514, 2011.

[96] P. Qi, J. Bai, E. Ahmed, A. M. Lyyra, S. Kotochigova, A. J. Ross, C. Effantin, P. Zalicki, J. Vigué, G. Chawla, R. W. Field, T.-J. Whang, W. C. Stwalley, H. Knöckel, E. Tiemann, J. Shang, L. Li, and T. Bergeman. New spectroscopic data, spin-orbit functions, and global analysis of data on the A$^1\Sigma^+$ and b$^3\Pi_u$ states of Na$_2$. *J. Chem. Phys.*, 127(4):–, 2007.

[97] C. Effantin, O. Babaky, K. Hussein, J. d'Incan, and R. F. Barrow. Interactions between A$^1\Sigma_u^+$ and b$^3\Pi_u$ states of Na$_2$. *J. Phys. B: At. Mol. Phys.*, 18(20):4077, 1985.

[98] W. M. Kosman and J. Hinze. Inverse perturbation analysis: Improving the accuracy of potential energy curves. *J. Mol. Spectrosc.*, 56(1):93 – 103, 1975.

[99] C.R. Vidal and H. Scheingraber. Determination of diatomic molecular constants using an inverted perturbation approach: Application to the $A^1\Sigma_u^+$-$X^1\Sigma_g^+$ system of Mg_2. *J. Mol. Spectrosc.*, 65(1):46 – 64, 1977.

[100] A. Pashov, W. Jastrzębski, W. Jaśniecki, V. Bednarska, and P. Kowalczyk. Accurate Potential Curve for the Double Minimum $2^1\Sigma_u^+$ State of Na_2. *J. Mol. Spectrosc.*, 203(2):264 – 267, 2000.

[101] V.S. Ivanov and V.B. Sovkov. An IPA procedure for bound-continuum diatomic transition intensities. *Chem. Phys.*, 213(1-3):295 – 301, 1996.

[102] R. Baer and R. Kosloff. Obtaining the excited-state potential by inversion of photodissociation absorption spectra. *Chem. Phys. Lett.*, 200(1-2):183 – 191, 1992.

[103] D. H. Zhang and J. C. Light. Potential inversion via variational generalized inverse. *J. Chem. Phys.*, 103(22):9713–9720, 1995.

[104] J. A. Coxon and C. S. Dickinson. Application of direct potential fitting to line position data for the $X^1\Sigma^+$ and $A^1\Sigma^+$ states of LiH. *J. Chem. Phys.*, 121(19):9378–9388, 2004.

[105] J. A. Coxon and P. G. Hajigeorgiou. Direct potential fit analysis of the $X^1\Sigma^+$ ground state of CO. *J. Chem. Phys.*, 121(7):2992–3008, 2004.

[106] H. Salami, T. Bergeman, B. Beser, J. Bai, E. H. Ahmed, S. Kotochigova, A. M. Lyyra, J. Huennekens, C. Lisdat, A. V. Stolyarov, O. Dulieu, P. Crozet, and A. J. Ross. Spectroscopic observations, spin-orbit functions, and coupled-channel deperturbation analysis of data on the $A^1\Sigma_u^+$ and $b^3\Pi_u$ states of Rb_2. *Phys. Rev. A*, 80:022515, 2009.

[107] N. S. Dattani and R. J. Le Roy. A DPF data analysis yields accurate analytic potentials for and that incorporate 3-state mixing near the state asymptote. *J. Mol. Spectrosc.*, 268(1-2):199 – 210, 2011.

[108] R. J. LeRoy, J. Seto, and Y. Huang. `DpotFit1.2`: A Computer Program for Fitting Diatomic Molecule Spectra to Potential Energy Functions. *U. Waterloo Chem. Phys. Research Report*, CP-664, 2007.

[109] A. Grochola, A. Pashov, J. Deiglmayr, M. Repp, E. Tiemann, R. Wester, and M. Weidemuller. Photoassociation spectroscopy of the B$^1\Pi$ state of LiCs. *J. Chem. Phys.*, 131(5):054304, 2009.

[110] P. G. Hajigeorgiou and R. J. Le Roy. A "modified Lennard-Jones oscillator" model for diatom potential functions. *J. Chem. Phys.*, 112(9):3949–3957, 2000.

[111] M. Molski. Extension of dunham's analytic treatment of highly resolved infrared and microwave spectra of diatomic molecules. *J. Phys. Chem. A*, 103(27):5269–5274, 1999.

[112] M. Semczuk, X. Li, W. Gunton, M. Haw, N. S. Dattani, J. Witz, A. K. Mills, D. J. Jones, and K. W. Madison. High-resolution photoassociation spectroscopy of the ^{6}Li$_2$ $1^3\Sigma_g^+$ state. *Phys. Rev. A*, 87:052505, 2013.

[113] C. Samuelis, E. Tiesinga, T. Laue, M. Elbs, H. Knöckel, and E. Tiemann. Cold atomic collisions studied by molecular spectroscopy. *Phys. Rev. A*, 63:012710, 2000.

[114] M.S. Child and M. Shapiro. Photodissociation and the Condon reflection principle. *Mol. Phys.*, 48(1):111–128, 1983.

[115] G. Aravind A. K. Gupta and M. Krishnamurthy. Probing potential energy curves of C$_2$- by translational energy spectroscopy. *Phys. Rev. A*, 69:035201, 2004.

[116] A. K. Gupta G. Aravind and M. Krishnamurthy. An experimental study on electronic excited states of O$_2$. *Chem. Phys. Lett.*, 424:252, 2006.

[117] E. Steiner, P. R. Certain, and P. J. Kuntz. Extended diatomics in molecules calculations. *J. Chem. Phys.*, 59(1):47–55, 1973.

[118] C. W. Eaker and C. A. Parr. Optimization of diatomic state mixing in diatomics-in-molecules theory: The CH$_n$ potential-energy surfaces. *J. Chem. Phys.*, 64(4):1322–1332, 1976.

[119] P.J. Kuntz and J. Valldorf. A DIM model for homogeneous noble gas ionic clusters. *Z. Phys. D.*, 8:195, 1998.

[120] A. Pashov, W. Jastrzębski, and P. Kowalczyk. Construction of potential curves for diatomic molecular states by the IPA method. *Comp. Phys. Comm.*, 128(3):622 – 634, 2000.

[121] T.-S. Ho and H. Rabitz. On the inversion of atomic scattering data: A new algorithm based on functional sensitivity analysis. *J. Chem. Phys.*, 91(12):7590–7605, 1989.

[122] T. S. Ho and H. Rabitz. Inversion of experimental data to extract intermolecular and intramolecular potentials. *J. Phys. Chem.*, 97(51):13447–13456, 1993.

[123] T.-S. Ho, H. Rabitz, S. E. Choi, and M. I. Lester. An inverse method for obtaining smooth multidimensional potential energy surfaces: application to Ar+OH. *J. Chem. Phys.*, 102(5):2282–2285, 1995.

[124] R. B. Gerber, M. Shapiro, U. Buck, and J. Schleusener. Quantum-mechanical inversion of the differential cross section: Determination of the He-Ne potential. *Phys. Rev. Lett.*, 41:236–239, 1978.

[125] M. Shapiro. Imaging of wave functions and potentials from time-resolved and frequency-resolved fluorescence data. *J. Chem. Phys.*, 103(5):1748–1754, 1995.

[126] M. Shapiro. Accurate determination of excited state potentials from frequency-resolved fluorescence data and knowledge of the ground state potential. *Chem. Phys. Lett.*, 242(6):548 – 554, 1995.

[127] I. Schmidt. Eigenschaften Angeregter Zustände der Alkalidimeren Li$_2$, Na$_2$ und NaLi Sowie deren Kationen aus Ab-Initio-Rechnungen. Master's thesis, Universität Kaiserlautern, Kaiserslautern, 1987.

[128] C. Menzel-Jones, X. Li, and M. Shapiro. Extracting double minima excited state potentials from bound-continuum spectroscopic data. *J. Mol. Spectrosc.*, 268(1-2):221–225, 2011.

[129] F. Lang, K. Winkler, C. Strauss, R. Grimm, and J. Hecker Denschlag. Ultracold triplet molecules in the rovibrational ground state. *Phys. Rev. Lett.*, 101:133005, 2008.

[130] K.-K. Ni, S. Ospelkaus, M. H. G. de Miranda, A. Pe'er, B. Neyenhuis, J. J. Zirbel, S. Kotochigova, P. S. Julienne, D. S. Jin, and J. Ye. A high phase-space-density gas of polar molecules. *Science*, 322(5899):231–235, 2008.

[131] H.-K. Chung, K. Kirby, and J. F. Babb. Theoretical study of the absorption spectra of the sodium dimer. *Phys. Rev. A*, 63:032516, 2001.

[132] S. Magnier, Ph. Millie, O. Dulieu, and F. Masnou-Seeuws. Potential curves for the ground and excited states of the Na_2 molecule up to the (3s+5p) dissociation limit: Results of two different effective potential calculations. *J. Chem. Phys.*, 98(9):7113–7125, 1993.

[133] G. Jeung. Theoretical study on low-lying electronic states of Na_2. *J. Phys. B: At. Mol. Phys.*, 16(23):4289, 1983.

[134] T. Berggren. On the use of resonant states in eigenfunction expansions of scattering and reaction amplitudes. *Nucl. Phys. A*, 109(2):265 – 287, 1968.

[135] T. Berggren. Resonance state expansions in nuclear physics. In *Resonances The Unifying Route Towards the Formulation of Dynamical Processes Foundations and Applications in Nuclear, Atomic and Molecular Physics*, volume 325 of *Lecture Notes in Physics*, pages 105–117. Springer Berlin Heidelberg, 1989.

[136] A. U. Hazi and H. S. Taylor. Stabilization method of calculating resonance energies: Model problem. *Phys. Rev. A*, 1:1109–1120, 1970.

[137] W.G. Valance and J. Lin. Bound state to continuum collisional probabilities. *Physica*, 52(4):620 – 627, 1971.

[138] P. W. Langhoff. Stieltjes-integral approximations to elementary dispersion relations. *Int. J. Quant. Chem.*, 8(S8):347–361, 1974.

[139] J. Römelt and R. Runau. Franck-Condon matrix elements for bound-continuum vibrational transitions calculated by numerical integration and basis set expansion techniques. *Theoretica chimica acta*, 54(2):171–177, 1980.

[140] G. Delacrétaz and L. Wöste. Two-photon ionization spectroscopy of two $(2)^1\Sigma_u^+$ double-minimum state of Na_2. *Chem. Phys. Lett.*, 120(4-5):342 – 348, 1985.

[141] J. Schlejen, C. J. Jalink, J. Korving, J. P. Woerdman, and W. Muller. The absorption spectrum of NaNa from 350 to 1075 nm. *J. Phys. B: At. Mol. Phys.*, 20(12):2691, 1987.

[142] J. Schlejen, J. P. Woerdman, and J. J. de Groot. Identification of NaNa satellites in the 320-350 nm spectral region. *J. Phys. B: At. Mol. Phys.*, 20(12):L369, 1987.

[143] X. Li, C. Menzel-Jones, and M. Shapiro. Spectroscopic phase and the extraction of excited-state potentials from fluorescence data. *J. Phys. Chem. Lett.*, 1(21):3172–3176, 2010.

[144] X. Li, C. Menzel-Jones, D. Avisar, and M. Shapiro. Solving the spectroscopic phase: Imaging excited wave packets and extracting excited state potentials from fluorescence data. *Phys. Chem. Chem. Phys.*, 12:15760–15765, 2010.

[145] K.K. Verma, T.H. Vu, and W.C. Stwalley. New observations and analyses of the laser excited fluorescence of the $A^1\Sigma_u^+$-$X^1\Sigma_g^+$ bands of the Na_2 molecule. *J. Mol. Spectrosc.*, 85(1):131 – 149, 1981.

[146] G. Herzberg, editor. *Molecular spectra and molecular structure*. Van Nostrand Reinhold, Princeton, N.J., 1966.

[147] K. S. Sorbie and J. N. Murrell. Analytical potentials for triatomic molecules from spectroscopic data. *Mol. Phys.*, 29(5):1387–1407, 1975.

[148] S. Altunata and R. W. Field. An assumption-violating application of the Lawrance–Knight deconvolution procedure: A retrieval of electronic coupling mechanisms underlying complex spectra. *J. Chem. Phys.*, 114(15):6557–6561, 2001.

[149] B. M. Wong, R. L. Thom, and R. W. Field. Accurate inertias for large-amplitude motions: Improvements on prevailing approximations. *J. Phys. Chem. A*, 110(23):7406–7413, 2006. PMID: 16759129.

[150] B. M. Wong, A. H. Steeves, and R. W. Field. Electronic signatures of large amplitude motions: Dipole moments of vibrationally excited local-bend and local-stretch states of S0 acetylene. *J. Phys. Chem. B*, 110(38):18912–18920, 2006. PMID: 16986883.

[151] F. Duschinsky. On the interpretation of electronic spectra of polyatomic molecules. *Acta Physicochimica U.R.S.S.*, 7:551–566, 1937.

[152] J. K.G. Watson. Simplification of the molecular vibration-rotation hamiltonian. *Mol. Phys.*, 15(5):479–490, 1968.

[153] D. Avisar and D. J. Tannor. Wavepacket and potential reconstruction by four-wave mixing spectroscopy: Preliminary application to polyatomic molecules. *Faraday Discuss.*, 153:131–148, 2011.

[154] D. Avisar and D. J. Tannor. Multi-dimensional wavepacket and potential reconstruction by resonant coherent anti-stokes raman scattering: Application to H_2O and HOD. *J. Chem. Phys.*, 136(21):214107, 2012.

[155] K. K. Verma, J. T. Bahns, A. R. Rajaei-Rizi, W. C. Stwalley, and W. T. Zemke. First observation of bound–continuum transitions in the laser-induced $A^1\Sigma_u^+$–$X^1\Sigma_g^+$ fluorescence of Na_2. *J. Chem. Phys.*, 78(6):3599–3613, 1983.

[156] P. Jensen and P. R. Bunker, editors. *Computational Molecular Spectroscopy*. Wiley, Chichester, 2000.

[157] D. DeMille. Quantum computation with trapped polar molecules. *Phys. Rev. Lett.*, 88:067901, 2002.

[158] L. E. E. de Araujo and I. A. Walmsley. Analytic solution for quantum control of atomic and molecular wavepackets. *J. Opt. B: Quantum Semiclass. Opt.*, 5(1):R27, 2003.

[159] A. Micheli, GK Brennen, and P. Zoller. A toolbox for lattice-spin models with polar molecules. *Nat. Phys.*, 2(5):341–347, 2006.

[160] A. André, D. DeMille, J. M. Doyle, M. D. Lukin, S. E. Maxwell, P. Rabl, R. J. Schoelkopf, and P. Zoller. A coherent all-electrical interface between polar molecules and mesoscopic superconducting resonators. *Nat. Phys.*, 2:637–642, 2006.

[161] K. Hosaka, H. Shimada, H. Chiba, H. Katsuki, Y. Teranishi, Y. Ohtsuki, and K. Ohmori. Ultrafast fourier transform with a femtosecond-laser-driven molecule. *Phys. Rev. Lett.*, 104:180501, 2010.

[162] T. C. Weinacht, J. Ahn, and P. H. Bucksbaum. Measurement of the amplitude and phase of a sculpted rydberg wave packet. *Phys. Rev. Lett.*, 80:5508–5511, 1998.

[163] H. Katsuki, H. Chiba, B. Girard, C. Meier, and K. Ohmori. Visualizing picometric quantum ripples of ultrafast wave-packet interference. *Science*, 311(5767):1589–1592, 2006.

[164] A. Monmayrant, B. Chatel, and B. Girard. Quantum state measurement using coherent transients. *Phys. Rev. Lett.*, 96:103002, 2006.

[165] K. Ohmori, H. Katsuki, H. Chiba, M. Honda, Y. Hagihara, K. Fujiwara, Y. Sato, and K. Ueda. Real-time observation of phase-controlled molecular wave-packet interference. *Phys. Rev. Lett.*, 96:093002, 2006.

[166] K. Ohmori. Wave-packet and coherent control dynamics. *Annu. Rev. Phys. Chem.*, 60(1):487–511, 2009.

[167] J. P. Palao and R. Kosloff. Quantum computing by an optimal control algorithm for unitary transformations. *Phys. Rev. Lett.*, 89:188301, 2002.

[168] C. M. Tesch and R. de Vivie-Riedle. Quantum computation with vibrationally excited molecules. *Phys. Rev. Lett.*, 89:157901, 2002.

[169] R. de Vivie-Riedle and U. Troppmann. Femtosecond lasers for quantum information technology. *Chem. Rev.*, 107(11):5082–5100, 2007.

[170] C. Menzel-Jones and M. Shapiro. Robust operation of a universal set of logic gates for quantum computation using adiabatic population transfer between molecular levels. *Phys. Rev. A*, 75:052308, 2007.

[171] C. Gollub, M. Kowalewski, and R. de Vivie-Riedle. Monotonic convergent optimal control theory with strict limitations on the spectrum of optimized laser fields. *Phys. Rev. Lett.*, 101:073002, 2008.

[172] L. Bomble, D. Lauvergnat, F. Remacle, and M. Desouter-Lecomte. Vibrational computing: Simulation of a full adder by optimal control. *J. Chem. Phys.*, 128(6):064110, 2008.

[173] R. R. Zaari and A. Brown. Effect of laser pulse shaping parameters on the fidelity of quantum logic gates. *J. Chem. Phys.*, 137(10):104306, 2012.

[174] T. J. Dunn, I. A. Walmsley, and S. Mukamel. Experimental determination of the quantum-mechanical state of a molecular vibrational mode using fluorescence tomography. *Phys. Rev. Lett.*, 74:884–887, 1995.

[175] E. Skovsen, H. Stapelfeldt, S. Juhl, and K. Mølmer. Quantum state tomography of dissociating molecules. *Phys. Rev. Lett.*, 91:090406, 2003.

[176] M. Shapiro. Spectroscopic wave function imaging and potential inversion. *J. Phys. Chem.*, 100(19):7859–7866, 1996.

[177] M. Shapiro. Spectroscopic density-matrix imaging and potential inversion: The rotational effect. *Chem. Phys.*, 207(2-3):317 – 329, 1996.

[178] T. M. Coffey, R. E. Wyatt, and Wm. C. Schieve. Reconstruction of the time-dependent wave function exclusively from position data. *Phys. Rev. Lett.*, 107:230403, 2011.

[179] C. Leichtle, W. P. Schleich, I. Sh. Averbukh, and M. Shapiro. Quantum state holography. *Phys. Rev. Lett.*, 80:1418–1421, 1998.

[180] C. Leichtle, W. P. Schleich, I. Sh. Averbukh, and M. Shapiro. Wave packet interferometry without phase-locking. *J. Chem. Phys.*, 108(15):6057–6067, 1998.

[181] M. Bienert, F. Haug, P. Schleich, W. and G. Raizen, M. State reconstruction of the kicked rotor. *Phys. Rev. Lett.*, 89:050403, 2002.

[182] Patrick F. Tekavec, Thomas R. Dyke, and Andrew H. Marcus. Wave packet interferometry and quantum state reconstruction by acousto-optic phase modulation. *J. Chem. Phys.*, 125(19):194303, 2006.

[183] H. Hasegawa and Y. Ohshima. Quantum state reconstruction of a rotational wave packet created by a nonresonant intense femtosecond laser field. *Phys. Rev. Lett.*, 101:053002, 2008.

[184] J. A. Cina. Wave-packet interferometry and molecular state reconstruction: Spectroscopic adventures on the left-hand side of the Schrödinger equation. *Annu. Rev. Phys. Chem.*, 59(1):319–342, 2008.

[185] T. S. Humble and J. A. Cina. Molecular state reconstruction by nonlinear wave packet interferometry. *Phys. Rev. Lett.*, 93:060402, 2004.

[186] T. S. Humble and J. A. Cina. Nonlinear wave-packet interferometry and molecular state reconstruction in a vibrating and rotating diatomic molecule. *J. Phys. Chem. B*, 110(38):18879–18892, 2006.

[187] T. Kiviniemi, J. Aumanen, P. Myllyperkio, V. A. Apkarian, and M. Pettersson. Time-resolved Coherent Anti-stokes Raman-scattering Measurements of I_2 in Solid Kr: Vibrational Dephasing on the Ground Electronic State at 2.6-32 K. *J. Chem. Phys.*, 123(6):064509, 2005.

[188] M. E. Akopyan, I. Yu. Novikova, S. A. Poretsky, A. M. Pravilov, A. G. Smolin, T. V. Tscherbul, and A. A. Buchachenko. Collision-induced Nonadiabatic Transitions in the Second-tier Ion-pair States of Iodine Molecule: Experimental and Theoretical Study of the $I_2(f0_g^+)$ Collisions with Rare Gas Atoms. *J. Chem. Phys.*, 122(20):204318, 2005.

[189] M. Karavitis, T. Kumada, I. U. Goldschleger, and V. A. Apkarian. Vibrational dissipation and dephasing of $I_2(v = 1\text{-}19)$ in solid Kr. *Phys. Chem. Chem. Phys.*, 7:791–796, 2005.

[190] D. Avisar and D. J. Tannor. Complete reconstruction of the wave function of a reacting molecule by four-wave mixing spectroscopy. *Phys. Rev. Lett.*, 106:170405, 2011.

[191] W. M. Tolles, J. W. Nibler, J. R. McDonald, and A. B. Harvey. A Review of the Theory and Application of Coherent Anti-Stokes Raman Spectroscopy (CARS). *Applied Spectroscopy*, 31(4):253–271, 1977-07-01T00:00:00.

[192] X. G. Xu, S. O. Konorov, S. Zhdanovich, J. W. Hepburn, and V. Milner. Complete characterization of molecular vibration using frequency resolved gating. *J. Chem. Phys.*, 126(9):091102, 2007.

[193] S. O. Konorov, X. G. Xu, J. W. Hepburn, and V. Milner. Characterization of transient molecular vibration excited with shaped femtosecond pulses. *J. Chem. Phys.*, 130(23):234505, 2009.

[194] R. Trebino. *Frequency-Resolved Optical Gating: The Measurement of Ultrashort Laser Pulses.* Kluwer. Academic Publishers, Boston, 2002.

[195] J. Wilkinson. Modern error analysis. *SIAM Review*, 13(4):548–568, 1971.

[196] T. Weber, A. O. Czasch, O. Jagutzki, A. K. Müller, V. Mergel, A. Kheifets, E. Rotenberg, G. Meigs, M. H. Prior, S. Daveau, A. Landers, C. L. Cocke, T. Osipov, R. Díez Mui no, H. Schmidt-Böcking, and R. Dörner. Complete photo-fragmentation of the deuterium molecule. *Nature*, 431:437–440, 2004.

[197] D. Egorov, B. S. Dennis, G. Blumberg, and M. I. Haftel. Two-dimensional control of surface plasmons and directional beaming from arrays of subwavelength apertures. *Phys. Rev. B*, 70:033404, 2004.

[198] Th. Ergler, A. Rudenko, B. Feuerstein, K. Zrost, C. D. Schröter, R. Moshammer, and J. Ullrich. Spatiotemporal imaging of ultrafast molecular motion: Collapse and revival of the $D_2{}^+$ nuclear wave packet. *Phys. Rev. Lett.*, 97:193001, 2006.

[199] I. A. Bocharova, A. S. Alnaser, U. Thumm, T. Niederhausen, D. Ray, C. L. Cocke, and I. V. Litvinyuk. Time-resolved coulomb-explosion imaging of nuclear wave-packet dynamics induced in diatomic molecules by intense few-cycle laser pulses. *Phys. Rev. A*, 83:013417, 2011.

[200] L. Ph. H. Schmidt, T. Jahnke, A. Czasch, M. Schöffler, H. Schmidt-Böcking, and R. Dörner. Spatial imaging of the H_2^+ vibrational wave function at the quantum limit. *Phys. Rev. Lett.*, 108:073202, 2012.

[201] I. Fischer, D. M. Villeneuve, M. J. J. Vrakking, and A. Stolow. Femtosecond wave-packet dynamics studied by time-resolved zero-kinetic energy photoelectron spectroscopy. *J. Chem. Phys.*, 102(13):5566–5569, 1995.

[202] A. González-Castrillo, A. Palacios, H. Bachau, and F. Martín. Clocking ultrafast wave packet dynamics in molecules through uv-induced symmetry breaking. *Phys. Rev. Lett.*, 108:063009, 2012.

[203] T.S. Humble and J. A. Cina. Towards the reconstruction of time-dependent vibronic states from nonlinear wavepacket interferometry signals. *Bulletin Korean Chem. Soc*, 25:584–584, 2004.

[204] M.P.A. Branderhorst, J. Nunn, I.A. Walmsley, and R.L. Kosut. Simplified quantum process tomography. *New J. Phys.*, 11:115010, 2009.

[205] N. Matuschek. G. Steinmeyer L. Gallmann, D.H Sutter and U. Keller. Techniques for the characterization of sub-10-fs optical pulses: A comparison. *Appl. Phys. B*, 70:S67–S75, 2000.

[206] G. Stibenz, C. Ropers, Ch. Lienau, Ch. Warmuth, A.S. Wyatt, I.A. Walmsley, and G. Steinmeyer. Advanced methods for the characterization of few-cycle light pulses: A comparison. *Appl. Phys. B*, 83:511–519, 2006.

[207] S. Birger and S. Heinrich. A method for unique phase retrieval of ultrafast optical fields. *Meas. Sci. Technol.*, 20:015303, 2009.

[208] J. Ratner, G. Steinmeyer, T. C. Wong, R. Bartels, and R. Trebino. Coherent artifact in modern pulse measurements. *Opt. Lett.*, 37(14):2874–2876, 2012.

[209] V. Wong and I. A. Walmsley. Ultrashort-pulse characterization from dynamic spectrograms by iterative phase retrieval. *J. Opt. Soc. Am. B*, 14(4):944–949, 1997.

[210] T.-W. Wu, J. Tang, B. Hajj, and M. Cui. Phase resolved interferometric spectral modulation (PRISM) for ultrafast pulse measurement and compression. *Opt. Express*, 19(14):12961–12968, 2011.

[211] T. C. Wong, J. Ratner, V. Chauhan, J. Cohen, P. M. Vaughan, L. Xu, A. Consoli, and R. Trebino. Simultaneously measuring two ultrashort laser pulses on a single-shot using double-blind frequency-resolved optical gating. *J. Opt. Soc. Am. B*, 29(6):1237–1244, 2012.

[212] C. Iaconis and I.A. Walmsley. Spectral phase interferometry for direct electric-field reconstruction of ultrashort optical pulses. *Opt. Lett.*, 23(10):792–794, 1998.

[213] I. Amat-Roldán, I. G. Cormack, P. Loza-Alvarez, and D. Artigas. Measurement of electric field by interferometric spectral trace observation. *Opt. Lett.*, 30(9):1063–1065, 2005.

[214] T. Witting, F. Frank, C. A. Arrell, W. A. Okell, J. P. Marangos, and J. W. G. Tisch. Characterization of high-intensity sub-4-fs laser pulses using spatially encoded spectral shearing interferometry. *Opt. Lett.*, 36(9):1680–1682, 2011.

[215] A. Pasquazi, M. Peccianti, Y. Park, B. E. Little, S. T. Chu, R. Morandotti, J. Azaña, and D. J. Moss. Sub-picosecond phase-sensitive optical pulse characterization on a chip. *Nat. Phot.*, 5(9):618 – 623, 2011.

[216] A.H. Zewail. Femtochemistry. past, present, and future. *Pure Appl. Chem.*, 72(12):2219–2231, 2000.

[217] C. Menzel-Jones and M. Shapiro. Complex wave function reconstruction and direct electromagnetic field determination from time-resolved intensity data. *J. Phys. Chem. Lett.*, 3(22):3353–3359, 2012.

[218] M. Shapiro and P. Brumer, editors. *Principles of the Quantum Control of Molecular Processes.* Wiley-Interscience, New Jersey, 2003.

[219] W. Salzmann, U. Poschinger, R. Wester, M. Weidemüller, A. Merli, S. M. Weber, F. Sauer, M. Plewicki, F. Weise, A. M. Esparza, L. Wöste, and A. Lindinger. Coherent control with shaped femtosecond laser pulses applied to ultracold molecules. *Phys. Rev. A*, 73:023414, 2006.

[220] L. Chuntonov, A. Fleischer, and Z. Amitay. Weak-field multiphoton femtosecond coherent control in the single-cycle regime. *Opt. Express*, 19(7):6865–6882, 2011.

[221] R. N. Zare. A personal account of developing laser-induced fluorescence. *Annu. Rev. Anal. Chem.*, 5:114, 2012.

[222] M. N. R. Ashfold, S. R. Langford, R. A. Morgan, A. J. Orr-Ewing, C. M. Western, C. R. Scheper, and C. A. de Lange. Resonance enhanced multiphoton ionization (rempi) and rempi-photoelectron spectroscopy of ammonia. *Eur. Phys. J. D*, 4(2):189–197, 1998.

[223] A R Allouche, M Korek, K Fakherddin, A Chaalan, M Dagher, F Taher, and M Aubert-Frécon. Theoretical Electronic Structure of RbCs Revisited. *J. Phys. B: At. Mol. Opt. Phys.*, 33(12):2307–2316, 2000.

[224] I. S. Lim, W. C. Lee, Y. S. Lee, and G.-H. Jeung. Theoretical Investigation of RbCs via Two-component Spin-orbit Pseudopotentials: Spectroscopic Constants and Permanent Dipole Moment Functions. *J. Chem. Phys.*, 124(23):234307, 2006.

[225] Z. Ji, H. Zhang, J. Wu, J. Yuan, Y. Yang, Y. Zhao, J. Ma, L. Wang, L. Xiao, and S. Jia. Photoassociative Formation of Ultracold RbCs Molecules in the (2) $^3\Pi$ State. *Phys. Rev. A*, 85:013401, 2012.

[226] M. Debatin, T. Takekoshi, R. Rameshan, L. Reichsöllner, F. Ferlaino, R. Grimm, R. Vexiau, N. Bouloufa, O. Dulieu, and H.-C. Nägerl. Molecular Spectroscopy for Ground-state Transfer of Ultracold RbCs Molecules. *Phys. Chem. Chem. Phys.*, 13:18926–18935, 2011.

[227] M. Korek, G. Younes, and S. Al-Shawa. Theoretical calculation of the electronic structure of the molecule LiRb including the spin-orbit interaction. *J. Mol. Struct.: Theochem.*, 899(1-3):25–31, 2009.

[228] M. Korek, A.R. Allouche, M. Kobeissi, A. Chaalan, M. Dagher, K. Fakherddin, and M. Aubert-Frécon. Theoretical study of the electronic structure of the LiRb and NaRb molecules. *Chem. Phys.*, 256(1):1–6, 2000.

[229] I. Jendoubi, H. Berriche, H. Ben Ouada, and F. X. Gadea. Structural and Spectroscopic Study of the LiRb Molecule beyond the Born-Oppenheimer Approximation. *J. Phys. Chem. A*, 116(11):2945–2960, 2012.

[230] M. Brouard, editor. *Reaction Dynamics*. Oxford University Press, Oxford, 1998.

[231] R. D. Levine, editor. *Molecular Reaction Dynamics*. Cambridge University Press, Cambridge, 2005.

[232] H. Niikura, H. J. Wörner, D. M. Villeneuve, and P. B. Corkum. Probing the spatial structure of a molecular attosecond electron wave packet using shaped recollision trajectories. *Phys. Rev. Lett.*, 107:093004, 2011.

[233] B. Friedrich and J. M. Doyle. Why are cold molecules so hot? *Chem. Phys. Chem.*, 10(4):604–623, 2009.

[234] C. P. Koch and M. Shapiro. Coherent control of ultracold photoassociation. *Chem. Rev.*, 112(9):4928–4948, 2012.

[235] C. M. Marian. Spin-orbit coupling and intersystem crossing in molecules. *Wiley Interdisciplinary Reviews: Computational Molecular Science*, 2(2):187–203, 2012.

[236] L. Li and A. M. Lyyra. Triplet States of Na_2 and Li_2: Perturbation Facilitated Optical-Optical Double Resonance Spectroscopy. *Spectro. Acta Part A*, 55:2147–2178, 1999.

[237] W.C. Stwalley. Efficient conversion of ultracold Feshbach-resonance-related polar molecules into ultracold ground state $X^1\Sigma^+$ $v = 0, J = 0$ molecules. *Eur. Phys. J. D: At. Mol. Opt. and Plasma Phys.*, 31(2):221–225, 2004.

[238] M.J. Mark, J.G. Danzl, E. Haller, M. Gustavsson, N. Bouloufa, O. Dulieu, H. Salami, T. Bergeman, H. Ritsch, R. Hart, and H.-C. Nägerl. Dark resonances for ground-state transfer of molecular quantum gases. *Appl. Phys. B*, 95(2):219–225, 2009.

[239] A. C. Han, E. A. Shapiro, and M. Shapiro. Pulsed adiabatic photoassociation via scattering resonances. *J. Phys. B: At. Mol. and Opt. Phys.*, 44(15):154018, 2011.

[240] W. Gunton, M. Semczuk, N. S. Dattani, and K. W. Madison. High-resolution photoassociation spectroscopy of the ^{2}Li$_2$ A($1^1\Sigma_u^+$) state. *Phys. Rev. A*, 88:062510, 2013.

[241] B. Bussery and M. Aubert-Frécon. Multipolar long-range electrostatic, dispersion, and induction energy terms for the interactions between two indentical alkali atomics Li, Na, K, Rb, and Cs in various electronic states. *J. Chem. Phys.*, 82:3224–3234, 1985.

[242] R. J. Le Roy, N. S. Dattani, J. A. Coxon, A. J. Ross, P. Crozet, and C. Linton. Accurate analytic potentials for Li$_2$(X$^1\Sigma_g^+$) and Li$_2$(A$^1\Sigma_u^+$) from 2 to 90 Å, and the radiative lifetime of Li(2p). *J. Chem. Phys.*, 131(20):–, 2009.

[243] S. Soorkia, F. Le Quéré, C. Léonard, and D. Figgen. Ab initio study of the spin-orbit coupling between the A and b$^3\Psi_u$ electronic states of Na$_2$. *Mol. Phys.*, 105(9):1095–1104, 2007.

[244] R. Penrose. A generalized inverse for matrices. *Proc. Cambridge Phil. Soc.*, 51:406–413, 1955.

[245] G. Backus and F. Gilbert. The Resolving Power of Gross Earth Data. *Geophysical Journal of the Royal Astronomical Society*, 16(2):169–205, 1968.

[246] W.H. Press, S.A. Teukolsky, W.T. Vetterling, and B.P. Flannery, editors. *Numerical Recipes in C: The Art of Scientific Computing.* Cambridge University Press, New York, 2nd edition, 1992.

[247] C. Menzel-Jones and M. Shapiro. Using Time-Resolved Experiments and Coherent Control to Determine the Phase of Transition Dipole Moments between Individual Energy Eigenstates. *J. Phys. Chem. Lett.*, 4(18):3083–3088, 2013.

[248] C. Menzel-Jones and M. Shapiro. Using coherent control to extract the phases of electronic transition-dipole matrices: the LiRb case. *Can. J. Chem.*, 92(2):94–99, 2014.

[249] A. Drozdova. *Study of spin-orbit coupled electronic states of Rb2, NaCs and NaK molecules. Laser spectroscopy and accurate coupled-channel perturbation analysis.* PhD thesis, Université Lyon, Lyon, France, 2012.

[250] M. Aymar and O. Dulieu. Calculations of transition and permanent dipole moments of heteronuclear alkali dimers NaK, NaRb and NaCs. *Mol. Phys.*, 105(11-12):1733–1742, 2007.

[251] L. B. Ratcliff, D. D. Konowalow, and W. J. Stevens. Electronic transition dipole moment functions for NaK. *J. Mol. Spectrosc.*, 110(2):242 – 255, 1985.

[252] D. J. Heinzen, R. Wynar, P. D. Drummond, and K. V. Kheruntsyan. Superchemistry: Dynamics of Coupled Atomic and Molecular Bose-Einstein Condensates. *Phys. Rev. Lett.*, 84:5029–5033, May 2000.

[253] C. A. Moore, G. P. Davis, and R. A. Gottscho. Sensitive, Nonintrusive, *In-Situ* Measurement of Temporally and Spatially Resolved Plasma Electric Fields. *Phys. Rev. Lett.*, 52:538–541, Feb 1984.

[254] M. Auzinsh, R. Ferber, O. Nikolayeva, N. Shafer-Ray, and M. Tamanis. Influence of the Stark effect on the fluorescence polarization of $X^1\Sigma \to B^1\Pi$-state laser-excited NaRb: Application to the direct imaging of electric fields. *J. Phys. D: Appl. Phys.*, 34(4):624, 2001.